

RF System Modeling and Controller Design for the European XFEL

Vom Promotionsausschuss der
Technischen Universität Hamburg-Harburg

zur Erlangung des akademischen Grades
Doktor-Ingenieur (Dr.-Ing)

genehmigte Dissertation

vorgelegt von
Christian Schmidt

aus
Parchim

Hamburg 2010

Gutachter: Prof. Dr. Herbert Werner
Prof. Dr. Arne Jacob
Dr. Frank Ludwig

Vorsitzender des Prüfungsausschusses: Prof. Dr. Wolfgang Meyer

Tag der mündlichen Prüfung: 26.10.2010

für Juliane

*Das Ganze ist mehr als die Summe seiner Teile.
Aristoteles*

Kurzfassung

Das Deutsche Elektronen Synchrotron wird durch den Bau des Europäischen Röntgenlasers XFEL eine Röntgenquelle besitzen, die intensive, ultrakurze, monochromatische und kohärente Pulse für die Materialforschung bereitstellt. Zur Erzeugung der Röntgenblitze werden Elektronenpakete mittels eines Hochfrequenzfeldes in supraleitenden Hohlraumresonatoren auf Energien bis zu 17.5 GeV beschleunigt. Die digitale Regelung dieser Felder bedarf sehr hoher Qualität, um die physikalischen Prozesse der Photonengeneration zu ermöglichen. Mit FLASH verfügt das DESY über eine Pilotanlage, welche es bereits vor Fertigstellung des XFEL erlaubt, den Großteil der benötigten Komponenten zu entwickeln und zu testen. Die gegenwärtige Feldregelung, basierend auf einer proportionalen Rückführung in Kombination mit einer konstanten Vorsteuerung, kann die hohen Anforderungen für den XFEL nicht erreichen.

Im Rahmen dieser Arbeit wird gezeigt, dass mit einem modellbasierten Reglerentwurf die notwendigen Anforderungen an die Feldregelung erfüllt werden. Hierfür wird zunächst ein lineares zeitinvariantes "Black Box Modell" des Systems erstellt, welches die wesentlichen dynamischen Vorgänge charakterisiert. Dieses Modell basiert nicht auf physikalischen Annahmen, es charakterisiert ausschließlich das Übertragungsverhalten des Systems. Die Beschleunigungsmodule werden in einem gepulsten Modus betrieben, indem für ein finites Zeitintervall das Hochfrequenzfeld konstant gehalten wird. Weiterhin soll die Variation der Felder über viele Pulse möglichst klein sein. Der Charakter der auftretenden Störgrößen und die Eigenschaften des Systems erfordern die Kombination aus geregelter Vorsteuerung und Rückkopplung. In der Regel nicht vorhersehbare, niederfrequente Variationen von Puls zu Puls werden mittels einer Ausgangsrückführung unterdrückt. Die Struktur des implementierten, komplexen Mehrgrößenreglers ist dabei vorgegeben, sodass der modellbasierte Entwurf sich auf die Bestimmung der einzelnen Reglerparameter beschränkt. Die in der modernen Regelungstechnik oft angewandte Methode des H_∞ *loop shaping* ermöglicht es, die Menge an nicht mehr manuell zu bestimmenden Parametern zu ermitteln. Störungen innerhalb eines Pulses hingegen sind aufgrund der kurzen Pulsdauer als hochfrequent anzusehen. Sie können durch die geringe Bandbreite des Systems mit einer Rückkopplung allein nicht ausreichend minimiert werden. Hierbei handelt es sich überwiegend um repetitive Einflüsse, wie den strahlinduzierten Feldabfall. Iterativ lernende Algorithmen erlauben es, die Vorsteuerung dahingehend zu adaptieren, dass auch wiederkehrende Störeinflüsse kompensiert werden. Die Kombination beider Konzepte und die damit erreichten Grenzen der Regelgüte bilden die wesentlichen Ergebnisse dieser Arbeit.

Die gezeigten Ergebnisse stammen aus Messungen an FLASH und demonstrieren damit die Möglichkeit der permanenten Verwendung dieses Reglers während des laufenden Beschleunigerbetriebes als auch des späteren Einsatzes am XFEL. Um die Flexibilität und die Vorteile eines modellbasierten Entwurfs zu zeigen, sind zusätzlich Messergebnisse von weiteren Beschleunigersystemen ausgewertet worden. Überlegungen bezüglich der Integration strahlbasierter Informationen zeigen, dass auf dem Weg zu einer optimalen Feldregelung mit dieser Arbeit die Grundlagen geschaffen sind.

Abstract

The European XFEL is being constructed at the *Deutsche Elektronen Synchrotron* DESY to generate intense, ultrashort pulses of highly coherent and monochromatic X-Rays for material science research. X-ray flashes are generated by accelerating electron bunches within superconducting cavities with radio frequency (RF) fields to energies up to 17.5 GeV. The digital control of these fields requires extremely high quality in order to achieve the physical processes of photon generation. DESY offers with FLASH a pilot test facility, allowing to test and develop most necessary components, even before the XFEL is conducted. Current field control is based on a proportional feedback controller in addition to a constant feedforward drive, which do not meet the high requirements of the XFEL.

This thesis shows that a model based controller design can achieve the necessary field regulation requirements. A linear, time invariant "black box model" is estimated, which characterizes the essential dynamic behavior. This model is not based on physical assumptions, but describes exclusively the transfer behavior of the plant. The acceleration modules are operated in a pulsed mode, in which the RF field must be kept constant for a finite period. The character of the disturbances and variations from pulse-to-pulse, together with the properties of the system, require a combination of controlled feedforward drive and feedback. Generally unpredictable, low frequency pulse-to-pulse variations are suppressed by the feedback controller. The structural design of the complex multivariable feedback controller is given, which constrains the model based design approach to assign the controller parameters only. Estimation of the parameters, which can not be tuned manually, is done by the method of H_∞ loop shaping which is often applied in modern control theory. However, disturbances within a pulse are in a high frequency range concerning the short pulse duration. They are not sufficiently suppressed by the feedback controller alone, due to the small bandwidth of the system. These are mainly repetitive effects like the beam induced field transient decay. Iterative learning control techniques allow adaptation of the feedforward drive such that repetitive disturbances are compensated. The combination of both controllers and the achieved limits of regulation represent the central results of this work.

The results presented are from measurements done at FLASH that demonstrate the possibility of permanent implementation of these controllers for the accelerator operation as well as for later application at XFEL. To show the flexibility and advantages of the model based controller design, additional measurement results are given from other accelerator systems. Considerations for integrating beam based information show that this work forms the basis for optimal field control.

Contents

1	Introduction	1
2	RF control at FLASH	5
2.1	LLRF-System	6
2.1.1	Pulsed operation mode	7
2.1.2	Drive signal chain	9
2.1.3	Cryomodule	10
2.1.4	Field detection and processing	11
2.2	Disturbances	15
2.2.1	Microphonics	16
2.2.2	Lorentz force detuning	17
2.2.3	Beam-loading	18
2.3	Existing models	19
2.3.1	Cavity model	20
2.3.2	Detuning model	21
2.3.3	Summary	22
3	System Modeling	23
3.1	System considerations	24
3.1.1	Model representation	24
3.1.2	Assumptions	25
3.1.3	Plant characteristics	25
3.2	General identification procedure	26
3.2.1	Choice of excitation signals	27
3.2.2	Processing identification data	31
3.2.3	Subspace identification	35
3.3	Measurement results	36
3.3.1	Model validation	37
3.3.2	Open-loop modeling	37
3.3.3	Closed-loop modeling	40
3.3.4	System delay	42
3.3.5	Model extensions by higher frequency dynamics	43
3.4	Model and conclusion	47

4	Feedback Control	51
4.1	Controller implementation	52
4.1.1	Limitations of the closed-loop system	52
4.1.2	Structural design	54
4.2	Controller Design	55
4.2.1	Standard feedback loop	55
4.2.2	Generalized plant and weighting filters	57
4.2.3	Fixed-order controller	58
4.3	Measurement Results	60
4.3.1	Controller application test	60
4.3.2	Performance definition	60
4.3.3	Controller comparison example	62
4.3.4	Measurements from the 3.9 GHz module	65
4.4	Conclusion and suggestions	68
5	Iterative learning control	71
5.1	General properties	72
5.1.1	Repetitive disturbance	72
5.1.2	Overview of iterative learning techniques	73
5.1.3	Norm optimal iterative learning control	74
5.1.4	Limitations for the real plant application	76
5.2	Experimental results	77
5.2.1	Open-loop adaptation	78
5.2.2	Closed-loop adaptation	79
5.3	Combined controllers	84
5.3.1	Measurements with combined ILC and MIMO feedback controller	86
5.3.2	Long-term adaptation after convergence	89
5.3.3	Beam energy spread for a bunch train	92
5.3.4	Implementation considerations	93
5.4	Summary	95
6	Conclusion and Outlook	97
6.1	Achieved goals	97
6.2	Future applications	99
6.3	Beam based feedbacks	102
A	Additional results	111
A.1	Measurements from PSI	111
A.2	RF feedback controller	116
A.3	Additional plots for ILC	117

Chapter 1

Introduction

A current field of research in particle accelerator physics are **Free Electron Lasers (FEL)**, which produce laser radiation with tunable wavelength. In contrast to FELs, conventional laser light sources have a fixed frequency spectrum due to the specific energy levels within the atom structure. The FEL process demands very dense electron bunches, either longitudinal or transversal. The transverse dimensions of the electron bunches have to be in the order of the desired FEL wavelength, while peak current after bunch compression have to exceed 50 A (infrared) or even 5 kA (X-ray), which determines the longitudinal dimension. The typical charge of an electron bunch is in the range of 1 nC.

For many research activities a light source that is able to resolve objects on an atomic level would be favorable, e.g., in molecular biology. Wavelengths of X-ray radiation are in the range of the diameter of an atom (10^{-10} m) such that X-ray radiation is suitable for the desired experiments. However, conventional X-ray sources cannot provide X-ray pulses with a sufficiently short pulse length. This has the effect that e.g., single biomolecules are destroyed by the high energy of the radiation. Moreover, the resolution of conventionally produced X-ray radiation is limited by the broadness of its spectrum. Therefore, laser light is used for a variety of experiments because it can be better focused compared to other light sources, it is monochromatic, and very short pulses can be produced, [1], [2]. At the German Electron Synchrotron (DESY) in Hamburg the X-ray Free Electron Laser research project XFEL is conducted. The goal of the project is to build a Free Electron Laser operating in the X-ray wavelength range by the year 2014, [3]. A prototype test facility for the XFEL has been developed over the last years with the **Free Electron Laser Hamburg FLASH**. This accelerator was basically a project of the TESLA collaboration which developed the superconducting acceleration technology at DESY. Within the years the accelerator was consistently extended by means of additional modules, and finally with the undulator development expanded to a user light source. With a higher number of modules the increased energy of the particles leads to shorter wavelengths down to 6 nm. The generation of light from the accelerated particles is a very complex physical process which is very simplified introduced. The electrons are forced to follow a slalom course in so-called *undulators*, e.g., an arrangement of dipole magnets, leading to the generation of laser light through **Self Amplified Spontaneous Emission (SASE)** with extremely high intensity and quality. Amplification of the radiation is exponential, since concentrated bunches of N electrons do not emit N times the radiation of an electron, but N^2 , [2]. This process is driven by an electron beam demanding an extremely constant energy provided by the particle accelerator. The acceleration

is based on electromagnetic radio frequency (RF) fields, which must be stabilized to a high degree of precision. Achieving high amplitude and phase precision to ensure small variations on the RF field is important in order to accelerate electrons to consistent energy. There is particularly for the so-called injector linac, which is the accelerator subsystem in front of the bunch compressing section. Beam energy variation here leads to arrival-time jitter of the bunch, which has to be avoided. The requirements on the RF field regulation are derived from the necessary compression properties, [2].

- The field amplitude must be within 0.01% (rms) of the reference value.
- The field phase must not differ from the reference value by more than 0.01° (rms).

Future experimental conditions may require even more demanding control objectives. A digital RF field control system is used to provide reference tracking and disturbance rejection. Due to limitations regarding the cryogenic system, responsible for maintain superconductivity, the accelerator is operated in a pulsed mode. The RF fields are brought to the requested level, before the electron bunches arrive and subsequently tuned off again.

Prior to this project, RF fields were controlled by a decentralized proportional controller aided by a pre-determined feedforward drive only. This work describes controller enhancements that complement on-going hardware development. To find a sufficient control concept the knowledge about the underlying plant is essential, gained by system identification. Therefore the basic task of this work is defined as:

- Application of a model-based controller design method, for regulation of RF accelerating fields in superconducting cavities.

To achieve this, the system information must be generated, a model estimated, and the required controllers have to be designed. This work can be considered from two perspectives: the control theory objectives, and real plant implementation. The control theory objectives can be summarized as follows:

1. Develop an appropriate model of the system applying standard subspace identification methods for linear time invariant systems, using input/output data only, i.e. black box model.
2. Estimate the feedback controller parameters which improve the closed-loop field regulation compared to the proportional controller used so far.
3. Apply an iterative learning controller that operates pulse-to-pulse on the feedforward drive.
4. Run both controller types together to combine the advantages of individual controllers to achieve improvements on the field regulation and suppress repetitive disturbances.

Black box models, which are widely used in engineering are used to describe the system dynamics, rather than white box models with physical parameters that are standard in particle physics. A sufficiently accurate estimated open-loop model of the system is necessary to design

a controller that meets the required closed-loop objectives. The disturbance characteristics in this system demand a combined controller concept composing both feedback and feedforward controllers.

As an upgrade of the current feedback controller a multivariable higher-order controller is designed using H_∞ loop shaping methods, [40], [41]. The narrow bandwidth of the system and the limited available power leads to constraints on the maximum disturbance rejection. Fast transients, which are introduced by the particle beam cannot be consequently suppressed by the feedback controller alone.

Fortunately they are predictable and repeatable from one pulse to the next, such that an iterative learning controller can be used to optimize the feedforward signal. This pulse-to-pulse adaptation concept is widely used in repetitive controller task, e.g., robots and automation lines, [49], [63].

As has been introduced previously, the plant is a user facility which has various objectives beside the control theory. The machine operators perspective on the controller implementation can be summarized by the following questions.

1. How can the estimated controllers be implemented on the machine?
2. Do these concepts influence the reliability and operability of this machine?
3. What are the time costs to have this model-based approach? Are the improvements on the field regulation sufficient to justify the higher complexity of this controller?
4. Does an improvement of the field regulation show further improvements on the beam performance?

The controller needs to be "aware" of this objectives especially since the cavities need to be operated close to physical limits in order to fulfill the requirements of the machine. Both, control theory and implementation perspective are considered in the following whereas the machine operation demands higher priority due to the application character of this work.

The contribution of this work is a tested and reliable procedure to a model based controller design, which achieves the previously defined requirements for the RF field control. The model of the plant is estimated using a fixed procedure of data acquisition, processing and model validation. The dynamics of the most important disturbances are classified and distinguished according to the possible suppression strategy. Unpredictable disturbances can be addressed by the output feedback controller, whereas repetitive field excursions are ideally suppressed by feedforward adaptations. A mixed sensitivity design and an iterative learning controller are implemented and tested respectively. Measurements with the electron beam are presented, showing that ideal field regulation does not necessary imply best beam conditions, which is finally the control objective.

In this case often the notation beam and field stability is used, meaning invariance of properties like amplitude or energy, whereas from a control perspective a system is either stable or unstable. Restrictions due to hardware realization boundaries are taken into account. The combined application has been tested and technical expertise is considered for permanent application. To show the applicability of this model based approach, tests on different accelerator systems have been made. The controller design method can be used even with other systems if a model can be

found, and the application provides necessary testing conditions. Finally a concept is presented which will be used for the permanent application on the real plant.

This thesis is organized as follows. In Chapter 2 the RF control system is explained, briefly introducing the corresponding subsystems and focusing on the specifics of the field measurements and according to the digitalization process. The disturbances influencing the field to be controlled are classified to the regulation concepts to be applied. Existing models as well as the black-box system identification approach are discussed in Chapter 3. The steps for estimating a system model specially for this plant from measured data are discussed. In Chapter 4 the estimated models are used to design the feedback controller. Here the concept of the parameter estimation methods is discussed and the best field regulation performance achieved with the H_∞ loop shaping design method is illustrated. In Chapter 5 the principle of iterative learning control for pulse-to-pulse compensation of repetitive disturbances like beam-loading is introduced. Also described is the integration of feedback and feedforward controllers for simultaneously compensating beam-loading effects and suppressing unpredictable disturbances. Finally the implementation for routine user operation is discussed in Chapter 6. Further ideas about the enhancement of the model-based design method are presented, including beam information which are expected to give improvements of the achievable field and beam performance.

Chapter 2

RF control at FLASH

The Free Electron Laser in Hamburg (FLASH) at DESY is an accelerator facility which provides to users a brilliant laser light in the range of the ultra violet spectrum. Furthermore the planned XFEL will be equipped with the technology developed at FLASH. This marks FLASH as a prototype test facility, a main advantage for the research activities. Typical FEL users are interdisciplinary scientist in biology, chemistry and material science. The continuing enhancements of this machine, allow its users to have best experimental conditions. An overview of the facility can be seen in Fig. 2.1.

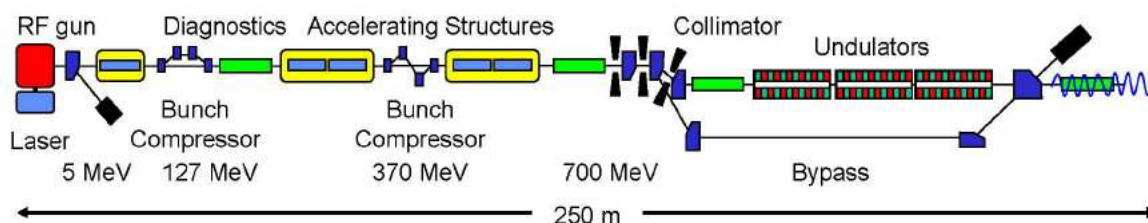


Figure 2.1: Schematic view of the FLASH facility with the main components of the injector, accelerating structures, and the undulator section, [5]

Free electrons are generated in the RF gun. A pulsed laser is focussed on a cathode that emits the particles by means of the photo effect with a defined repetition rate. These bunches are accelerated by a 1.5 - cell normal conducting cavity to an energy of about 5 MeV. The first superconducting acceleration module *ACCI* increases the energy to 127 MeV by electromagnetic field gradients of 12 – 24 MV/m. Next the bunch compressor reduces the longitudinal space of the electron bunch to increase the peak current of the bunch up to 2.5 kA. After this modulation the electrons are further accelerated to approximately 1 GeV. This series of acceleration modules is interspersed by different kinds of magnets for deflection and focussing of the electron beam. Further measurement devices such as cameras are installed for diagnose purpose. Finally the undulators, which are essentially a gallery of cascaded alternating dipoles, force the electron beam to oscillate transversally, causing then to emit photons via synchrotron radiation. This results in a pulsed laser of variable wavelength, the latter depending on the electron beam energy, and may be as low as 7 nm. This laser light is transferred to the user experiments, whereas the residual electron beam is dumped after isolation.

In the following, only the first cryomodule *ACC1* and its associated control system are considered. Nevertheless, the introduced concepts can also be applied to the other modules and even for other control systems, as will be shown later in this thesis. The measurements were made at ACC1 because at the beginning of the work only this module was equipped with the digital control system. Further, the location before the first bunch compressor has advantages in terms of measurement possibilities which are discussed later in this chapter.

The LLRF-System is introduced in Sec. 2.1, including descriptions of the configuration of the energy transport, field detection, and data processing system used for field regulation in FLASH. The main sources of disturbances are discussed in Sec. 2.2, the influence on the field regulation described, and they are classified with respect to the compensation concept. Lastly in this chapter the existing models are discussed in Sec. 2.3 before introducing the novel modeling procedure in the next chapter.

2.1 LLRF-System

The **Low Level Radio Frequency (LLRF)** system is responsible for regulation of the accelerating field in the cavities used for a particle accelerator. This includes the generation of control signals, timing and synchronization, signal acquisition and digital signal processing. The ideal operation scenario is for the machine operator to set the desired acceleration parameters such as energy gain, and the LLRF system then provides the corresponding acceleration field inside the cavities with best achievable accuracy. This demands on the one hand a reliable and suitable control performance and on the other hand a very precise and complex hardware for signal and data transportation and processing. The structure of the currently implemented LLRF control system is shown in Fig. 2.2.

The LLRF system can be divided into analog and digital sections, as indicated in the figure. From the control point of view, the analog part is the plant to be controlled, while the digital part includes the controller and the corresponding data acquisition system. The basis of this work is with the controller.

Specific components of the plant will be introduced later in this section, but first the digital signals presented in the figure are defined:

- **Output signals** y_I, y_Q : Measured sum of the RF field voltage vectors of the eight cavities
- **Reference signals** r_I, r_Q : Reference signals
- **Control error signals** e_I, e_Q : Deviations of the measured output signals from the reference signals
- **Control signals** $u_{c,I}, u_{c,Q}$: Controller output signals
- **Feedforward signals** f_I, f_Q : Open-loop control signals
- **Input signals** u_I, u_Q : Control signals of the digital control system which are applied to the vector modulator

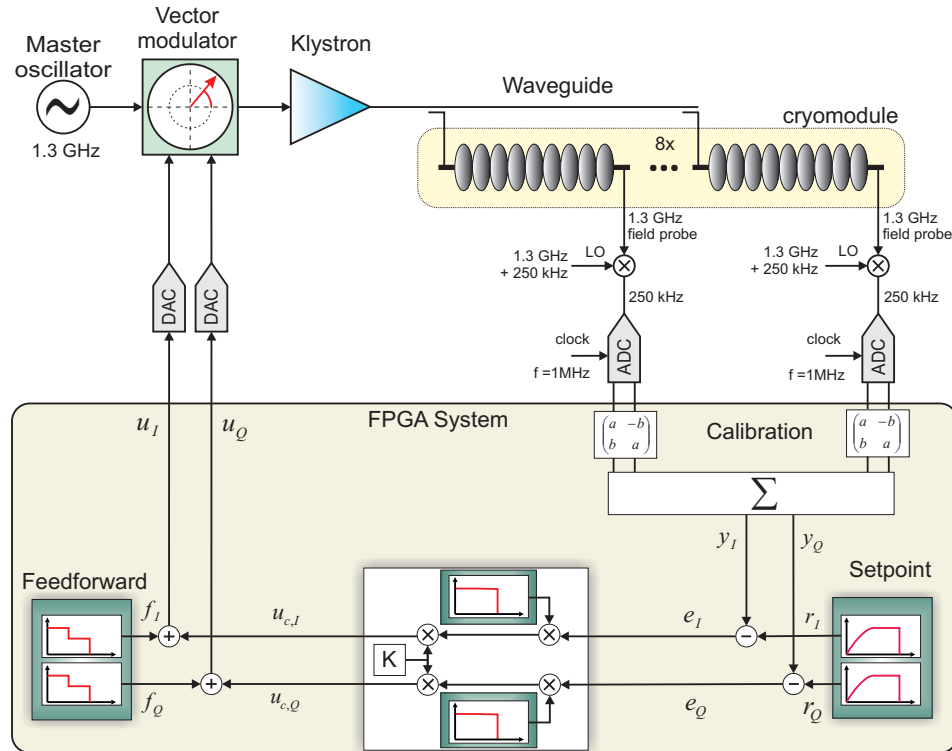


Figure 2.2: Schematic view of the current LLRF control system. The different subsystems are described in the following text, while an overview of the control signals is given in the list below.

The signals are defined in term of the real I (in-phase) and imaginary Q (quadrature) part of the field vector. Rather than of controlling amplitude and phase, the controller processes the decoupled components of I and Q . A typical pattern of the signals in open-loop operation can be found in Fig. 2.3.

This single pulse repeats at a 5Hz rate. The pulse is divided into different phases in time which will be discussed in the following section.

2.1.1 Pulsed operation mode

The accelerating modules (cavities) are made from a niobium alloy, which is a superconductor at liquid helium temperatures. Even at these temperatures, however, power is still dissipated and the thermal losses must be removed by the cooling system in order to keep the cavities superconducting. The dissipated power depends on the acceleration field and the quality factor of the cavity. The cryogenic system is not able to sustain the thermal losses in continuous (CW) operation, which forces the system to be operated in a pulsed mode. The field inside the accelerator cavities has to be kept constant once the required amplitude for the appropriate energy gain of the electrons has been reached at the end of the so-called *filling phase*. During the *flat top phase* the electron beam is injected into the accelerator. When the electron beam has passed, the RF field is turned off and the field amplitude decays until the next pulse starts. This duty cycle reduces the dissipated power to a level that is within the cooling capacity of the

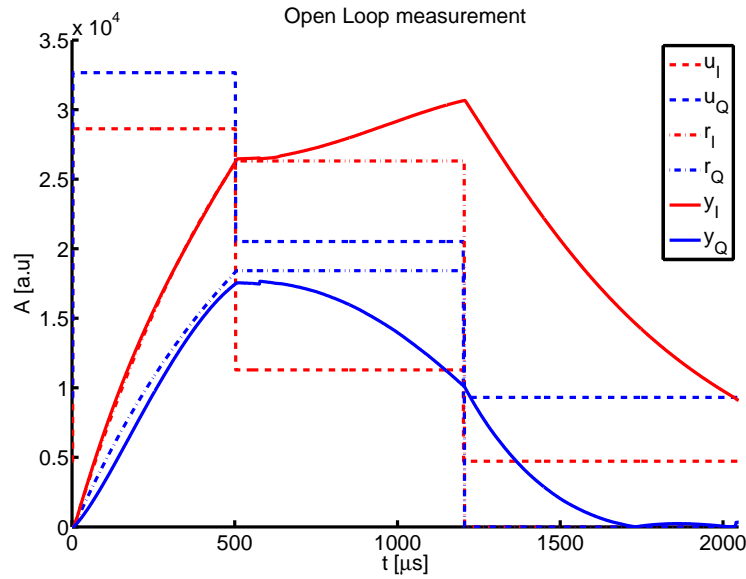


Figure 2.3: Open-loop response to usual feedforward signals, given in the I, Q representation used for data processing inside the controller

cryogenic system. The typical shape of the pulsed mode is shown in Fig. 2.4.

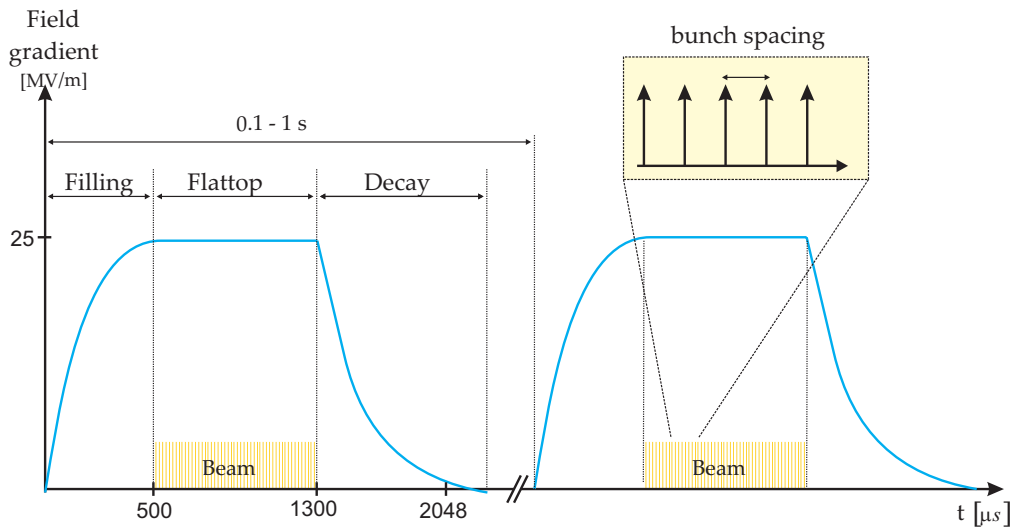


Figure 2.4: RF pulses in superconducting cavities, defining the period of beam acceleration

This figure shows the amplitude of the desired envelope of the RF field for two consecutive RF pulses as a function of time. The resonance frequency of the cavities is $f_0 = 1.3$ GHz, but the envelope of the RF is sufficient for field control since field changes are much slower than the resonance oscillations, [9].

In this work several frequency notations are used for description of ranges of interest. Therefore, in the following table an overview about the different time notations used is given:

<i>notation</i>	<i>frequency range</i>	<i>description</i>
bunch-to-bunch	0.1 – 3 MHz	repetition frequency between two subsequent bunches which depends on experimental settings
intra-pulse	1 MHz	the RF sampling frequency which determines the time between two sampling instants
pulse-to-pulse	1 – 10 Hz	repetition frequency of two subsequent pulses, mainly important for changes in control tables
long-term	< 0.1 Hz	drifts due to environmental changes such as temperature or mechanical oscillations

The time variations are derived from different operation modes to be set by the user. For example, the bunch-to-bunch frequency is often changed based on the needs of each user experiment. For the normal operation, the filling phase is usually set to $t = 500\mu\text{s}$ and the flat top time $t \leq 800\mu\text{s}$ depending on the number of bunches to be accelerated within a pulse. The maximum number of bunches is 2400 assuming a bunch repetition rate of 3 MHz.

Having summarized the digital signals in the LLRF system, the basic analog subsystems of the LLRF station are explained in the following section.

2.1.2 Drive signal chain

The digital signals generated by the control system are converted to analog signals in **Digital Analog Converters (DAC)**. In the chain, the control signals are amplified and transferred to the cavity. Therefore, the real and imaginary field vectors u_I and u_Q have to modulate the cavity resonance frequency of 1.3 GHz, using a vector modulator. The demanded reference frequency is generated in the so-called master oscillator, providing further signals synchronized to this reference. Details are omitted here but can be found in [6]. This processed RF signal must be amplified to drive the system with the demanded power necessary to accelerate the beam. Two preamplifiers and one so-called klystron generates this power amplification, and a waveguide system distributes the RF power to the cavity couplers. The basic functionality of both systems is introduced in the following.

Klystron and waveguide system

A klystron is a large amplifier often used in radio frequency applications where high-frequency power signals are demanded, like radar system or accelerators. The basic principle is to convert a DC electron beam into RF power by bunching processes. This electron beam is generated in a cathode and accelerated by high voltage electrodes. Subsequently the electron beam passes through a cavity which is driven by a high-frequency field. This electromagnetic field introduces an energy profile on the electron beam, such that some electrons are accelerated and others are decelerated depending on the field direction. This leads to different traveling times of the electrons and subsequently a bunching process (density modulation). These bunches induce electromagnetic fields in a second resonator, which can be coupled out.

Currently the considered system to be controlled, consists of 8 cavities which will be increased to 32 cavities controlled by one high power klystron only. Therefore operations close to power

limits cannot be neglected, which is aligned with saturation effects and nonlinear behavior. In measurements presented here, the 8 cavity control does not reach this levels and input/output power linearity can be assumed. The bandwidth of the klystron used is about 6 MHz, which is sufficiently large for this application.

The output power is distributed to the cavities in waveguides, which is a power transmission line to carry almost lossless electromagnetic waves especially in the microwave and optical frequency range. Finally the RF power is coupled to the cavities by coaxial couplers, which are a very sensitive part in this chain. It is possible to influence the wave propagation by a tuning mechanism that the amplitude and phase of the incoming wave. This is necessary to adjust the matching between the waveguide and the cavities inside the cryomodule.

2.1.3 Cryomodule

The cavities are housed in cryomodules, along with and various measurement and supply equipment such as field probes, piezo sensors and motor tuners. The main purpose of this module is to carry several temperature layers including cryogenic supply pipes isolating the superconducting cavity from the environment. The type of cryomodule type used for FLASH is about 12 meters long and hosts 8 cavities enclosed by liquid helium.

Cavity

The cavities are superconducting electromagnetic resonators composed of *Niobium* material, which has the physical properties to conduct almost lossless high currents at temperatures of about 2 K. These currents are generated by the high electromagnetic fields inside the cavities used for particle acceleration. Due to superconductivity the cavity has a high quality factor Q defined as:

$$Q = 2\pi f_0 \frac{W}{P_{diss}} \quad , \quad (2.1)$$

where W is the stored energy and P_{diss} the dissipated power. The quality factor is very high in a superconducting resonator, e.g. approximately $Q = 10^{10}$ for Tesla type cavities. The vacuum inside the cavities minimizes collisions between the accelerated particles and residual atoms. One resonators consist of nine cells of special geometry as shown in Fig. 2.5, [7].

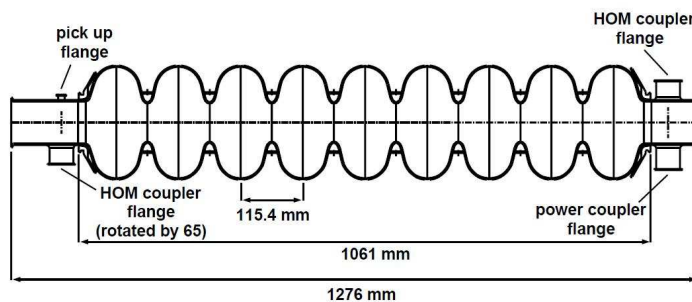


Figure 2.5: View of a 9 cell tesla type cavity with couplers [7]

Each cavity hosts 9 fundamental modes having electrical field vectors in direction of the cavity axis. The so-called π -mode is excited by the resonance frequency of $f_0 = 1.3$ GHz, whereas all other modes are unwanted. Energy from the klystron is propagating from the power coupler through the weakly coupled cells, creating a standing electromagnetic wave in this structure. Slight changes of the geometry have significant effects on the resonance frequency. This is exploited in the frequency tuning process where stepper motors are used to distort the cavity. The π -mode is of special interest, with respect to the electrical field component on axis. The field amplitude of this mode is equal in all cells, but has the opposite sign from one subsequent cell to the next, [8]. On the cavity axis it is observed as a sine wave with a period of 2 cells with the maximum amplitude in the center of each cell in the longitudinal direction. For beam acceleration, this provides a field gradient in direction of transition when the particles enter the first cell. As the beam travels to the next cell, the electric field direction reverses, and the particles are accelerated in that cell. This pattern is further repeated over the full cavity length. Wave propagation and the relativistic electron velocity $v \approx c$ are balanced which is important for a constant acceleration.

Beam operation

The electrons being accelerated are relativistic, so the increase in their velocity is negligible, already being close to the speed of light. The energy consumption however is significant. This energy gain is provided in the real part of the complex field vector, given as:

$$V_{acc}(t) = V_{cav} \cdot \cos\varphi_b = V_{cav} \cdot \cos(\omega t_b) \quad , \quad (2.2)$$

with the beam phase φ_b with respect to the phase of the cavity field vector V_{cav} , [9]. On crest operation is determined when the beam passes the cell during the time the electric field has its maximum amplitude, whereas off-crest operation is done to introduce an energy profile along the bunch which is necessary for the bunch compression procedure. In this case the beam phase deviates from the field phase by about 5 – 10 degrees. Thinking about a sine wave, the beam traverses the cell not when the field is at its maximum, but on the rising edge. The bunches pass through the bunch compressor, which is a chicane in the beam pipe comprising a series of dipole magnets, that reduces the longitudinal dimension of the electron bunch. An energy profile over the bunch leads to variable deflections in the dipole magnets and corresponding traveling paths. All particles in the bunch have the same velocity, which finally results by the different traveling time to compression. This system is very susceptible to energy variations which translate to an unwanted arrival-time jitter. Requirements for the field regulation performance are derived from the arrival-time stability requirements given by the machine users. How to accurately provide the demanded RF field is discussed in the following.

2.1.4 Field detection and processing

For appropriate field regulation it is first necessary to measure the actual field in the cavity, which is done directly by field probes at the edge of the last cell as it can be seen in Fig. 2.5 (pick up). For data processing, the analog signals have to be transmitted over long distances from the accelerator tunnel to the computation devices. This makes the RF signals susceptible to environmental influences, e.g. temperature changes or crosstalk. Furthermore, latencies are

introduced by the traveling time, and this might limit gains in the digital control loop. Once the data are transmitted to the regulation system they are processed.

IQ-sampling scheme

For data processing, the analog signals have to be digitized, which is usually done by sampling the signals with a sufficiently high sampling frequency. The Analog to Digital Converters (ADC) available on the market at the time of system implementation were not sufficiently fast to directly sampling the RF field. Today the development in this technology allows to overcome this drawback. Nevertheless the sampling method introduced next is still applied, using a modulation concept to convert the high-frequency signals down to an intermediate frequency (IF), in a so-called downconverter. This IF is sampled with a special method named IQ-sampling, [10] where original radio frequency of 1.3 GHz is mixed with an additional frequency contribution shifted by about 250 kHz as it is shown in Fig. 2.6.

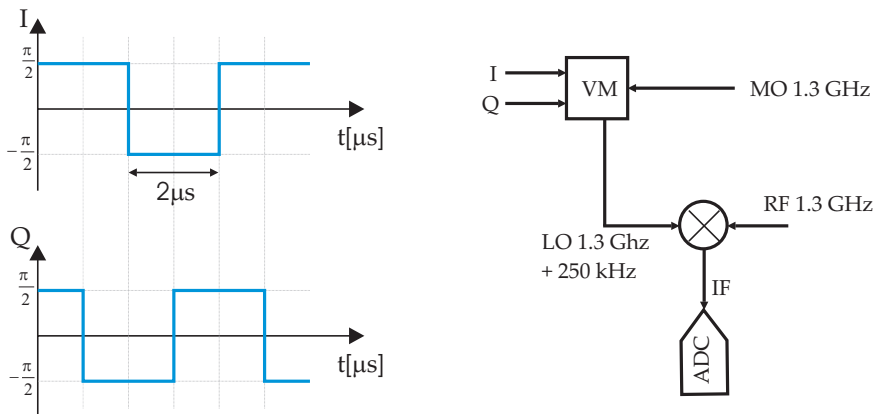


Figure 2.6: Downconversion of the RF signals with time step changes of IQ, sampling and frequency distribution

This local oscillator frequency is generated by the vector modulator. The modulation in this case is done by step changes for the I and Q channel as shown in Fig. 2.6, [11]. After multiplying the IF with the measured RF, the resulting high-frequency term is filtered out so only the low-frequency part remains. The phase and amplitude information is now transferred to the intermediate frequency which can be sampled by the ADC as it is shown in Fig. 2.7.

The field information is computed by sampling the steps of the downconverter output as sketched in Fig. 2.7. After the step transition, which can be adjusted by a variable delay, the values are sampled at 81 MHz and averaged, as shown in the figure. The field vector components are determined in series of $I, Q, -I, -Q$, and further rotated for every sampling instant of about 90° . With the sampling time of 1 MHz, within one period exactly 4 values are calculated. Effectively every $2\mu\text{s}$ a new pair of I,Q values is generated, whereas the sampling frequency of $1\mu\text{s}$ implies getting a new data pair every sampling instant. This can be provided by computing the new vector from one step back value, and rotating it of about 90° . This procedure is possible because of the very narrow bandwidth of the cavity, where the field changes are expected to vanish between two sampling steps. This sampling method is very sensitive to the generation

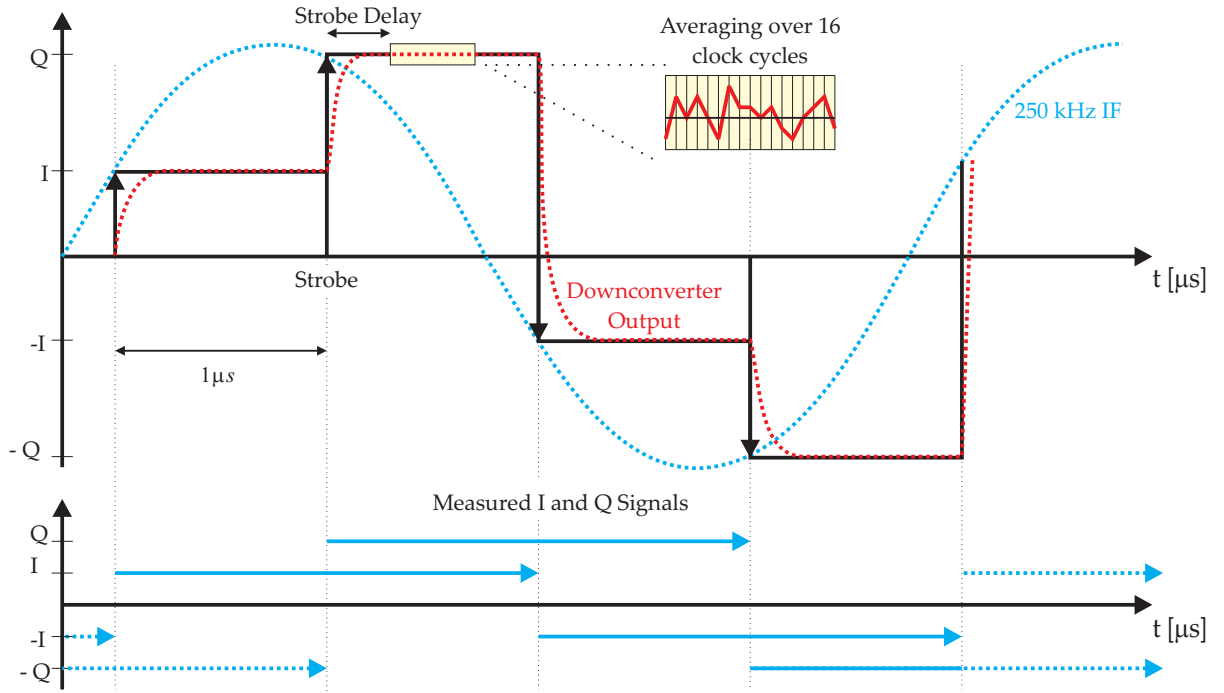


Figure 2.7: Schematic illustration of the IQ sampling and data averaging method, having the downconverted IF frequency.

of the intermediate frequency steps, e.g the step heights vary which leads to non-perfect circles in the IQ planes and therefore wrong calculation of the field vector. The digital IQ data generation and all digital processing operations are done within an **F**ield **P**rogrammable **G**ate **A**rray (FPGA) placed on the so-called Simcon (**S**imulator and **C**ontroller) board. As the name suggests, this board can be used either as the controller platform or as a simulator for testing controller applications. A side view picture of this board can be seen in Fig. 2.8.

The FPGA has the advantage that the controller structure as well as new applications are easily realized by reprogramming this device accordingly. The internal clock rate of the FPGA is 81 MHz, which is sufficient to allow averaging of 16 values each sample in the IQ detection scheme shown in Fig. 2.7. The latency introduced by this detection algorithm is about $2\mu\text{s}$. Further processing steps in the pipeline take about 500 ns. Therefore the overall input-output delay sums up to 3 sampling steps measuring the input output response with the sampling instants. For detailed information it is referred to [12]. As already introduced in Sec. 2.1.2 it is not one cavity field vector but the sum of several cavities data is used for regulation. This processing step is discussed next.

Vector sum calculation and calibration

The klystron is one of the most expensive devices in the accelerator system. Costs need to be minimized to keep new linear accelerators like the XFEL affordable. Supplying every single cavity with one klystron is much more expensive, then having one large RF source for several cavities. For the XFEL it is planned to have 32 cavities, installed in 4 cryomodules driven

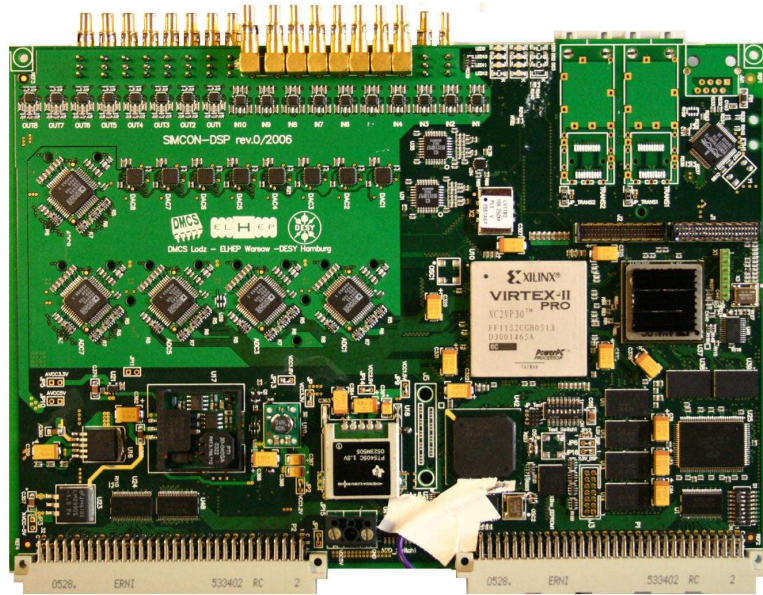


Figure 2.8: Picture of the Simcon DSP board used currently for LLRF control including ADCs, DACs, DSP, Virtex FPGA and optical links

by one 10 MW klystron. The disadvantage is that because single cavities are not individually controllable, the system is under-determined. It is assumed that all cavities have the same physical behavior, so it is possible to sum up all individually field contributions which are also seen by the electron beam. The vector sum represents the amount of energy the particle gains as it would be accelerated in one module with the same amount of energy. Certainly summing up the individually field vectors averages over noise contribution from the field sensors, ideally leading to more accurate field measurements if the noise contributions are uncorrelated. The improvement in accuracy is \sqrt{N} , with N the number of cavities. The vector sum calculation is done in the FPGA on one controller board for 8 cavities, partial sums are build when controlling more cavities and further combined. Therefore the real and imaginary field vector components are summed up. Before the summation a calibration of the individual components has to be done, e.g. compensating for different cable length. Without this calibration the measured field vector differs from the real field vector resulting in a regulation error. For this calibration there exists a rotation matrix that scales the amplitude and rotates the phase of the individually measured field vector. Calibration errors cause the measured vector sum differ from the actual vector sum seen by the beam, which significantly impacts quality of field regulation. In Fig. 2.9 a pattern of the actual and measured vector sum is sketched.

Currently the calibration is done by measuring the field decay introduced by the electron beam passing the cavities. The charged particles are a stable current which generates with the shunt impedance of the cavity a voltage with opposite direction to the stored field voltage. Assuming all cavities have equal impedances this voltage must be equal in all cavities. The regulation has to be turned off and the cavities are only operated by the open-loop control signals. Calibration coefficients are derived by differences in the individual field decay measurements. Therefore the individual field vectors are rotated and scaled to a defined reference cavity. Details about

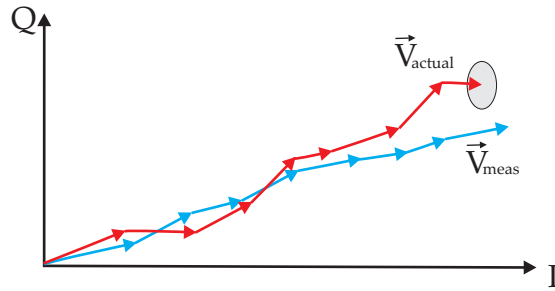


Figure 2.9: Sketch of the basic idea of vector sum calibration with measurement and estimation errors

this procedure can be found in [13]. Finally the generation of the control signals is introduced briefly.

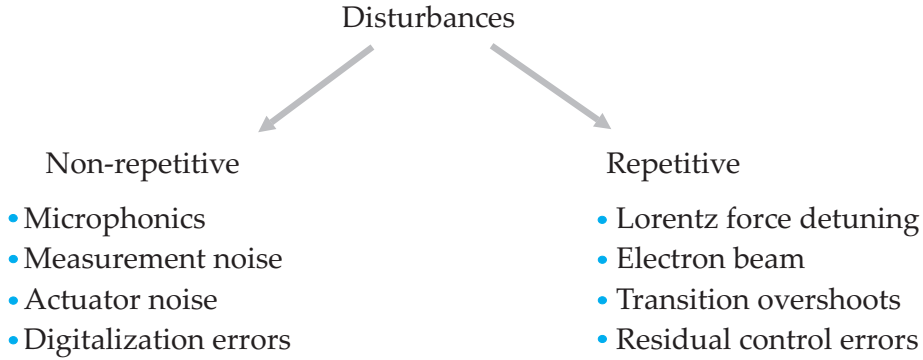
Controller tables

The controller output is generated in the FPGA from tables that define the values for everyone of the 2048 sample points in one pulse. As illustrated in Fig. 2.2 the vector sum is computed and then subtracted from the setpoint table. The resulting field deviation is further multiplied with gain tables, that define the gain factor for each sampling step. Currently this table is kept constant during the filling and flat top phase, although scheduling the gain factor to improve the field regulation is intended.

The controller used for normal operation is a decentralized proportional feedback, that controls the two vector components individually. Later in this work this controller is replaced by a multivariable controller. Finally the open-loop control signals are added to the controller output, generating a driving signal which leads the plant to reach almost the reference trajectory or setpoint. The feedback controller is used to compensate small field deviations around this operation point. The disturbances leading to this imperfections in the system response are discussed next.

2.2 Disturbances

As is typical for a real system in presence of a disturbed environment, influences to the controlled system cannot be neglected. This disturbances can come from various sources and can be categorized according to the strategy of suppression. The following diagram shows the classification in two subgroups, namely repetitive and non-repetitive disturbances. This breakdown was chosen according to the possible regulation concepts, namely feedforward and feedback control. The repetitive components in this case are predictable and can be compensated by the feedforward signal to the system, updated between two pulses. Non-repetitive disturbances on the other hand cannot be foreseen. The influences must be compensated by the feedback controller which acts within a pulse. These non repetitive disturbances are mainly caused by noise sources from the measurement equipment, digitalization process and also actuator imperfections. In the following, three main disturbance contributions are distinguished, all of which will recur within this work when discussing the controller performances.



2.2.1 Microphonics

Microphonics are mechanical vibrations of the system hardware that couple to the cavity, leading to small oscillations which change the cavity geometry. Accelerator components such as cooling systems and vacuum pumps, or man-made sources such as road traffic or environmental ground motion are sources of mechanical vibrations. The high quality factor of the cavity makes it very sensitive to vibrations, which shift its eigenfrequency by $\approx 300 \text{ Hz}/\mu\text{m}$. An example plot of the shifted resonance peak can be seen in Fig. 2.10.

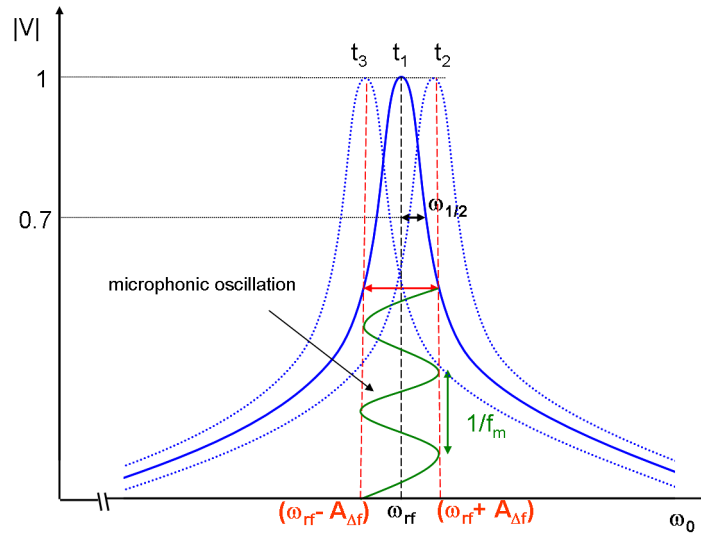


Figure 2.10: Resonance curve displacement of the cavity due to microphonic vibrations. The maximum achievable output voltage is given as function of the excitation frequency.

The microphonic oscillation in this figure is simplified constituted as a sinusoidal oscillation of:

$$\Delta\omega(t) = A_{\Delta f} \sin(2\pi f_m t + \phi) \quad , \quad (2.3)$$

with the microphonic amplitude $A_{\Delta f}$ and frequency of f_m . These vibration frequencies are typically in a range up to a few hundred hertz, which in pulsed operation appears as fluctuations from pulse-to-pulse. The amplitude or resonance frequency change for this type of cavities is typically $\sigma_{A_{\Delta f}} \approx 6 \text{ Hz}$, [14]. The small changes in the resonance frequency have a strong impact on the field, because the RF drive frequency remains unchanged. Imperfect matching between

the antenna and the module leads to a lower field amplitude which must be compensated by the feedback controller. Beside the increased power, these fluctuations are undesirable because they cause residual field errors visible as pulse-to-pulse fluctuations on the vector sum if not perfectly compensated. To keep these effects small the cavities are mechanically stiffened in order to passively suppress the effects. Further there are proposals to actively compensate the microphonic oscillations, by a mechanical feedback loop, [15] and [16].

2.2.2 Lorentz force detuning

In contrast to microphonic vibrations, the so-called Lorentz force detuning (LFD) is treated as a repetitive disturbance, even though the detuning effect is also caused by deformations of the cavity. In this case, however, the electromagnetic field inside the cavity acts on the thin cavity walls and the resulting electromagnetic forces are sufficient to change the cavity geometry. This process is sketched in Fig. 2.11, [17].

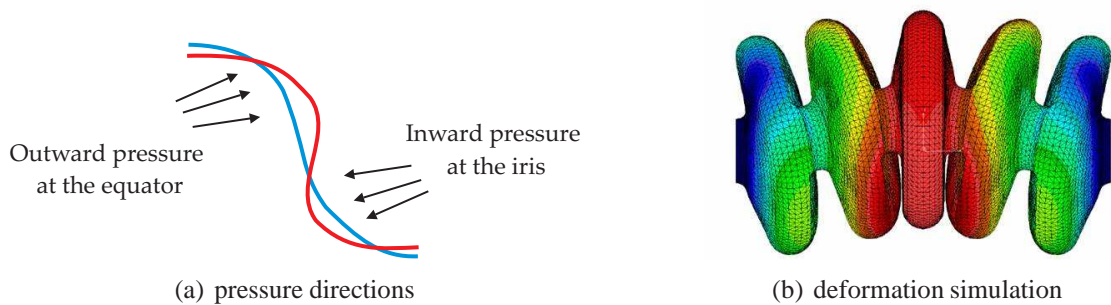


Figure 2.11: Influences of geometric deformations to the cavity. The resonance frequency is sensitive to deformations in the accelerating modules.

Compared to the microphonic deformations, this effect leads to stronger resonance frequency deviation. Instead of vibration around the resonance frequency, the detuning represents a constant drift of the cavity eigenfrequency. If the RF field does not change from pulse-to-pulse, the deformations will show almost the same behavior. Influences such as the LFD are well understood and further predictable. Studies on this topic can be found in [18] and [19]. If the system would not be operated in pulsed mode, the detuning would reach a final steady state when the introduced deformations and the rigidity of the cavity are in balance. In this case one could simply detune the cavity by the RF field induced frequency shift. For the pulsed operation mode only the transient response is measurable, since steady state is not reached before the RF is turned off at the end of the flat top. Deformations disappear before the next pulse starts, so the effect is repeated with the next pulse. A measurement using deformation sensors (piezos) is shown in Fig. 2.12, giving the transient detuning response.

Unfortunately this measurement could not be correlated with the field measurement data. Only a relative behavior is detectable, showing that the deformation increases with field gradient in the cavity as postulated. A simulation example on this topic is given in Sec. 2.3.2. From Fig. 2.12, one can observe that the pulse is started at the sampling instant of about 2000 and

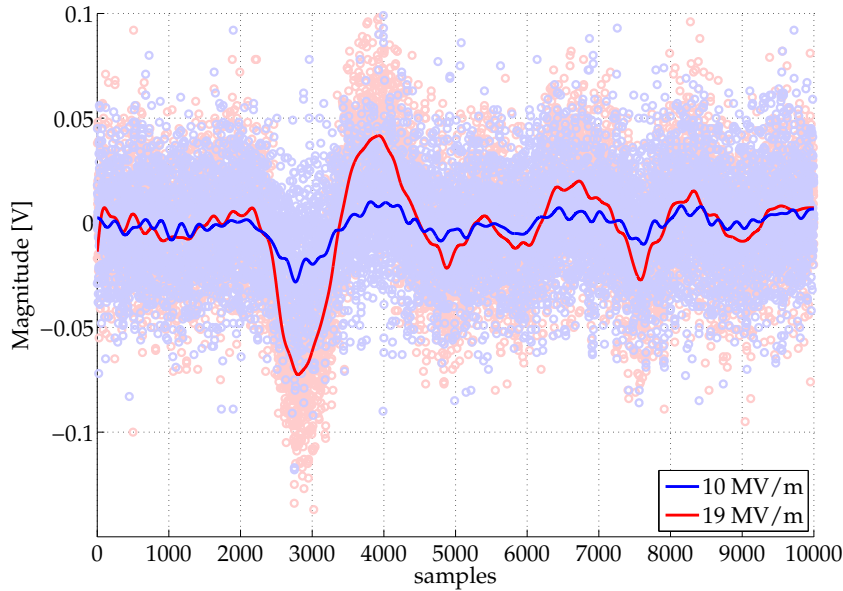


Figure 2.12: Measurements of detuning by piezo detectors for two different gradients as function of time. Due to synchronization issues these data cannot be correlated with measured field information.

the pulse stopped at the maximum amplitude at about 2800. One can see that the oscillations continue, which can be ascribed to mechanical modes of the cavity.

Effects of this detuning process can be seen from Fig. 2.3, where the open-loop system response is measured. The significant deviation of the field from the setpoint is caused by the LFD, visualized in the IQ plot. In Fig. 2.13 the impact in the amplitude and phase representation is also shown. This means that the field inside the cavity can only be kept constant if the input power is increased. Otherwise the field amplitude decreases and the phase drifts away from the setpoint. For practical application the cavities are pre-detuned such that the detuning effect is minimized during the flat top region so as to keep the deviation minimal during beam acceleration, although this also increases the required power in the filling phase. Passive compensation is done by stiffening rings that enhance the rigidity. The cavity walls have to be kept thin due to thermal reasons and material costs. Active LFD compensation is currently under developments and first test show the benefit in much reduced detuning.

2.2.3 Beam-loading

The most serious disturbance to the RF field comes from the electron beam itself. Due to the interaction with the RF field, the energy for the beam acceleration is transferred from the field to the beam, which must be ascribed by the RF field regulation. In this case the beam-loading can be seen as a disturbance, whereas the beam is the actual value to be controlled and further used as independent measurement for the quality of regulation. Characteristic of this disturbance source is determined by the charge, repetition rate, quantity and phase of the particle beam. Usually these parameters remain unchanged during operation which means this

can be classified as a repetitive disturbance source. Small variations, e.g. in the charge from the electron gun are negligible. The effect of this beam-loading can be seen from Fig. 2.13, where the feedback loop is already closed.

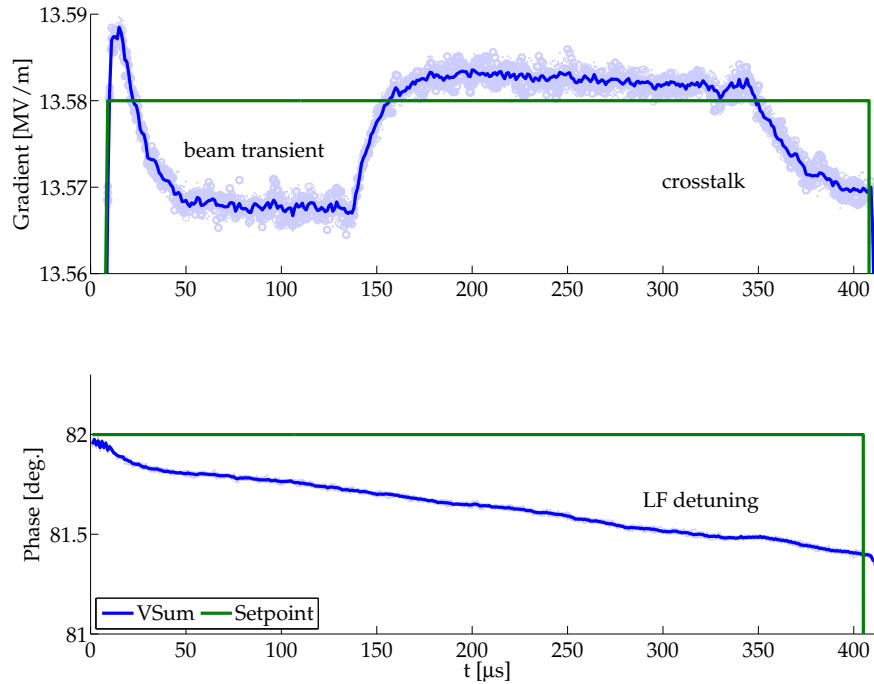


Figure 2.13: Effects of beam-loading with a particle beam of 30 bunches and a charge of 3 nC. The proportional feedback controller closes the loop!

It can be easily observed that the feedback controller is not able to sufficiently compensate the beam-loading effect. In addition this disturbance causes a steady state error until the beam is turned off. If the beam properties are not changed this large field drop is predictable as is illustrated in Fig. 2.13, where the measurement points for several pulses are overlaid as blue dots.

As a result it can be claimed that the design of a feedback controller alone will not be able to suppress all disturbances, rather the addition of pre compensation by an appropriate feedforward signal could significantly reduce the remaining control error. To design this combined controller, first a system model is needed. Before introducing the procedure of system identification, the existing models are outlined in the following.

2.3 Existing models

Existing models are derived from physical considerations of the different subcomponents in the plant. Therefore several assumptions have been made, which are briefly discussed when introducing the models. In the next chapter a system modeling procedure will be discussed

where characteristics of the physical models are auxiliary, e.g. for prior assumptions or model verification. The dominant contribution to the system dynamics is certainly the cavity, due to the small bandwidth compared to other subsystems in the plant. Therefore the physical model is based on this subsystem.

2.3.1 Cavity model

The derivation of the cavity model has been given in several works like [9], [11], [13], and therefore need not be repeated here. Rather the focus is more on the characteristics of this model. As already introduced in Sec. 2.1.3, the cavity is an electromagnetic resonator, which allows the propagation of standing electromagnetic waves for a resonance frequency of 1.3 GHz, determined by its geometry. The electromagnetic field is weakly coupled from cell to cell. As an equivalent representation, a coupled LCR circuit as sketched in Fig. 2.14 is used.

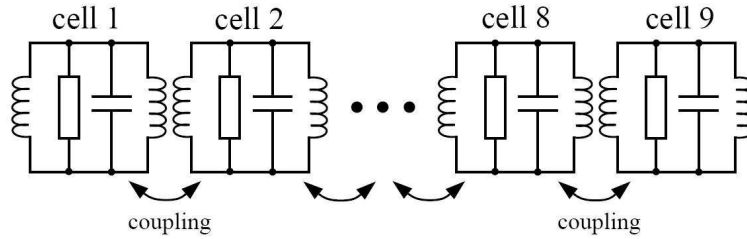


Figure 2.14: Equivalent circuit diagram for the 9 cell cavity, showing the coupling between the cells.[9]

Solving the differential equation, which can be derived from this circuit representation leads finally to the state space representation of the field envelope, after removing the high-frequency oscillations. The remain transient behavior is desired as given in Eqn. 2.4, [9].

$$\begin{pmatrix} \dot{V}_I \\ \dot{V}_Q \end{pmatrix} = \begin{pmatrix} -\omega_{1/2} & -\Delta\omega(t) \\ \Delta\omega(t) & -\omega_{1/2} \end{pmatrix} \begin{pmatrix} V_I \\ V_Q \end{pmatrix} + \begin{pmatrix} R_L\omega_{1/2} & 0 \\ 0 & R_L\omega_{1/2} \end{pmatrix} \begin{pmatrix} I_I \\ I_Q \end{pmatrix}, \quad (2.4)$$

with the shunt impedance of the cavity defined as:

$$R_L = \left(\frac{r}{Q}\right) Q_L. \quad (2.5)$$

The cavity voltage is given as \vec{V} in terms of the real and imaginary field component and the driving current as \vec{I} . For the TESLA type cavities considered in this work the physical parameters in the state space representation are:

Symbol	Value	Unit	Description
Q_l	$3 \cdot 10^6$	/	loaded quality factor
ω_0	$2\pi \cdot 3 \cdot 10^9$	1/s	resonance frequency
$\Delta\omega(t)$	$\omega_0 - \omega(t)$	1/s	detuning frequency
$\omega_{1/2}$	$\approx 2\pi \cdot 216.7$	1/s	half bandwidth
$\frac{r}{Q}$	1024	$\frac{\Omega}{m}$	normalized shunt impedance

It is easy to observe that within this representation there is a fixed structure in the system matrices. The terms on the diagonal elements are equal for the real and imaginary field component. This is obvious from physical considerations and the detection algorithm, where the field components are only representation of a 90° rotated field vector. Unless the field detection algorithm introduces some errors the components must not differ in its behavior. Later it will be shown that this diagonal structure has significant influence on the modeling procedure. Additionally it can be observed that the detuning effects described in Sec. 2.2 assign the coupling between the two field vector components. Time dependency is caused by the microphonic oscillations as well as transients introduced by the LFD. There exist a model describing the effect of the lorentz force detuning, which is discussed next.

2.3.2 Detuning model

A mechanical model is used to describe the time varying detuning $\Delta\omega(t)$ as function of the accelerating electric field E_{acc} , as previously introduced in [17]. This second-order model relies on mechanical modes in the cavity which can be described as:

$$\Delta\ddot{\omega}(t) + \frac{1}{\tau_m}\Delta\dot{\omega}(t) + \omega_m^2\Delta\omega(t) = \omega_m^2\Delta\omega_T - 2\pi K\omega_m^2 \cdot E_{acc}^2(t) \quad , \quad (2.6)$$

with τ_m the time constant of the damping and ω_m the resonance frequency of the mechanical oscillation. Additional pre-detuning of the resonance frequency is represented by $\Delta\omega_T$. In Fig. 2.15 the detuning curves are simulated with a typical parameter set for field gradients.

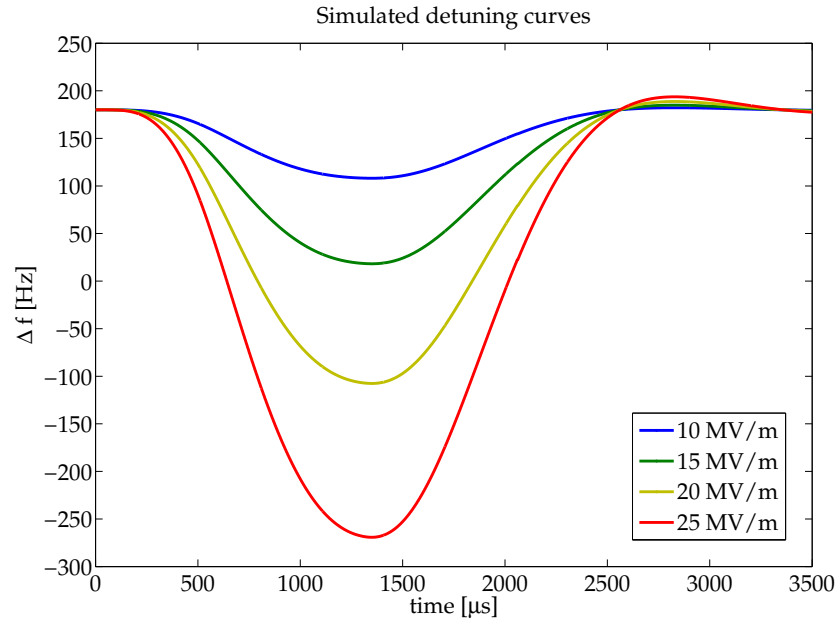


Figure 2.15: Simulated detuning curves for different field gradients as function of time

The mechanical model and physical state space representation of Eqn. 2.4 have been investigated and studied in numerical simulations with *Matlab Simulink*. Furthermore as mentioned

in the description of the Simcon board, it can be used as controller and simulator, where the simulator is based on the combined model introduced here. This model, however, is both non-linear and time varying, which would place high demands on the modeling process discussed in the next chapter. To overcome this drawback, a first approach in this thesis is to use a linear time invariant model approximation to determine the sufficiency for the controller design. The integration of the mechanical model into the cavity model, was further investigated in [26].

2.3.3 Summary

In this chapter the LLRF system was introduced along with the main subcomponents that are necessary for the operation of a single LLRF station in an accelerator complex. Further, pulsed operation mode was explained with the consequences for field regulation tasks. As a main topic, the sources of possible disturbances have been classified according to the suppression strategy to be discussed later. Three main contributions to field imperfections were emphasized in terms of their physical origin. Finally, existing system models were outlined, with respect to assumptions to be made in the system identification procedure. It is claimed that the cavity dominates the system behavior, which allows effects from other subcomponents to be neglected in the modeling procedure. Nevertheless the plant is modeled as the whole chain between controller output u_I, u_Q and the computed vector sum controller input y_I, y_Q .

For all measurements presented in the following chapter the control system introduced here has been used. Additionally a duplicate of this system has been installed in parallel by splitting the field probes. Field detection and vector sum calculations use this parallel system. The main advantage was the possibility of running setup procedures prior the real measurements, significantly improving efficiency of the the actual experimental time. Further it allows observation of the regulation system with an parallel measurement equipment out of the feedback loop.

Chapter 3

System Modeling

This chapter will focus on the mathematical representation of the RF system and components that were described in the previous chapter. For most control design methods it is essential to have a model of the system representing the static and dynamic behavior, which can be generalized according to the usage and application.

There are three possible methods to determine such a model. First the so-called *White Box model*, where it is assumed that the physical behavior is exactly known. The model is found by describing the system by a set of differential equations containing physical laws such as conservation of energy or electric losses. The physical system model given in Sec. 2.3 was determined by this method. In general the behavior of real plants are not fully understood, hence a second category of models is needed, where it is assumed that the physical context is known but the parameters or states of this system have to be determined. Estimating these variables by experiments and fitting them to the given set of differential equations is the basis of *Grey Box models*. For the cavity system of Sec. 2.3 this would mean that the parameters like $\omega_{1/2}$ are estimated, e.g. by measuring the loaded quality factor Q_L . Some considerations of methods for determining such physical parameters can be found in [26]. The assumption here is that the system dynamics is dominated by the small bandwidth of the cavity.

Black box models are often used to describe systems which behaviors are not well understood, and as the name presumes, there only is a linearity assumption about the internal system dynamics of the plant. The only possibility of characterizing the system is by its input-output behavior in mathematical notation. The states do not necessarily have a physical interpretation but they have a conceptual relevance. The plant output can be predicted by simulation with the black box model and defined input signals. Here this method was chosen to find an appropriate system identification method which not only relies on the cavity dynamics, but also on the surrounding environment which might influence the system. Therefore various experiments have been performed to model the system which will be described in detail in the following.

The chapter is organized as follows: first, in Sec. 3.1, the system structure is described ; then in Sec. 3.2, the identification steps and method of modeling are described in detail; Sec. 3.3 covers results from measurement on the real plant, leading to the models and conclusions in Sec. 3.4 that are used in later chapters for controller design.

3.1 System considerations

Like every other system, this plant has individual characteristics to be considered before processing parameter identification. It is known that the dynamics are dominated by the cavity compared to the other subsystems in the black box, e.g. klystron, couplers and measurement devices. The subsystems are shown in Fig. 2.2, where the input to the plant is defined as the controller output to the DAC, and the system output will be the computed vectorsum. The vector components are given in terms of I (in-phase) and Q (quadrature) of the field vector. It is possible to measure not just the sum but every single cavity vector, however it is not possible to control every single cavity, so the system is underdetermined. Hence, the input-output behavior must be defined.

3.1.1 Model representation

Having two inputs and outputs to the system, it is defined as a multivariable input, multivariable output (MIMO) system, which is represented in state space notation as:

$$\dot{x}(t) = A_c x(t) + B_c u(t) \quad , \quad (3.1)$$

$$y(t) = Cx(t) + Du(t) \quad , \quad (3.2)$$

with the state vector $x \in \mathbb{R}^n$, the control input $u \in \mathbb{R}^m$, the output vector $y \in \mathbb{R}^l$ and the constant system matrix $A_c \in \mathbb{R}^{n \times n}$, input matrix $B_c \in \mathbb{R}^{n \times m}$, output matrix $C \in \mathbb{R}^{l \times n}$ and the feedthrough matrix $D \in \mathbb{R}^{l \times m}$. For physically realizable systems the matrix D is usually a zero matrix. The data generation and storage is done at discrete sampling instances, so the model will be a discrete time model.

Discrete time model

In most modern control applications digital controllers are implemented and it is convenient to use discrete time models. The continuous time state space representation Sec. 3.1.1 can be transformed to a discrete time representation by computing the discrete time system matrix A_c and input matrix B_c as:

$$A = e^{A_c T} \quad , \quad B = \int_0^T e^{A_c t} B_c dt, \quad (3.3)$$

where T denotes the sampling time. This leads to the state space model:

$$x(k+1) = Ax(k) + Bu(k) \quad , \quad (3.4)$$

$$y(k) = Cx(k) + Du(k) \quad , \quad k = 0, 1, \dots, N \quad (3.5)$$

where k denotes the discrete sampling instants and N is the maximum number of instants. FLASH is operated in pulsed mode, with each pulse containing 2048 sample points (limited by buffer size inside the electronics). The continuous time and discrete time models can be converted easily using MATLABs commands `c2d` and `d2c` respectively. For controller design

both types of models are used and therefore mentioned here. For linear time-invariant models, parameters A, B, C, D are constant matrices of appropriate dimensions. Some assumptions have to be made in order to use this specific type of model.

3.1.2 Assumptions

In general for real plants, the dynamics is rather complex and influenced by the individual characteristic of the system. Although it is not necessary (and often not wanted) to model all details, an approximation can be sufficient to characterize the model. Using some basic assumptions, the system can be described in a very simple way such that well-understood system identification procedures can be applied. Here linear time invariant (LTI) models should be used for the system description, provided the system fulfills the two properties of *linearity* and *time-invariance* with good approximation. For most physical systems these conditions are fulfilled.

System linearity and time invariance

From physical considerations about the real plant, it is known that especially the klystron in the actuator part is the main source of nonlinearities, so when operating close to saturation limits as it is planned, the identification and modeling procedures must be adapted. Furthermore the measurement part of the control system also shows nonlinearities, e.g. if the ADC is operated in compression. Under typical system operation using a moderate feedback gain, the system is driven around the operation point, so it can be assumed that the linearity assumption is true. The time variance must be distinguished for both, pulse-to-pulse and intra-pulse variations. From the physical model, it is known that the detuning effect is a time variant parameter changing during the pulse. Also it is known that from pulse-to-pulse, microphonic effects have an impact, allowing the system to vary frequently. Furthermore unpredictable long-term drifts might be observed that are a consequence of temperature changes. All these effects are assumed to be negligible in this model representation. It has to be shown that these assumptions can be made for unchanged system conditions such as pulse length or field gradient. Beside the definition of an LTI system, further typical system properties are pointed out in the following.

3.1.3 Plant characteristics

In addition to define the prerequisite assumptions, it is also necessary to mention some specifics of the underlying system. The identification can be improved if prior knowledge of the physical description is taken into account. Furthermore, model validation can be performed by verifying whether typical behavior can be recovered using the estimated model.

While introducing the system, it was claimed that this consists of a 2×2 MIMO system, where the inputs and outputs are the real and imaginary part of the complex field vector. From a physical point of view it is the difference between the vector of the incoming electromagnetic wave and the measured vector inside the cavity. This means that in this special MIMO system, the diagonal elements must model the same physical behavior. This assumption presumes that the measured system data are representing a plant without measurement errors from the data acquisition. This is in general not the case for a real plant, although the noise contributions should be small compared to the system response.

Furthermore detuning effects can be found in the cross coupling elements of the MIMO system. As a consequence of the detuning effect, a constant input power results in an increasing amplitude of the output channel I, whereas the amplitude of Q decreases, as shown in Fig. 2.3. This cross coupling effect will be modeled as a constant detuning factor. Further, it will be shown that a detuning slope must be removed from the data. During normal system operation, the cavity is initially slightly detuned in order to compensate the detuning effect within a pulse to get a constant flat top.

Compared to the diagonal elements in this model, the cross coupling components have less impact on the system response because the detuning effects are less significant than the system bandwidth. A plausibility check can be made by checking if the system is diagonal dominant. This assumes the system is appropriately calibrated, which can easily be checked when rotating the measured field vector by 90 degrees in the calibration matrices, in which case the IQ detection would interpret the channels as swapped. Both amplitude and phase must be calibrated before closing the feedback loop.

A typical system response can be seen in Fig. 2.3, where the usual feedforward signal is applied. It is easy to visualize that the system is mainly dominated by the small bandwidth of the cavity. The system has a time constant of about $700\mu s$ which is in range of a typical flat top duration. The open-loop system response does not reach steady state conditions within a pulse! Consequently, the open-loop control signal uses a higher input power during the cavity fill time and then set lower at the beginning of the flat-top to the level that gives a steady state field. The challenge in this case is to find a controller which increases the bandwidth of this system in order that the system is able to react on disturbance influences. The black box modeling procedure will now be discussed in detail.

3.2 General identification procedure

Estimating the model parameters is done by using the following general sequence of steps that take into account the properties and physical limitations of the system.

1. **Find an appropriate excitation signal:** This signal or sequence of several signals must be able to excite all system dynamics that need to be modeled.
2. **Postprocess the measured data sets:** Trends and means from the observed data must be removed in order to model the actual excited system around the operating point. Averaging is a possible method to suppress measurement noise from the signal, while filtering, shifting data sequences or removing outliers might be necessary to have a suitable data set for the identification process.
3. **Assign model structure and identification method:** The complexity and kind of model must be defined before identification. In this case a black box model in state space representation has been chosen, the variable to be determined is left to the order of the model.
4. **Choose identification algorithm and estimate model:** This was described previously. The data sets are prepared to estimate the chosen model.

5. **Validate the model:** The validation process should verify whether an adequate model could be found, and the reliability of the model is examined by comparing with measured system data not used in the identification, or by comparing with physical known parameters of the system. Comparisons can also be made with other established models of the system.

It is planned that a semi-automated routine for system identification will be implemented on the real plant. A fixed procedure has to be developed in order to estimate the model frequently, for example in cases when the operation point has changed. This is also necessary because of the limited time available for studies and application development. During this work, experience led to slight modifications to the identification procedure that solved modeling issues and allowed to further improve the model estimation. As an example, determination of an adequate excitation signal has been found over several iterations that converged on the following set of data input signals.

3.2.1 Choice of excitation signals

One of the most critical steps in system identification is to find an appropriate excitation signal that excites all relevant modes of the model. The "richness" of a signal can be described in term of *persistently exciting*, [20]. The signals used for excitation are discussed later in this section. Considering characteristics one can find terms of conditions like, the amplitude must be sufficiently large that the system response can be detected in presence of measurement noise but small enough that linearity assumptions hold around the operation point. For excitation in the high-frequency range this aspect is more crucial, due to the known narrow bandwidth of the system. High-frequency dynamics in this case might be hard to detect due to the noise contributions in the field detection process. These considerations can be summarized as follows:

- Appropriate amplitudes for a good signal to noise ratio and nonlinearities prevention
- Persistent excitation of the system to detect all dynamics modes of the system

Taking all these considerations into account, the characteristics of the signal can be derived. Beside the type of signal used for identification there are also limitations on the data acquisition and pulse duration. It has been outlined that one pulses consists of $N = 2048$ samples, whereas the time duration of excitation is limited to the flat top area. The maximum flat top time is given as about $800\mu s$, which is short time period given the system time-constant. Additionally transient effects have to be removed in the beginning of the flat top introduced by the feedforward step at the filling to flat top transition, hence the first samples in the flat top are not used for excitation. The maximum number of possible identification samples per pulse has been chosen for the experiments to $N = 750$ (compare Fig. 3.3). Given a sampling time of $T = 1\mu s$, the lower bound of the maximum possible input frequency is defined. The excitation will be added to the given feedforward tables during the flat top time, allowing to study the system response at the operation point. Nevertheless after applying the excitation signal, several pulses can be recorded until the excitation is turned off again. Due to the short pulse duration, long-term measurements cannot be done since the system does not reach a steady state within a pulse, which has drawbacks for the identification of very low-frequency characteristics. When presenting the

identified models in Sec. 4.3, effects regarding these limitations will be discussed. The kinds of excitation signals used for the identification are introduced in the following section, while the final choice will be discussed when measurement results are presented in Sec. 4.3.

Random excitation signals

Perfect white noise signals are generally not realizable for identification experiments. Limited system requirements and length of data sets restrict the bandwidth of possible input signals. Excitation sequences with comparable properties must be found. This forces the usage of so-called **p**seudo **r**andom **b**inary sequences (PRBS) for identification. This signal can be obtained from linear shift registers producing an uncorrelated sequence that repeats after a certain amount of steps. Another possibility is using chirped sinusoidal input signals for excitation.

$$u(t) = \sum_{k=1}^d a_k \cos(\omega_k t + \phi_k) \tag{3.6}$$

Here it is feasible to have a wide band of excitation amplitudes compared to the identification using PRBS signals, where the input amplitude is varied by switching between u_{min} and u_{max} . The bandwidth used here is determined by a priori knowledge of the system dynamics. Nevertheless the excitation bandwidth should not be too low to detect some unknown dynamics especially in the higher frequency range. The generated signal is mean free and must fulfill conditions which can be found in [20]. Both signal types can be found by free available algorithms or using the *System Identification Toolbox of Matlab*, [22].

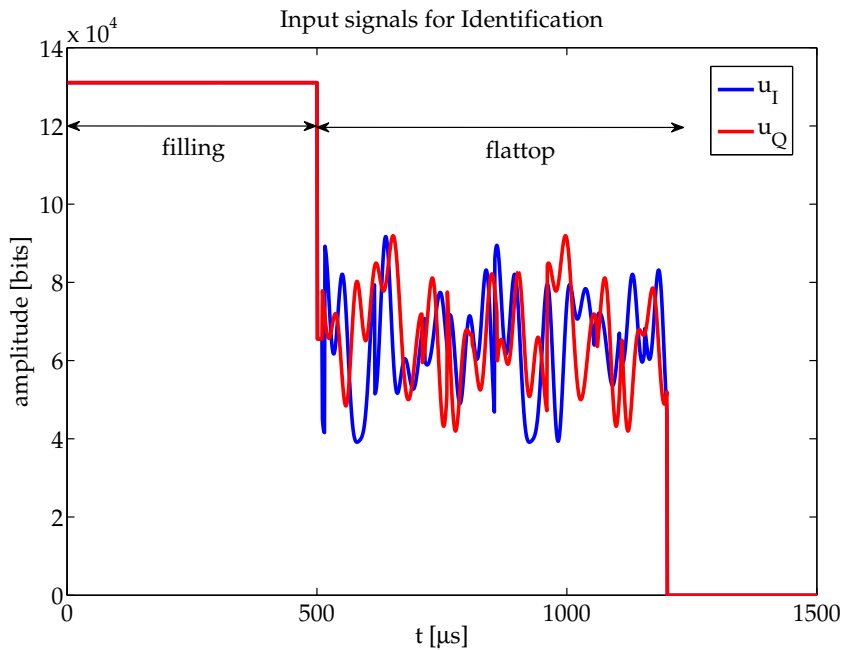


Figure 3.1: Excitation with sinusoidal random signals during flat top for the I and Q channel simultaneously. The signal amplitude is kept to about 1/3 of the operating point to have a good signal to noise ratio without exciting the system too far from the usual operating point

During the measurements it turned out that exciting both channels (I and Q) at the same time as shown in Fig. 3.1 might lead to modeling difficulties (see. Sec 3.3.2). Applying the excitation signals on both channels in consecutive pulses leads to improvements in this case, as it is described in the following.

Combining channels

By this method two experiments are used to excite both input channels of the system separately. It is known that the system dynamics of both channels are theoretically equal. Therefore it would be possible to excite in a first step the I-channel and measure the response in both output channels. In the second step this experiment is repeated with excitation on the Q-channel. For each of these two identification sequences, it is possible to identify two SIMO (single input, multiple output) models. This overcomes the drawback that cross-coupling components are over-estimated, if both channels are excited simultaneously by uncorrelated input signals. The two identified SIMO models can be merged to a single model by combination of the estimated system matrices A, B, C as follows:

$$A = \begin{bmatrix} A_1 & 0 \\ 0 & A_2 \end{bmatrix}, \quad B = \begin{bmatrix} B_1 & 0 \\ 0 & B_2 \end{bmatrix}, \quad C = [C_1 \quad C_2], \quad (3.7)$$

where the subscripts 1 and 2 assign the individual model parameters. The combined system matrices A, B, C contain of the individual system matrices and zero matrices of appropriate dimensions. Individual estimated SIMO models must have the same system order. It turned out that this method leads to modeling improvements as shown in Sec. 3.3.2. Previously, the diagonal dominance, known from physical consideration, was not reflected in the estimated models if the excitations has been applied on both channels simultaneously. Distribution of this separate excitation on both channel within a pulse is not feasible due to the limited pulse duration and variable detuning characteristics within a pulse. Taking into account the assumptions made in Sec. 3.1.2, equal experimental conditions are given for both excitation channels. Additionally this method implies a possible validation procedure. Knowing that both channels are supposed to have nearly the same behavior, it can easily be detected either if the modeling process or the system data itself might be corrupted. An example of PRBS excitation can be seen in Fig. 3.2. By conducting several excitation experiments over consecutive pulses, it is possible to extend the identification process and merge the input/output data, as it is described in the following.

Sequence merging

Having a limited pulse length makes it feasible to apply methods of merging different sets of input/output data into a joint set. For the pulsed operation, it is fast and easy to conduct several experiments, even with different kinds of excitation. In this case the plant is excited in different frequency ranges as it can be seen in Fig. 3.3. After carrying all experiments, the data sets are appended in series by Matlabs identification toolbox [22].

In addition, it is possible to combine different kind of excitation signals, such as PRBS and chirped sine-waves, allowing to test different frequency ranges with wider or smaller bands, for example to detect sharp resonance peaks like the $\frac{8}{9}\pi$ -mode that are known from theory.

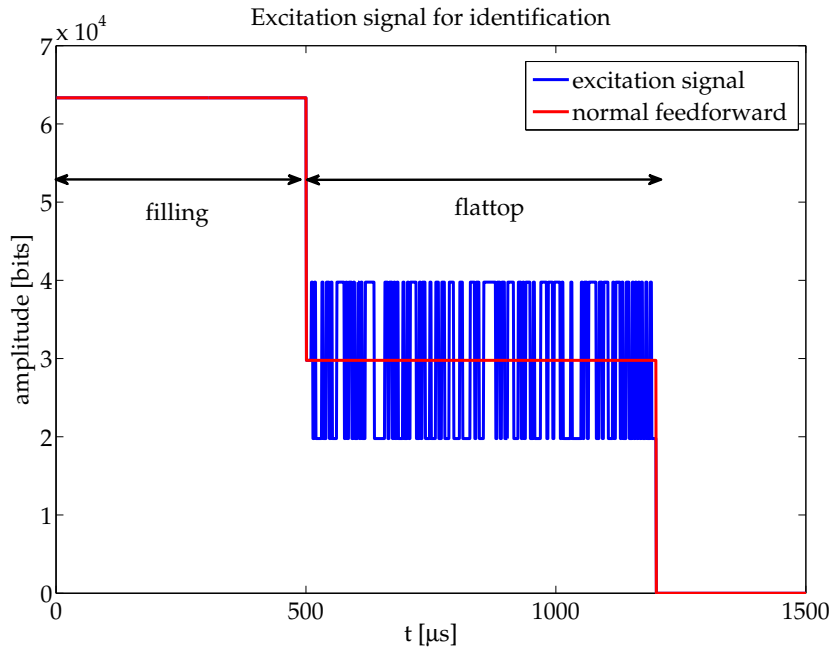


Figure 3.2: Example of the excitation signal used for Identification. Only one input channel is excited with an PRBS signal. The same input is used for the second input channel in order to have same identification conditions in both channels

Measurements show that only exciting the system for one pulse over a broad band does not lead to find this peak, even when increasing the model order. Usage of several small band excitations around the assumed resonance frequency and combining these measurements with other low-frequency excitations might lead to an appropriate model that spans all significant modes of the system. A priori knowledge of the plant about possible resonance peaks is necessary to excite around this assumed peak in an appropriate way, so the system was excited with sinusoidal oscillations of constant frequency.

Sinusoidal excitation of constant frequency

Excitation with sinusoidal oscillations of constant frequency does not fulfill the criterium of persistent excitation, but doing so might be beneficial for detection of resonance peaks. So far, it has not been possible to use random signals to detect dynamics of the additional modes described in [8]. It is assumed this is because the noise contribution of the field detection system is crossfading these signals. An example of constant sinusoidal input signals is shown in Fig. 3.4.

By sweeping the frequency of the sinusoidal signal and measuring the response it should be possible to detect resonance peaks in the measured output. These tests have been made in open-loop and closed-loop operation with the proportional feedback controller for various gains. If the feedback loop is closed, cross coupling cannot be prevented due to the coupling between I and Q signals. This method has only be applied to find resonance peaks which might be present in the plant. It was not intended to use this method for identification only, but to gain informa-

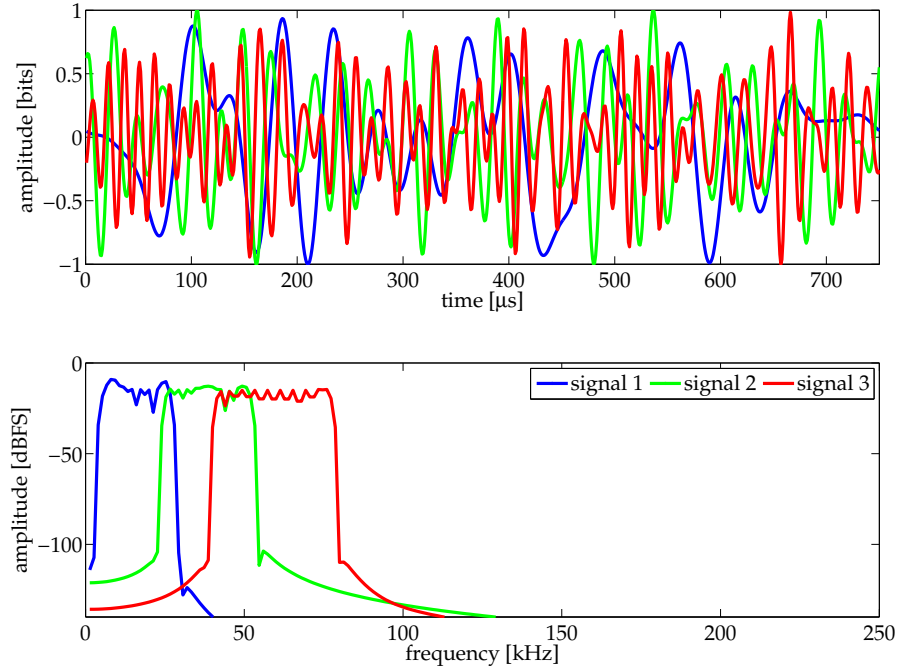


Figure 3.3: Example data set of different excitation signals used for merging different experiments. In the upper plot the time domain data, and in the lower plot the corresponding frequency spectrum is displayed.

tion about the system and improving the ordinary identification signals introduced before. The results of this method are discussed in Sec. 3.3.5.

3.2.2 Processing identification data

As step two of the identification process, the data must be pre-processed in order to provide sufficient data sets to generate the model. Possible and necessary pre-processing tasks can be found in [20]. Usually data that have been recorded during the excitation is not used for the identification process directly, for example because corrupted data sets or outliers must be removed. For each excitation signal, typically 20 system responses were recorded. Advantages about this will be discussed in this chapter. For the following considerations all methods are described for a single dataset. The system responses can be found as the mapping of input to output channels as discrete time transfer function matrix

$$\begin{bmatrix} y_I(z) \\ y_Q(z) \end{bmatrix} = \begin{bmatrix} G_{11}(z) & G_{12}(z) \\ G_{21}(z) & G_{22}(z) \end{bmatrix} \begin{bmatrix} u_I(z) \\ u_Q(z) \end{bmatrix} \quad (3.8)$$

Although the pre-processing steps presented in the following have been applied to all mapping directions, the examples are discussed for the channel G_{11} only, without loss of generality.

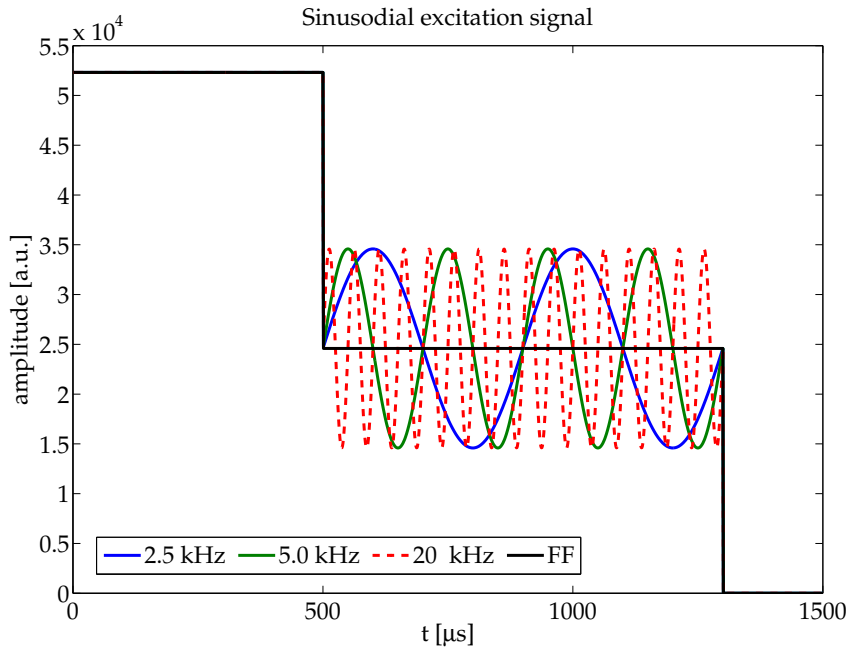


Figure 3.4: Example for the used sinusoidal excitation signals. The various frequency are snapshots of consecutive experiments.

Trends and means

Offsets and drifts in measurement data are quit common and must be removed before identification. Another possibility, but not applied in the following, is to have a disturbance model, which is estimated and representing such influences, [20]. Usually drifts are generated by the system itself or caused by the surrounding environment.

In the following, three ways of processing the measurement data are shown and the advantages regarding the modeling is discussed. From Fig. 2.3 it is easy to observe that the open-loop system response for a constant feedforward during the flat top is strongly influenced by the detuning characteristic introduced in Sec. 2.2.2. To remove this constant offset introduced by the operation point, is to subtract the mean value by:

$$\tilde{y}(t) = y(t) - \bar{y}(t) \quad , \quad (3.9)$$

where \tilde{y} is the detrended system output of $y(t)$ with the mean value of $\bar{y}(t)$. Generally for the operation point measured here, $\bar{y} \neq 0$ holds. Detuning effects can be seen as an bias or slope during the flat top, which is to be removed by a linear trend instead of subtracting the mean value only. Even more generally, a fitting polynomial can be found as:

$$p(t) = \sum_{i=0}^n a_i t^i = a_0 + a_1 t + \dots a_n t^n \quad , \quad (3.10)$$

of order n and a_i ($i = 0, \dots, n$) weighting coefficients. In case of a linear trend $n = 1$ has to be chosen and the data can be fitted by least square methods. From Fig. 3.5 it is clearly visible that

neither the subtraction of the mean value nor a removal of linear trends would be sufficient to detrend the detuning effect and its influence on the field.

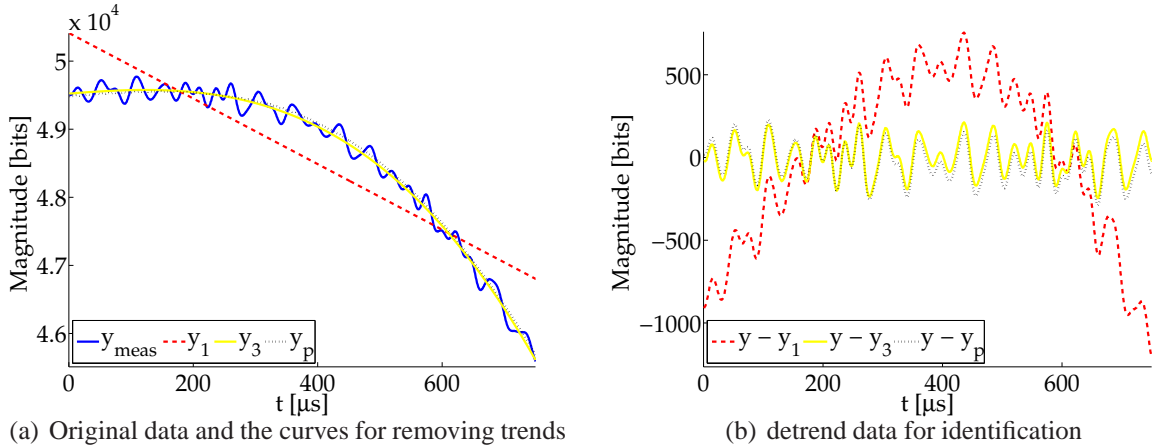


Figure 3.5: Comparison of the used detrend methods for preprocessing the data for identification. In (a) the data and the fits are shown before removing the detuning effect, in (b) the identification data after removing the trends is shown

The curve is superiorly detrended by subtracting a higher-order polynomial from the measured data set y_{meas} . Detuning effects cause a time-varying equilibria comparable with a polynomial of 3rd order, ($n = 3$) and are removed before identification because it is not a forced response to the excitation signal.

From Fig. 3.5 (b) it can be seen that compared to the linear detrend, the polynomial fit (y_3) leads to an almost constant and mean free system response for the identification data.

Finally a last possibility is introduced, which turned out to be the most effective because it was less sensitive to disturbances that occurred while taking measurement data. Often the data sets for identification are corrupted by errors out of the digital measurement equipment. As an example, crosstalk on the signals caused by other parts of the accelerator system have been observed. This results in jumps of the measurement signals (see. Fig. 2.13), which are known to be independent of the subsystem dynamics. Detected as an repetitive disturbance source, it can be easily removed by measuring the unexcited system response before applying the excitation signals. Averaging over several pulses or lowpass filtering might reduce stochastic noise contribution. The unexcited system response can be found in Fig. 3.5 (a) as y_p , and is subtracted like the detrending operation introduced previously. In comparison to the 3rd order polynomial fit no significant differences can be found, but this last method turned out to be most reliable and gives best fitting results. This becomes clear if linear behavior is assumed, so subtracting the normal system response to the feedforward should provide the system response to the excitation alone. Further considerations of this method of removing trends from disturbances can be found in the appendix A.1.

Averaging and time shifts

Measurement noise is generally unavoidable under real conditions. The detection equipment, sampling quantization and signal processing show a large variety of noise aspects. Usually it is possible to filter the data, e.g. with lowpass filters. The data sets are available offline so lag-free filters can be used. Most of the stochastic disturbances are in the high-frequency range, but filtering cannot be used for preprocessing due to possible higher frequency dynamics. In addition PRBS input signals have to be filtered as well. Another possibility is to average over several pulses when recording the excitation response

$$\hat{y}(t) = \frac{1}{n} \sum_{k=1}^n y_k(t) \quad , \quad (3.11)$$

where $\hat{y}(t)$ is the mean output signal of the same experiment output over n pulses. If $n \rightarrow \infty$ the stochastic error is ideally removed. In practice, a large number of measurements can be made by recording several pulses as already introduced. In Fig. 3.6, an example of the measured data (red dots) and the corresponding mean value is given.

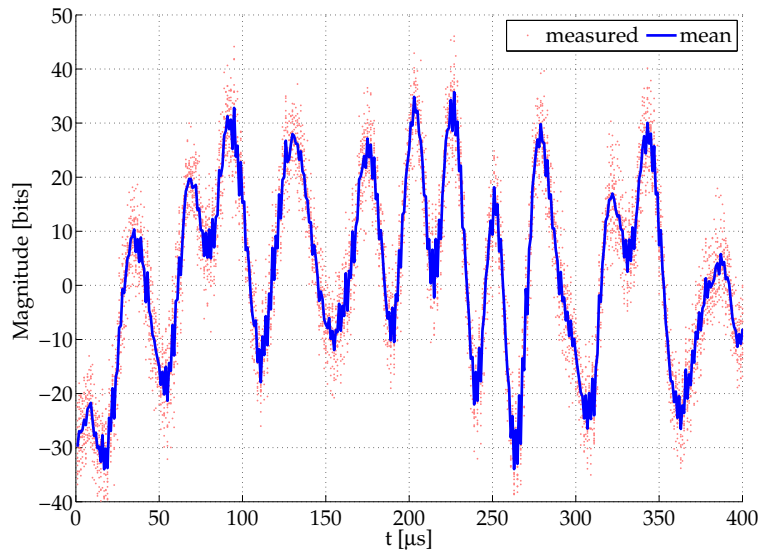


Figure 3.6: Measured data samples for the cross coupling elements show a spread regarding to noise and microphonic effects of the system. The excitation sequence remains unchanged, so the mean of the output signals gives the response in the low-frequency range of the system

In this case with one specific input signal, the system response is measured. This decreases measurement imperfections, which are introduced by, e.g., microphonics as described in Sec. 3.2.3. These pulse-to-pulse fluctuations are also removed by averaging.

The last and significant step in pre-processing is the treatment of system delays. Inspecting the system response in Fig. 3.7 a time delay of $t_d = 4\mu s$ can be estimated.

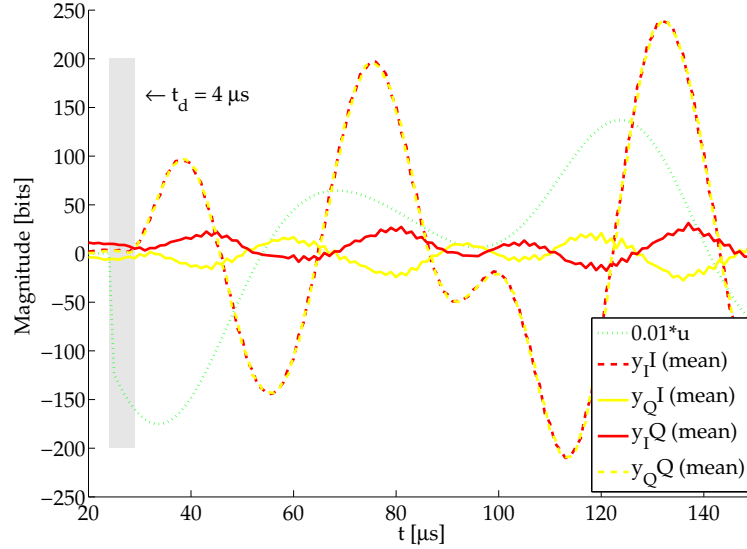


Figure 3.7: Measured system delay using open-loop identification data. The data sets of input u (only one channel shown) and the output channels y will be shifted in time to compensate this delay effect for the identification, preventing increased model order

Due to the processing steps and the field detection algorithm, a delay of about $2 - 4\mu\text{s}$ are introduced as described in Sec. 2.1.4. Delays are treated in state space models

$$\begin{aligned} \begin{bmatrix} x_1(k+1) \\ x_2(k+1) \end{bmatrix} &= \begin{bmatrix} 0 & 1 \\ 0 & 0 \end{bmatrix} \begin{bmatrix} x_1(k) \\ x_2(k) \end{bmatrix} + \begin{bmatrix} 0 \\ k_1 \end{bmatrix} u(k) \\ y(k) &= \begin{bmatrix} 1 & 0 \end{bmatrix} \begin{bmatrix} x_1(k) \\ x_2(k) \end{bmatrix} \end{aligned}, \quad (3.12)$$

by introducing additional states that behave like a shift register, as given in (3.12), where the response is stored in one state and further processed in the next sample step. This leads to an increased order in the model parameter estimation, which introduces higher complexity to the controller synthesis. For an estimated delay of $t_d = 4\mu\text{s}$, the system order is increased to $n + 4$. The identification data are modified by shifting the output data about $y(k - t_d) = y(k)$ while leaving the input data unchanged to compensate the time delay. These delay effects have to be taken into account when designing the controller, as discussed in chapter 4 and chapter 5.

Having summarized the pre-processing steps, the identification algorithm is outlined in the next Section, where it is assumed that the identification data is already pre-processed and is available as detrended input and output data sequences.

3.2.3 Subspace identification

The third step in the procedures is to estimate the model parameters using a state space model. Standard identification procedures for linear time invariant (LTI) models can be chosen to estimate black box models at specific setpoints, even though it is known that additional external disturbances and non-linearities in the actuator system are relevant when operating over a broad

range of operation setpoints. Using LTI models is advantageous because standard controller design methods can be used for design of the feedback and feedforward controllers. The suitability of this class of models for representing the system dynamics has to be studied. In future applications, it might be necessary to extend the models, but for this work the identified models are restricted to LTI systems.

In the following, the subspace identification method *N4SID* (Numerical algorithms for State Space Subspace System Identification), provided by Matlab System Identification Toolbox [22] is used to estimate the parameters A, B, C, D for the black box state space model. The advantage of subspace methods is that they do not make use of any optimization procedures. The system matrices are obtained by solving algebraic equations. For further information about subspace identification methods the reader is referred to [20], [21], and [23].

After this definition the system characteristics, data preprocessing steps and the identification algorithm, the measurement results from the identification process are now presented, where all the measurements were done on a real plant over an extended period of time, during which there was significant development of the data generation and acquisition processes. This development is reflected in the results presented.

3.3 Measurement results

As previously stated, the objective of black box system identification is to find a system description that describes the static and dynamic system behavior for a large number of sources. In general, distinctions can be made between deterministic and stochastic signals and between open-loop and closed-loop models. In the case of unstable systems, only closed-loop models can be identified. Fortunately, for this application, the system is open-loop stable, so identification can be performed either in closed-loop or open-loop, depending on the necessary system representation for the controller design. The generalized block diagram of a closed-loop system is shown in Fig. 3.8.

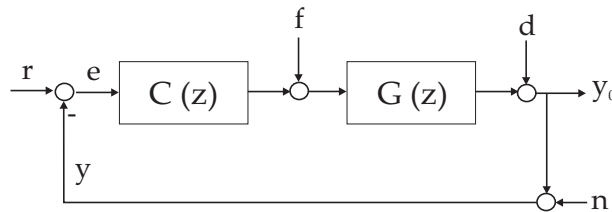


Figure 3.8: Block diagram of the closed-loop system with f as the feedforward input and d and n as plant disturbance and measurement noise configuration respectively. The reference trajectory is denoted as r , which gives by subtracting the measured system output y the control error e . The undisturbed output y_0 is representing the field seen by the electron beam, which cannot be measured directly.

The two open-loop input signals f are provided by the feedforward tables as described in Sec. 3.2.1, which are scaled such that in open-loop mode, the amplitude and phase of the field gradient is already approaching the desired values, as illustrated in the example in Fig. 2.3.

Rather than using calibrated physical units, the system responses are presented in the notation of *bits*, which vary during the individual results. Therefore the various measurement results are not directly comparable by absolute bit values. Furthermore, because of the frequent usage, the definition of on and off-diagonal elements is introduced. On-diagonal elements are the parts of the transfer function that define coupling between equivalent vector components, such as $u_I \rightarrow y_I$. Off-diagonal elements in this notation are the couplings between I and Q. The quality of the plant model is evaluated by comparing the simulated output with the measured output. This first comparison was made with the same set of input signals that were used for the identification. All other validations were performed with different data sets for identification and validation.

3.3.1 Model validation

Validating the estimated models is necessary in order to answer the question whether the model can be used for controller design. There are several methods available, namely:

- **Cross validation with unused experiment data:** Validation is performed using a different input/output dataset than was used during the identification procedure. The model should give an acceptable validation with this data so as to check whether the dynamics belong to the system or were caused by particular artifacts of the dataset. Furthermore data from excitations of different frequency ranges can be checked.
- **Comparing different models:** Compare models of different identification experiments e.g. frequency ranges, experiment times and system changes. Comparisons can be done for different properties, such as pole-zero locations, frequency and time-domain responses. The models should not vary more than an acceptable level to verify the usability.

In the following, some examples from estimated system models are presented. It should be clear from the ordering of the data how the modeling procedure has developed as experience was gained with the plant. Particular aspects of the data pre-processing and their influence on the model are discussed for each case. Limitations of the detectable system characteristics are outlined, and solutions for improving the models will be introduced. To begin, the open-loop modeling results are shown.

3.3.2 Open-loop modeling

The measurements presented in the following are examples from the large number of data that were recorded during this work. For the design of the feedback controller an open-loop model of the system is necessary. The system characteristics require preprocessing steps like detrending and averaging previously introduced. It is known, that the open-loop system is effected by the detuning, leading to strong trends to be removed as described in Sec. 3.2.2. It turned out that the subtraction of the un-excited system response (see Fig. 3.5 y_p) leads to best fits of detuning effect and further some unexpected behavior, e.g. disturbances introduced by crosstalk. This method is further applied for the rest of the presented results. In addition it is known that

especially in open-loop operation the system is fluctuating from pulse-to-pulse due to microphonics. Averaging as introduced in Sec. 3.2.2 over several pulses reduces these field variations adequately and therefore is applied in the following. An example of a cross validation data set for used open-loop models can be seen in Fig. 3.9.

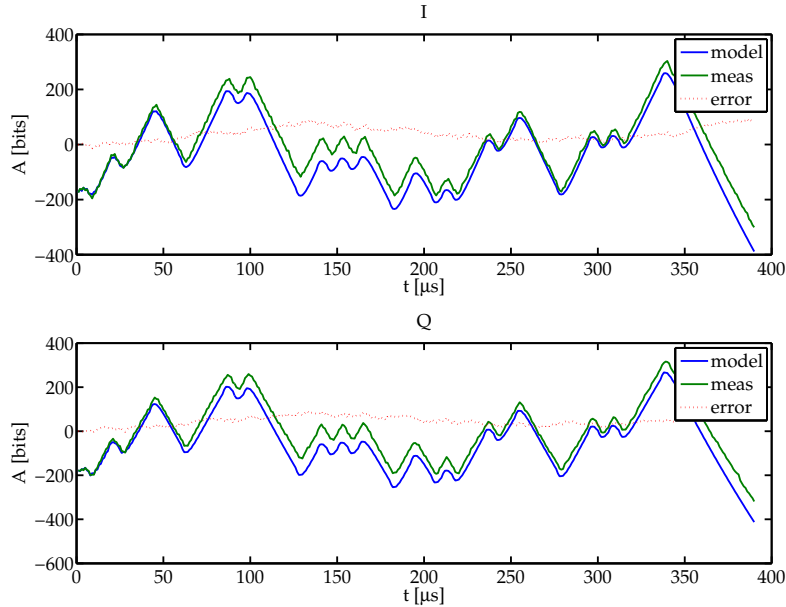


Figure 3.9: Cross validation data example of a third order open-loop model with excitation PRBS signals in both channels simultaneously

It is evident that this third order model is sufficient to represent the dominant system dynamics. Having a low order model, the controller synthesis complexity can be reduced. Several model orders have been tested, whereas increasing the order leads to introducing additional complex pole pairs on the subharmonic elements of the IQ sampling scheme described in Sec.2.1.4. The field detection leads to sampling steps residuals on the measured signals which are interpreted as harmonic oscillations. This is not caused by the excitation signals and therefore not part of the estimated model, but an outcome from the digitalization process.

From theory and step response measurements, the diagonal dominance of the system can be seen, i.e. the gain from $u_I \rightarrow y_I$ is much stronger than $u_I \rightarrow y_Q$.

Overestimation

Physical consideration indicate that the dynamic behavior is ideally equal for both channels, if assuming that the field detection is perfect. If the on-diagonal elements of the model do not represent this, then the model parameter estimation is corrupted, something that can be easily checked by observing the bode plot of the model. The identification procedure of exciting both channels independently turned out to improve the model quality in this case. In addition, tests have been made to excite the two input channels distributed over the flat top region, which leads to bad results because the detuning effects have a stronger impact at the end of the flat

top then at the beginning [28]. In addition, due to the very limited flat top time it is not feasible to further reduce the possible excitation bandwidth by splitting for both channels. Further it could be observed that the estimated parameters strongly depend on the pre-processing step of detrending, where slight fitting errors lead to strong differences in the estimated static gains of the model. Subtracting the open-loop system response from the excitation response turned out to be the best method to keep this modeling error small. The fitted polynomials vary from pulse-to-pulse, which further leads to strong model variation in the static gains. As an example cross validation of the estimated model with the combined excitation method can be found in Fig. 3.10.

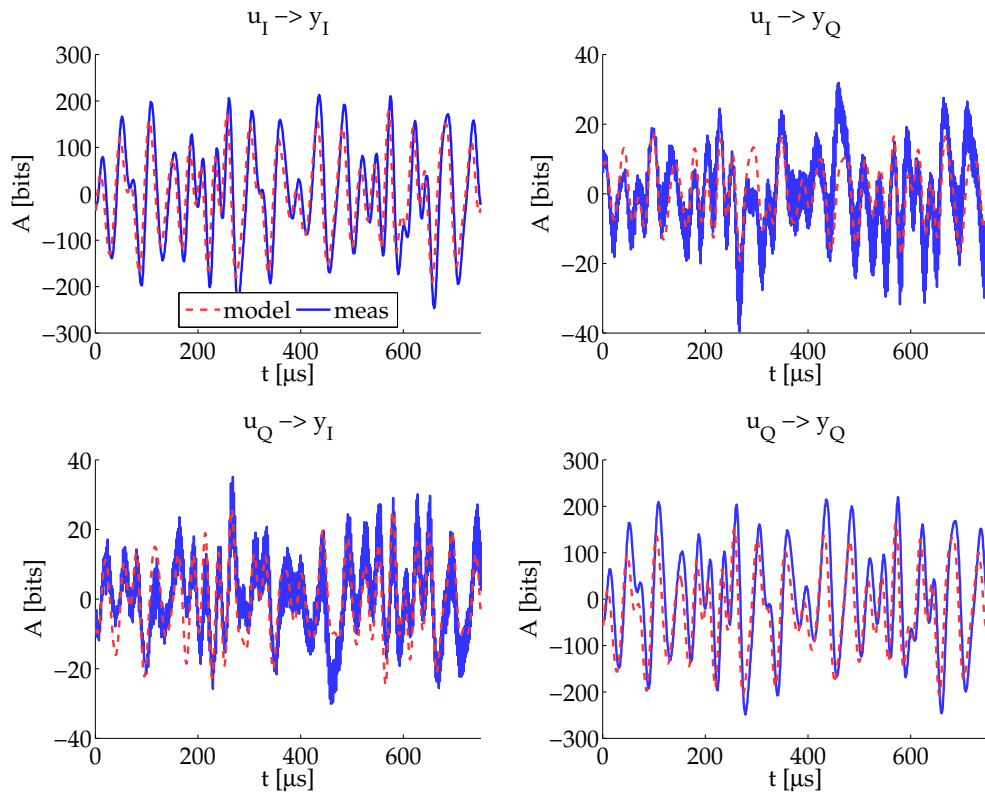


Figure 3.10: Cross validation of a 4th order open-loop system model identified with the combination method of partially excited channels

It can be observed from the cross validation that the estimated open-loop model gives a good representation of the measured system response in all channels. Also the off-diagonal elements are appropriately modeled, even with higher relative noise levels on the identification data. The response amplitude is almost 10 times smaller in these channels. From this figure, the assumed diagonal dominance as well as a similar dynamic behavior can be easily studied. A comparison between the different channels of the model can further be found in the bode plot given by Fig 3.11.

The diagonal dominance of the system is apparent and also the channels look similar in their

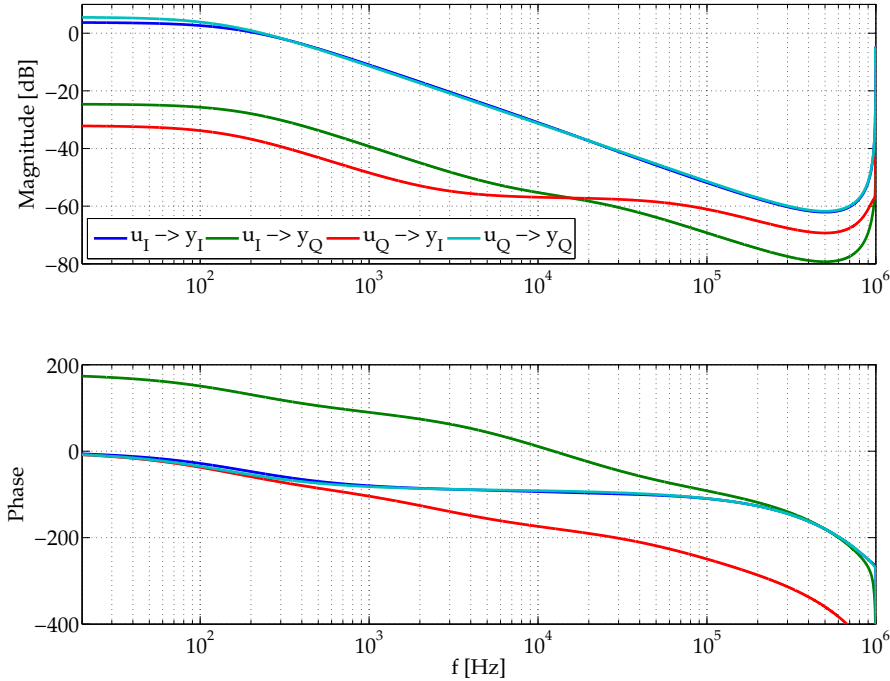


Figure 3.11: Bode plot of a 4th order open-loop system model identified with the combination method of partially excited channels

frequency behavior. The main difference comes from phase information in the off-diagonal elements where one channel is rotated by 180 degrees in phase. Here it can be seen that the identified model has strong similarities to the physical model (see Sec. 2.3.1) which has the diagonal dependencies.

3.3.3 Closed-loop modeling

Beside the open-loop model, it is further necessary to have also a sufficient description of the closed-loop dynamics in order to design the feed-forward controller that is discussed in chapter 5. The closed-loop model can be found either by combining the open-loop model with the model of the feedback controller, or through direct identification of the closed-loop model. Direct identification was chosen because it gives the possibility of identifying system characteristics not identified in the open-loop model. The estimation has been done by the same method and procedures as used for the open-loop identification. With references to Fig. 3.8, the excitation signal was again applied on the system input f , while $C(z) \neq 0$. This is the feedforward input signal that will be used and subsequently optimized by the feedforward controller during normal operation. The closed-loop model dynamics represent the transfer function from $f \rightarrow y$ as applied for the controller. When changing the feedback controller it is necessary to update this closed-loop model. The feedforward controller is assisting the feedback controller and therefore relies on the closed-loop system dynamics. Knowing that the excitation signal is superimposed by the feedback controller, equal conditions can be found for excitation and normal plant operation.

The stronger impact of the cross coupling elements are easily visible when comparing the closed-loop measured data amplitudes in Fig. 3.12 with the open-loop response shown in Fig. 3.10.

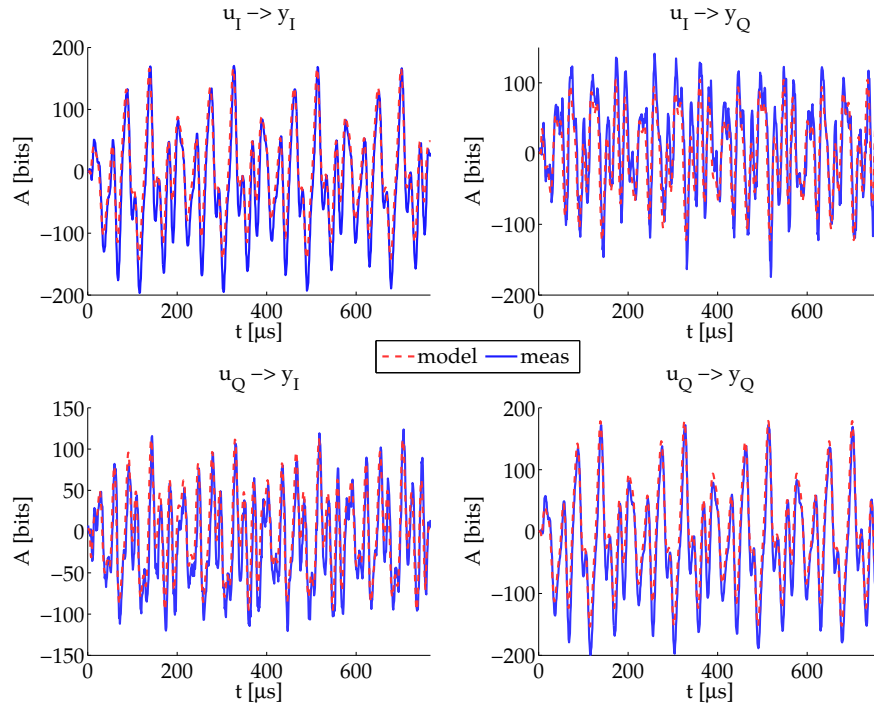


Figure 3.12: Cross validation of a 4th order closed-loop (proportional feedback gain 40) system model identified with the combination method of partially excited channels

The feedback controller leads to a stronger impact on the off-diagonal elements. The system response to excitation signals is faster due to the increased closed-loop bandwidth. The validation data set gives a sufficient model fit in the dominating frequency range. Influences to the higher frequency dynamics are discussed later. Here the dominating lowpass-characteristic and diagonal dominance as seen by the open-loop model can also be identified. The off diagonal elements show almost the same dynamic behavior, in contrast to the open-loop model given in Fig. 3.13.

Here it can be seen why it is important that the feedback controller has also cross term components like the MIMO controller. High-frequency dynamics are stronger coupled over the cross term components that arise from the feedback. For further discussion on the controller design see chapter 4.

In summary, it can be seen that the procedure for identifying open-loop and closed-loop models is sufficient to find good models for design of feedforward and feedback controllers. The same methods can be used for both design procedures. Taking data over a small number of pulses works very reliably. This makes the method useable during normal operation of the machine, where excitation signals could be applied for short times generating the system responses used as identification data, and all design procedures are performed offline. It can be seen that the system model does not change significant over time if no calibration changes or significant

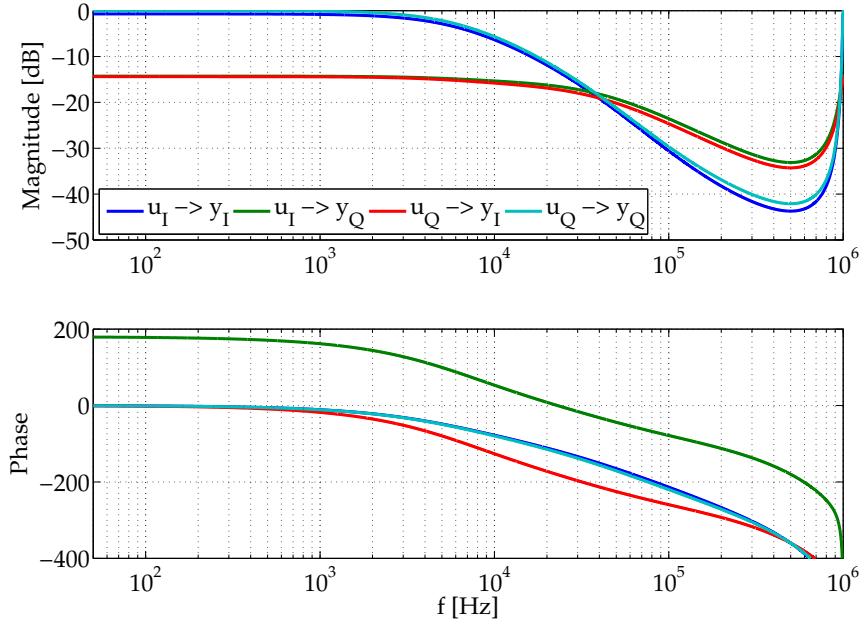


Figure 3.13: Bode plot of a 4 th order closed-loop system model identified with the combination method of partially excited channels

operation mode changes are performed. Validating the new model with old ones is possible and has been done.

An important aspect not discussed so far is the impact of an overall system delay from applying the excitation to the measured response. The dependencies and the resulting considerations to be made are discussed in the following.

3.3.4 System delay

As discussed in Sec. 3.2.2 there is a small time delay in the system response because of the long cables and from algorithms for the field detection, which add up to an input-output delay of about $3\mu\text{s}$ that must be taken into account when identifying the system model. It is well known that delays can lead to instabilities in closed-loop system. Furthermore, the closed-loop system might become unstable for particular time delays because of the additional modes, [8]. There is a significant improvement from removing the system delay from the datasets during pre-processing. With the delay compensation a significant improvement of the model fit can be achieved by having the same model order as shown in Fig. 3.14.

It is clear, therefore, that removing the system delay has a big influence on the later controller design procedure. Detecting the effective delay time from feedforward input to the measured output of the system will give a hint on possible shifting in feedforward tables to get the wanted response to the dedicated time. Additional measurements associated with delay compensation can be found in the Appendix A.1.

In this Section, it was shown how the processing methods influence the quality of identified black box models. Next, ideas are presented for modeling not only slow dynamics, but also any

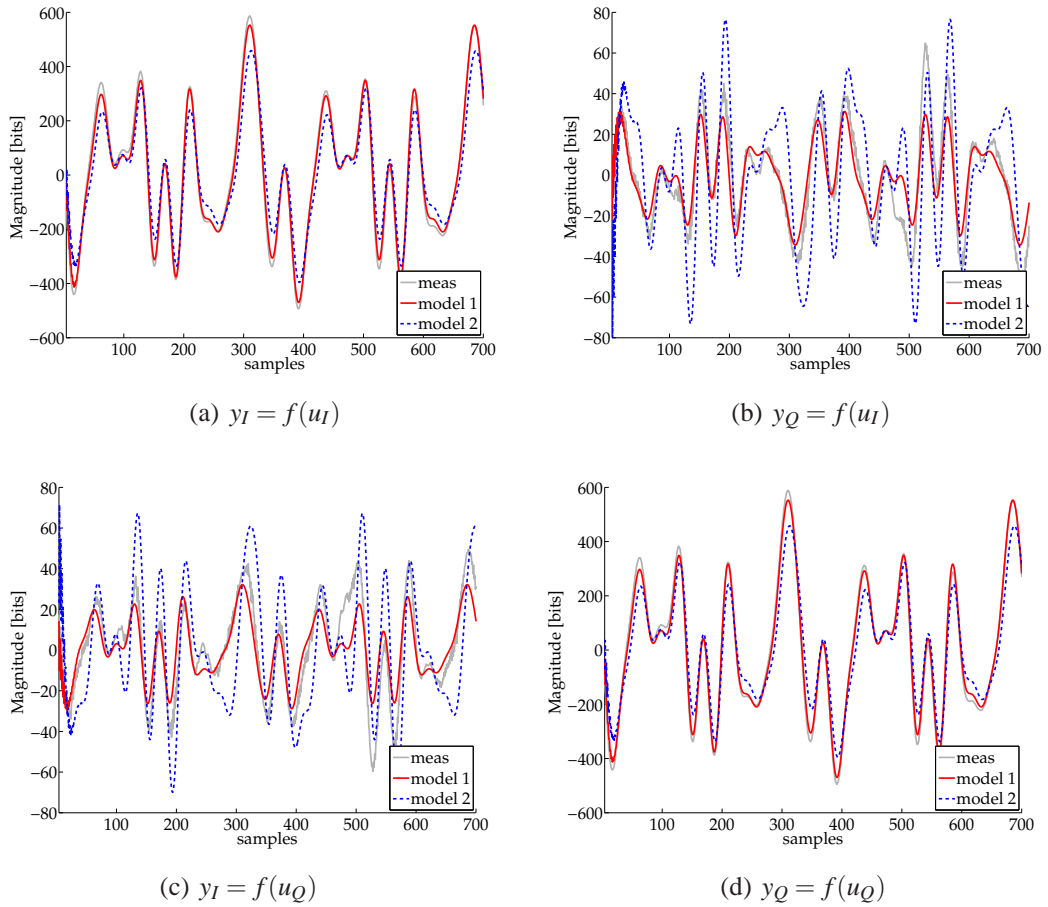


Figure 3.14: Comparison between the delay compensated model (1) and uncompensated model (2). Both models have equal order 3, and the system delay was detected to be $4\mu\text{s}$.

high-frequency dynamics that might be present.

3.3.5 Model extensions by higher frequency dynamics

It can be seen that the models identified so far are dominated by the cavities lowpass characteristics. Knowledge of the physical plant suggests there are also higher-frequency dynamics coming from the coupled-cavity modes. Unfortunately, identification of these higher frequency dynamics is difficult because measurement noise cannot be lowpass filtered. Averaging would suppress the high-frequency dynamics if there are phase shifts over several pulses. Consequently, another way has to be found to extract this information so the model can be extended to include high-frequency dynamics.

One possible approach is to excite the plant with steady-state sinusoidal excitation signals, as will be described in the next Section.

Response to sinusoidal inputs

For controller design it is important to know if there are any specific frequency ranges where the system contains modes that destabilize the closed-loop system. It was found by broad band excitation, that the system does not show these modes, even though there are known to exist from physical considerations and closed-loop operation with high gains. Subsequently, additional tests were performed where the system was excited during the flat top region by using sinusoidal input signals (see Fig. 3.4) in a given frequency range. To illustrate the effect of resonances in the system, the time domain system output is shown for the sinusoidal excitation with frequencies on and off the resonance frequency in Fig. 3.15. Here it is clearly visible why the continuous frequency excitation is necessary to identify this mode. After some transient time the oscillations reach an amplitude which is measurable. This method allows to detect several resonance peaks when sweeping through a defined frequency range.

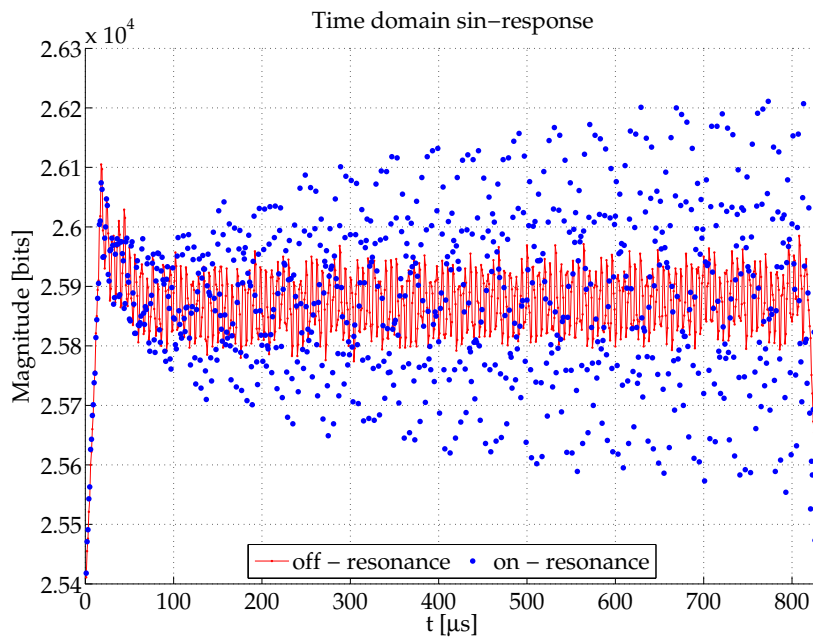


Figure 3.15: Time domain response with and without excitation on resonance

One possible explanation for not detecting these resonance peaks with the original excitation signal, even with a small excitation bandwidth is that the effect was small compared to the noise level, because of the weak input power to this mode and the transition time until the oscillations are visible. To find this peak, sine-waves were used to excite the system at particular frequencies and over the whole flat top. Having measured system responses over all the excitation frequencies, several resonances can be easily identified, as shown in Fig. 3.16.

The plot shown in Fig. 3.16 was generated by taking the frequency spectra of the input signal and output signal for the given frequency point and subtraction of the input and output signal in logarithmic scale. In the figure several resonance peaks can be observed. The first resonance peak is assumed to be the aliased component of the $\frac{8}{9}\pi$ -mode. The considerations leading to

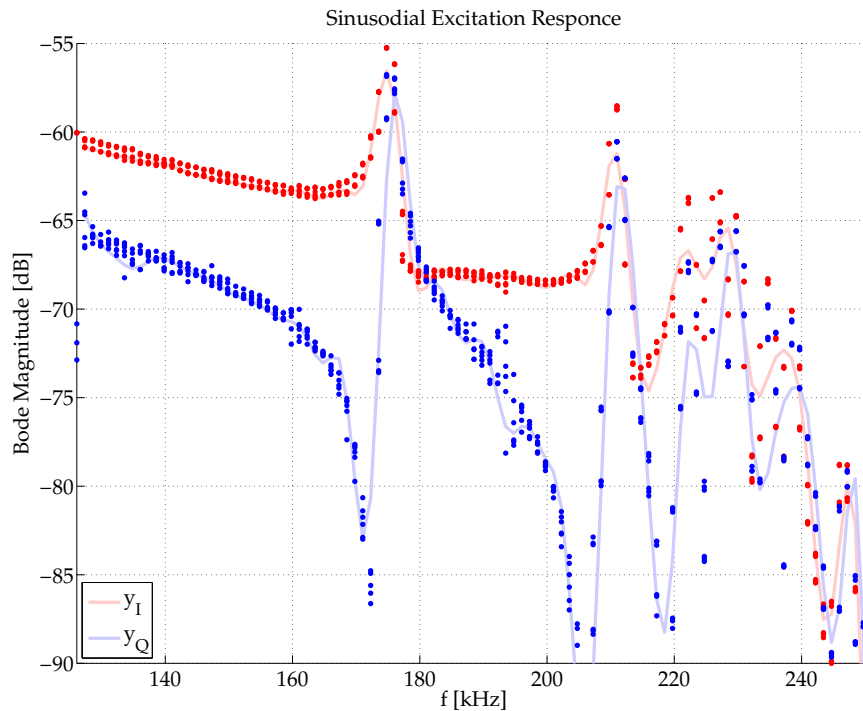


Figure 3.16: System response to sinusoidal excitation signal sweeping frequency in the I-channel. The responses are given for both channels, showing resonance peaks at approx. 174 kHz and 212 kHz.

this assumption are sketched in Fig. 3.17.

This special mode can be found about 825 MHz below the carrier frequency of 1.3 GHz. In order to prevent aliasing effects, it is usual to filter analog signals prior to sampling using a so-called anti-aliasing filter. Additionally, the well known Shannon theorem must be fulfilled, [27]. For a sampling frequency of 1 MHz, signals above 500 kHz would ideally be filtered out before sampling. In this application however, the field detection procedure discussed in Sec. 2.1.4 does not allow the use of anti-aliasing filters since the I and Q components of the field are detected in steps so the filter would smooth the steps for I and Q, having negative effects to the field detection.

The fundamental modes are aliased in this case to the measured frequency range as sketched in Fig. 3.17. Therefore the estimated controllers must not excite especially this mode due to the fact of causing oscillations in the control system.

It is worth noting that changing the intermediate frequency would also influence these aspects, as would the use of other sampling schemes, such as direct sampling with fast ADCs. The considerations done here can be applied for any other field detection procedures, whereas the model especially in the high-frequency range will probably show different behavior as given here. Detection of these resonance peaks turned out to be challenging. Recent measurement results however turned out to give possible solutions to this issue. Further details can be found in [29].

Having made these measurements once, one can find out whether or not the resonances are

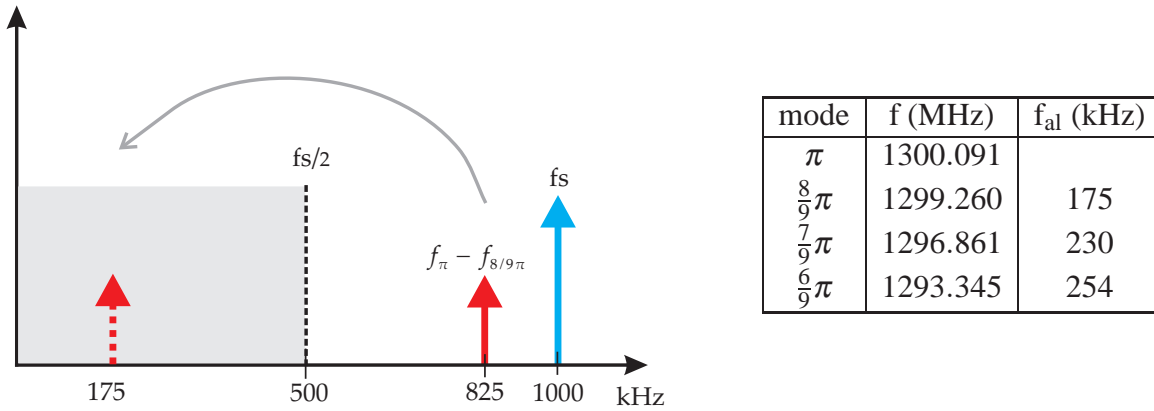


Figure 3.17: Example of aliasing effect of the fundamental modes. The table on the right shows the estimated aliased frequency f_{al} in the nyquist band while aliased on the baseband sampling and there higher harmonic components.

changing over time. Usually they stay the same and can be found just by sweeping around this bandwidth to get the information. Alternatively, checking the validity of the old model could be included in maintenance procedures for the system, so as to verify that the previous controller is still applicable. Furthermore it is possible to limit the frequency from PRBS signals to this range, and applying identification methods used so far.

In the following section, we will discuss incorporating knowledge of significant resonance peaks into the system model and then into the controller design.

Combining system responses

Having found these resonance peaks in the system, the model can be extended by this knowledge to give a better approximation of the high-frequency system dynamics. This leads to a better prediction of stability boundaries for closed-loop operation.

As a first possible solution, tests were made to see whether the different identification data sets could be merged into a single representation of both, the excitation with PRBS signals and excitation with sinusoids of constant frequency. This system will show a significant increased order due to the sharp resonance peaks and their corresponding model. Furthermore, there is a significantly higher computation time because of the large number of data sets needed to take into account every single frequency excitation. For offline generation of the model this would be acceptable, but it would be unsuitable for frequently model updates during normal user operation, for example if the operation point is changed.

Averaging data from several measurements turns out to have negative influence on the resonance modeling because the emerging oscillations are time shifted over a series of pulses and are therefore canceled out by averaging. In Fig. 3.18 bode plots of the identified model are shown. It can be seen that the resonance peak extends the lowpass characteristic of the model at the frequencies identified by the sinusoidal sweeping in the diagonal component $I \rightarrow I$. In the off-diagonal element this characteristic can not be found, whereas the resonance peaks are at the same frequency.

This method seems to have some beneficial effects in the higher frequency range but also a

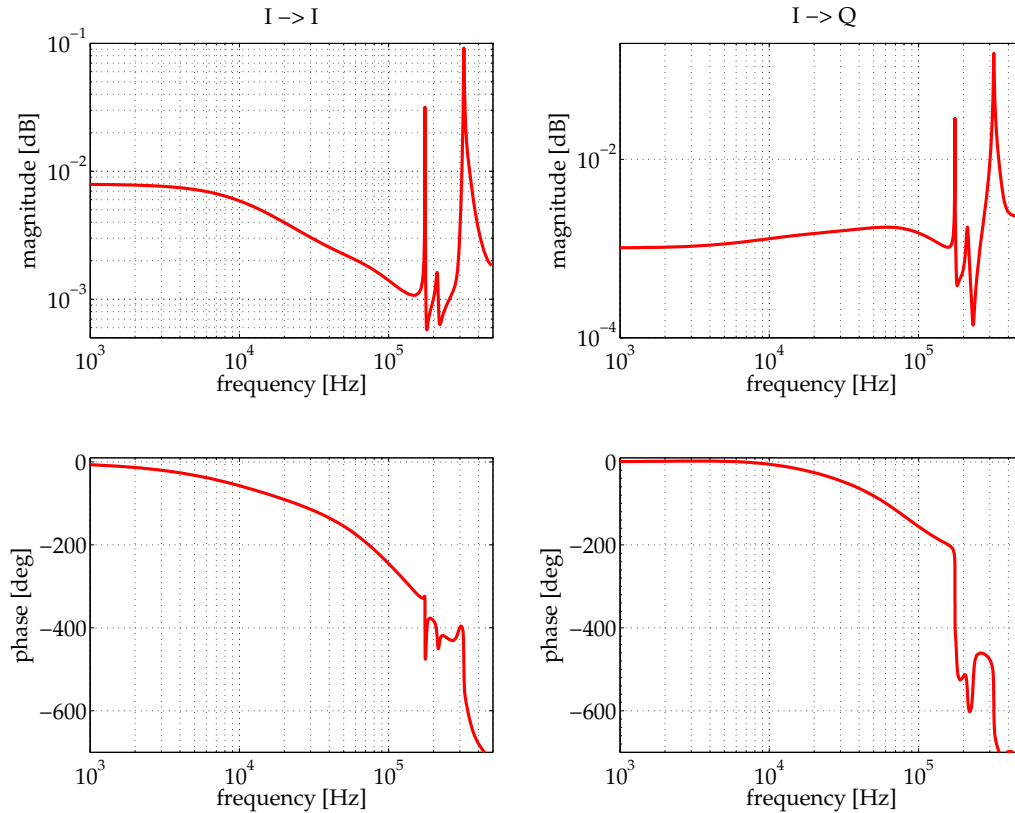


Figure 3.18: Bode diagram of a 12th order model identified by combination of PRBS excited and sinusoidal response data for excitation in the I channel, [29]

drawback when considering the low-frequency response in the off-diagonal element. Knowing the specific peaks, it is also possible to use the function *n4sid* of the identification toolbox to define the frequency areas of interest to improve the modeling. The excitation signals must have an appropriate bandwidth as discussed before. Sweeping over the whole frequency range to identify the critical points is no longer necessary which also reduces the time for generating measurement data. In the last Section this recent results are given.

3.4 Model and conclusion

It has been seen that system identification is a challenging procedure that demands a priori knowledge of the system characteristics. An appropriate excitation signal is the most important key because dynamics that have not been excited are not measured and therefore cannot be modeled. Various signals have been tested in order to find an appropriate input sequence, and it turned out that the combination of several input signals with different frequency ranges is the most effective. Due to the high Q-factor of the cavity, the system bandwidth is very low, which has a strong influence on the identification procedures. In all models it is possible to determine the lowpass-characteristic that dominates the system dynamics, while knowledge of

the other fundamental modes in the system and the aliasing effect has lead to a more detailed study of the high-frequency behavior. Some preprocessing steps are not applicable and the identification procedure must be adapted to generate the necessary data sets. Just increasing the model order and using broad band excitation does not necessary lead to a good model quality. Modeling errors in the static gains turned out to be strongly depended on the detrending method applied. The short identification period and the corresponding low system bandwidth leads to modeling difficulties especially in the low-frequency range. The combined channel excitation for the two input channels turned out to improve the quality of the model, especially in the off diagonal elements of the system. All tested methods for excitation and preprocessing are summarized in Tab. 3.1. The ratings given for the individual methods can be taken as guideline on which methods might be used in the permanent plant system identification procedure. Taking into account all these factors, it was possible to identify a model that has a bode plot given in Fig. 3.19.

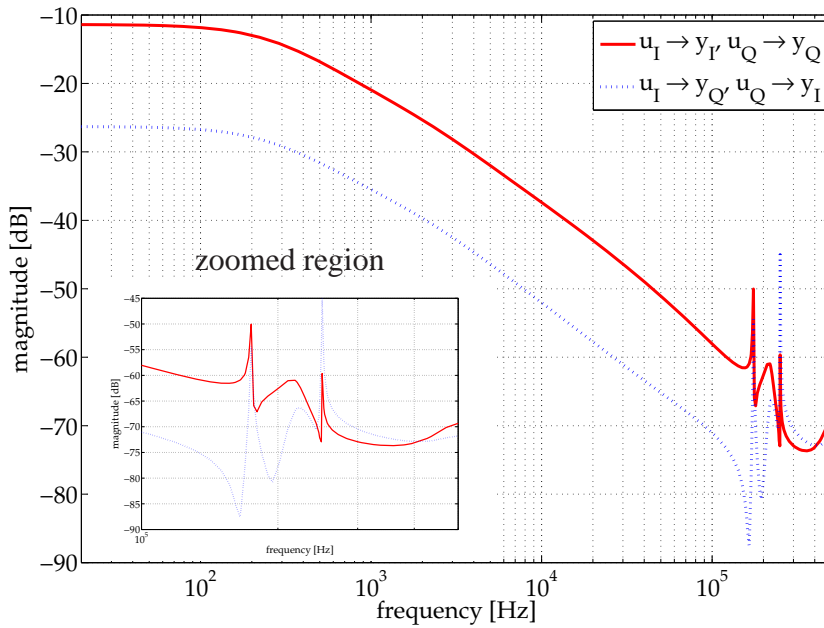


Figure 3.19: Bode Amplitude diagram of a 11th order model identified by weighted and merged PRBS excited, averaged parameter combined system responses. The mean of both corresponding channels is taken to get the equal behavior in the system dynamics. The resonance peak at 174kHz (aliased mode) can be identified in the black box model, [29]

This plot shows the recently developed system model that incorporates all the expertise gained during the modeling steps described before. Here the respective coupling elements are forced to show same behavior as known from the physical description of the system.

Comparison to physical description

One can easily observe that this model shown in Fig. 3.19 is similar to the physical model of the cavity given in Sec. 2.3.1. The diagonal dominance is modeled well and the high and

low-frequency dynamics show the expected behavior of the cavity as observed after the digitalization process. The first resonance peak at about 174kHz is assumed to be the aliased $\frac{8}{9}\pi$ -mode as discussed before. The second sharp peak at about 250kHz is ascribed to be an influence by the sampling frequency of 1MHz. As mentioned the identification was forced to get the same behavior for the corresponding elements of I and Q in the MIMO system. From the physical point of view these elements must show the same behavior except some disturbances are present in the field detection algorithm. The phase shift of 90 degrees should not have any influence on the dynamic behavior in the system, furthermore the field detection algorithm mixes these channels when computing the components in the controller discussed in Sec. 2.1.4. This is also true for the cross coupling components, whereas the phase is rotated by 180 degrees in one channel. When modeling the system these considerations must be taken into account and additionally they are helpful to validate the model. Because the identification was done only during the flat top time, data detrending must be done with care as was discussed previously as well as the combination of the consecutively identified channels. Comparing the bandwidth of the physical and identified model, it is clearly visible that the low pass characteristic is dominant. Especially when keeping the model order very small one can compare both state space representation in a good way. Nevertheless LTI black box models have advantages compared to the physical model, especially when considering the gained expertise for future identification tasks. Independent validation of these claims would be performed once a different sampling scheme is used for data processing. For further modeling, it is also possible to try a given structure in the identified model, which is known as grey box model. Recent results on this topic can be found in [29]. Beside this, some more thoughts about the system modeling are done in the final paragraph.

Further ideas

The model discussed so far is only valid under the given assumptions and the current machine setup and will probably change in the future due to system upgrades, different hardware setups or field detection algorithms. The system model must be adapted to take these changes into account. It is also planned to operate the whole system on a higher gradient which means the klystron will be closer to saturation. The linearity assumptions must be revised in this case and the model might be valuable for a limited area around the operation point. Additionally piezo sensors and actuators will be used to reduce the cavity detuning during the pulse. This will have a strong impact on the system dynamics which have to be taken into account. Furthermore these actuators can be used to support the feedback control loop that will extend the current MIMO system structure by adding channels that provide coupling between field and detuning.

Finally it has to be taken into account that the field regulation can be considered as an actuator for the real object to be controlled, the electron beam. Development in the beam measurement devices allows information to be gathered directly about the quality of field regulation by measuring beam imperfections. RF fields and electron beam acceleration depend on each other, which opens the door to further improvements by changing the control structure in a way that beam measurements are incorporated in the inner FPGA loop or the outer ILC loop.

The combination of RF, mechanical systems on the cavity and beam information must be merged in an appropriate system model to show these dependencies in the general case of a MIMO system. This is the only way of designing a controller which allows to handle different

actuators and sensors to an optimal beam regulation, a reliable feedback system with control loops are defined together in a full closed-loop system description.

Table 3.1: Overview of tested identification procedures

<i>method</i>	<i>rating</i>	<i>description</i>
PRBS	++	The signals are easy to realize by standard methods. Bandwidth and amplitude can be chosen regarding experimental conditions.
chirped sinusoidal excitation	+	The signals are easy to realize by standard methods. Bandwidth and time varying amplitude can be chosen regarding experimental conditions.
const. sinusoidal excitation	o	Method is only used for resonance peak detection and not directly for system identification. Improved the plant knowledge and choice of identification signals.
combining channels	++	Prevents the overestimation of the cross coupling terms. Additional validation method by comparing the different channels
sequence merging	+	Broad band excitation can be realized by different narrow band regions. Combination of different excitation signals.
linear trends	--	Not sufficient for detrending due to higher-order detuning effect. Estimated models give non sufficient validation results.
polynomial trends	+	Good fit to detuning effects. Leads to almost mean free excitation response.
unexcited system response	++	Best fit to detuning effects and further disturbance influences. Data mean and trend free due to removal of unexcited system response.
averaging	+	Removing of stochastic noise contributions and outliers. Noise model cannot be estimated from the data.
time shift	++	Model order can be decrease. Cross validation data set show significant improved fit. Must be considered during controller design.

Chapter 4

Feedback Control

Disturbances such as those introduced in Sec. 2.2 are common in real systems. In order to achieve disturbance rejection and good reference tracking a feedback controller is used. The RF field control task can be defined as keeping the measured vector sum on the given setpoint trajectory during the RF pulse. For this task the feedback controller is assisted by a pulsed feed-forward drive waveform that has constant shape and that forces the system to almost achieve the reference trajectory. Residual small excursions, especially pulse-to-pulse fluctuations, must be regulated by the feedback controller. To date, two independent proportional feedback controllers have been used to regulate in-phase and quadrature (I and Q) components of the RF field vector sum, but the performance has been inadequate to meet the requirements defined in Sec. 1. This work introduces a multi-variable higher-order feedback controller to improve the regulation performance. The necessary controller parameters have been estimated and the controller has been tested on the plant (the FLASH accelerator).

It is known from chapter 3 that the plant has a very narrow open-loop bandwidth and dynamics that have a similar timescale to the RF pulse length. The controller must be designed to sufficiently increase the system closed-loop bandwidth in order to achieve fast disturbance rejection without destabilizing the closed-loop system and while minimizing amplification of measurement noise. It is already known that the closed-loop bandwidth cannot be sufficiently increased to suppress high-frequency disturbance contributions. Fortunately, disturbances such as transient beam-loading effects are repetitive from pulse-to-pulse and can be compensated using the feedforward controller. Disturbances are correspondingly classified as listed in Sec. 2.2. The main objective of the feedback controller in this case will be to minimize the pulse-to-pulse fluctuations of the measured vector sum.

The controller parameters have been estimated using the well known mixed sensitivity design method, [30], [32], [33]. This model-based design method allows the parameters of the fixed-order controller to be estimated using the H_∞ norm that has the benefit of being robust against model uncertainties. Presented here are results from measurements taken on real accelerator systems using this controller design method.

This chapter is organized as follows: In Sec. 4.1, the structural implementation of the feedback controller will be introduced, giving particular consideration to the system constraints; the controller design procedure is discussed in Sec. 4.2 and measurement results from tests on the plant will be presented in Sec. 4.3. Finally, further steps in the controller design will be given in Sec. 4.4.

4.1 Controller implementation

In the present system, independent proportional controllers are used for in-phase and quadrature terms, with the proportional gain being the only tunable parameter. The controller is implemented as a digital control system inside an embedded FPGA, with each 2ms RF pulse being managed as a separate event. Each RF pulse is treated as $N = 2048$ sampling steps that are processed in real time, after which the data acquisition is turned off until the next pulse. Between RF pulses it is possible to apply changes to the control tables. For each sampling step within the RF pulse, there exists a single proportional factor (gain table) that is a function of the feedback gain and a calibration constant. The relevant value in the gain table is multiplied with the control error e and then added to the feed-forward signal. While this gain table makes it in principle possible to implement a time-varying gain over the duration of the pulse, to-date only a single stable gain factor has been used.

The feedback controller maps the control error e_I and e_Q to the controller output u_I and u_Q as follows:

$$\begin{bmatrix} u_I(z) \\ u_Q(z) \end{bmatrix} = K(z) \begin{bmatrix} e_I(z) \\ e_Q(z) \end{bmatrix}, \quad (4.1)$$

with $K(z)$ the feedback controller. For the separate I/Q proportional controllers, $K(z)$ simplifies to K as:

$$K = K_p \begin{bmatrix} 1 & 0 \\ 0 & 1 \end{bmatrix}, \quad (4.2)$$

where K_p is the proportional gain factor to be chosen. The feedback controller must appropriately compensate the vector sum field error, which can be distinguished in the fluctuations both from one pulse to the next and within each individual pulse. Usually the reference signal remains unchanged for several pulses, so the fluctuations measured from pulse-to-pulse are caused by measurement noise, input disturbances and by microphonics inside the system, as discussed in Sec. 2.2.

4.1.1 Limitations of the closed-loop system

As described in chapter 3 the system response is dominated by the lowpass characteristic of the cavity. Additional resonance peaks can also be observed, and these have a strong impact on the closed-loop stability. Delays caused by the digitization process have a further impact on the closed-loop stability. The combined impact of these factors is to significantly reduce the range of achievable feedback controllers. Reference tracking is improved by increasing the feedback gain to give a higher closed-loop bandwidth and faster system response. Unfortunately this also amplifies the regulator response to measurement noise, which is then injected into the system. Resonance peaks in the system significantly reduce the gain margin over that of a simple lowpass filter. For example, the so-called $\frac{8}{9}\pi$ -mode frequently can destabilize the system in closed-loop operation. The destabilization effect is dependent on the overall loop delay. For further details the reader is referred to [8]. The gain margin can be further reduced by the phase lag caused by the digitization loop delay.

It is important to note that, ultimately the parameter to be controlled is the energy gained by the electron beam as it passes through the cavity, which is the result of the cavity RF voltage at the instant the electron beam passes through. This means that not all electron bunches will have the same energy gain if the cavity field fluctuates from pulse-to-pulse or within the pulse. The primary goal is therefore to keep these energy fluctuations as small as possible. Indeed, RF cavity field regulation tolerances are derived from the maximum allowable energy deviations. The electron bunch energy fluctuations will be minimized by stabilizing the measured cavity vector sum, provided the measured vector sum exactly represents the actual vector sum. Unfortunately, it is not possible to exactly measure the real vector sum because of calibration errors, measurement noise, and because of errors in the digitalization process. This leads to the statement:

- A perfect RF field regulation does not necessary lead to a perfectly stabilized beam acceleration!

During this work, only the measured cavity field information could be used for feedback regulation, while beam-based measurements were used to validate the measured vector sum control performance. Later measurements showed that the field regulation could be improved by using both, beam information and the cavity vector sum in the feedback regulation.

For a proportional controller the residual error is reduced by the gain factor. Fig. 4.1 shows the measured beam energy stability as a function of the feedback gain.

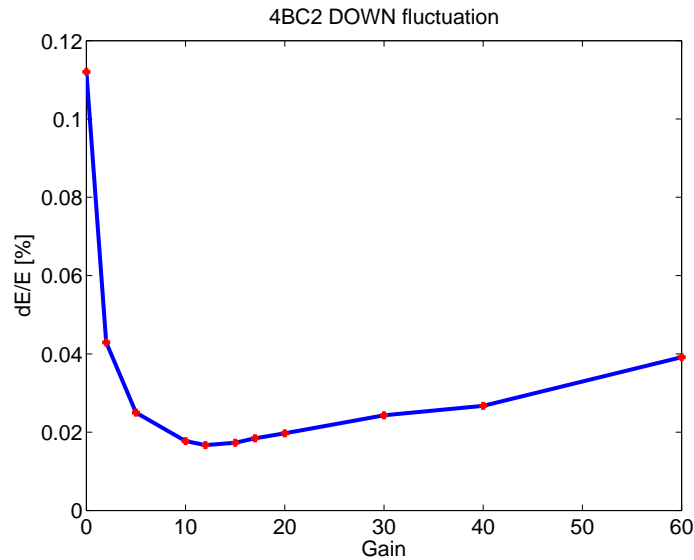


Figure 4.1: Relative pulse-to-pulse fluctuation of the electron beam as function of the proportional feedback gain, measured with the synchrotron radiation camera (4BC2DOWN)

It can be observed, that there exists an optimal feedback gain to minimize the measured beam energy fluctuation. By increasing the feedback gain, the bandwidth of this closed-loop system increases. This further results in feeding measurement noise back to the system input, which in this case results in an increased beam energy fluctuation. For further details refer to [35].

The question is whether or not a controller can be found that reduces beam energy fluctuation, keeps the system stable, and is robust against measurement noise. Performance of the independent in-phase and quadrature proportional feedback controllers is limited in part because there are cross-coupling components between the real and imaginary part of the field vector as a result of detuning effects. Since this cross-coupling should be taken into account in the feedback controller design, a multiple input / multiple output (MIMO) controller (comp. Fig. 4.2) is introduced as an upgrade to the existing controller, [36]. Considerations of the controller structural implementation will be discussed in the following section.

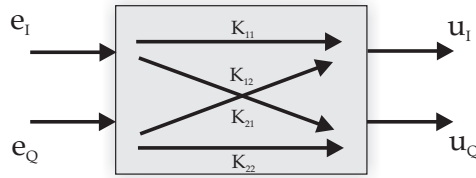


Figure 4.2: Schematic view of the multiple input, multiple output (MIMO) implementation in the feedback controller. Within the decentralized controller the cross coupling components K_{21} and K_{12} vanishes.

4.1.2 Structural design

The necessary low latency response in the control loop can only be achieved by implementation of the feedback controller in a digital platform based on an FPGA. In case of the proportional feedback controller the implementation is very simple. Conversely, the MIMO controller significantly expands the computations to be processed, in part because it must implement the cross-coupling dynamic terms. Due to memory limitations in the FPGA, each channel of the MIMO controller is restricted to second-order terms. The MIMO controller implementation is represented in Eqn. 4.1 as a 2×2 matrix:

$$K(z) = \begin{pmatrix} K_{11}(z) & K_{21}(z) \\ K_{12}(z) & K_{22}(z) \end{pmatrix}, \quad (4.3)$$

with the elements

$$K_{ij}(z) = k_{ij} \frac{a_{ij} \cdot z^{-2} + b_{ij} \cdot z^{-1} + 1}{c_{ij} \cdot z^{-2} + d_{ij} \cdot z^{-1} + 1}. \quad (4.4)$$

This is a second-order digital IIR-filter having 5 free parameters per channel that must be determined by the user. The block diagram in Fig. 4.3 represents one channel of the IIR filter as it is implemented on the FPGA.

The data processing is done in binary fixed-point arithmetic, so additional scaling factors must be applied by bit shifts in the processing units. If now the parameters are able to be chosen arbitrary it is necessary to implement the computation with a high accuracy to prevent overflowing and precision losses. Once an appropriate set of achievable parameters has been found it might

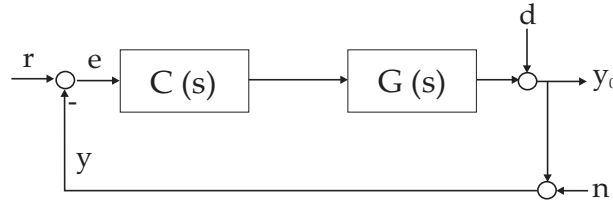


Figure 4.4: Standard feedback loop with Controller $C(s)$ and Plant $G(s)$ and the signals r, e, u, d, y and n denoting the reference, error, plant input, output disturbance, system output and measurement noise contributions respectively.

input/output definition. ”In the following, two basic transfer functions necessary for the mixed-sensitivity design are emphasized.

System functions

The transfer function from the disturbance input to the system output $d \rightarrow y$ is called the *sensitivity function* $S(s)$ of the closed-loop system,

$$S(s) = (I + G(s)C(s))^{-1} \quad . \quad (4.5)$$

In addition one can find another transfer function referred to the *complementary sensitivity function* $T(s)$:

$$T(s) = (I + G(s)C(s))^{-1}G(s)C(s) \quad , \quad (4.6)$$

which is the transfer function from the reference input r to the system output y , and is also the transfer function for the noise input n to the system output y . Inspecting both transfer function, it is clear that:

$$S(j\omega) + T(j\omega) = I \quad \forall \omega \quad . \quad (4.7)$$

Design objectives can be formulated in terms of these transfer functions, given as follows:

- **perfect tracking:** The controller should ideally keep the measured system output on the reference trajectory, which implies that $T(s) = I$.
- **disturbance rejection:** Real systems are generally disturbed by environmental influence which is given as the disturbance contribution. This disturbances should have ideally no impact on the measured output, demanding that $S(s) = 0$.
- **noise rejection:** Usually when generating measurements the data are noise corrupted by measurement equipment. Due to the system feedback this contribution is applied again to the control loop which influences the system output. Ideally the output is not affected by the noise, demanding that $T(s) = 0$.

Clearly, the design objective of noise rejection conflicts with the first two objectives, so it follows that a controller must be found which tracks the reference trajectory well but without feeding measurement noise back into the system. An additional constraint comes from the fact

that the actuators of the system have limited power, meaning that the plant input u is physically limited. This becomes clear when considering reference tracking, which is not possible for arbitrary high frequencies, e.g. jumps in the reference signal which cannot be followed perfectly.

The mixed sensitivity design method is used to fulfill these objectives, and this is discussed in the next section.

4.2.2 Generalized plant and weighting filters

In modern control theory, the so-called generalized plant is often used in the controller design process. In the block diagram in Fig. 4.5, the generalized plant comprises the elements inside the dotted lines. Usually disturbance and noise contributions are defined as external inputs, but in this case the desired (reference) output is given as the system input. The fictitious system outputs z_S and z_T are filtered through so-called weighting filters W_S and W_T .

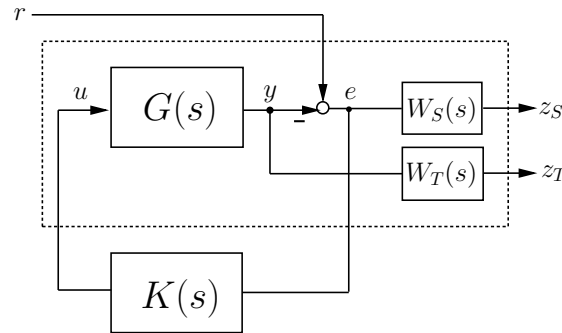


Figure 4.5: Block diagram of the generalized plant with the plant model G , the controller K and weighting filters W_S and W_T . The input and output signals are the system reference input r and the fictitious plant output z_S and z_T

The general idea of the weighting filters W_S and W_T is to obtain a desired closed-loop behavior. Using these filtered output signals, it is possible to shape the sensitivity and complementary sensitivity functions using the H_∞ norm. Following [32] the shaping filters for the MIMO case usually are chosen to be diagonal as:

$$W_S(s) = \begin{pmatrix} w_S(s) & 0 \\ 0 & w_S(s) \end{pmatrix} \quad ; \quad W_T(s) = \begin{pmatrix} w_T(s) & 0 \\ 0 & w_T(s) \end{pmatrix} \quad (4.8)$$

with $w_S(s)$ and $w_T(s)$ being scalar weighting filters for each system output. From Sec. 3.4 it is known that the two channels I and Q are phase rotated vectors having almost the same dynamic behavior, so it follows that the matrix of weighing filters can be diagonal, as given in Eqn. 4.8. The closed-loop transfer function is then defined as:

$$\begin{pmatrix} z_S \\ z_T \end{pmatrix} = \begin{pmatrix} W_S(s) S(s) \\ W_T(s) T(s) \end{pmatrix} r \quad . \quad (4.9)$$

The requirements on the closed-loop system can be achieved by designing the weighting filters such that the resulting closed-loop transfer functions fulfill the H_∞ constraints, as [32]:

$$\sup_{\omega} \overline{\sigma} \left[\begin{pmatrix} W_S(j\omega)S(j\omega) \\ W_T(j\omega)T(j\omega) \end{pmatrix} \right] < 1 \quad , \quad (4.10)$$

usually the H_∞ norm is minimized:

$$\min_K \left\| \begin{pmatrix} W_S S \\ W_T T \end{pmatrix} \right\|_\infty \quad . \quad (4.11)$$

Using the weighting filters, boundaries for the closed-loop transfer functions are defined. Algorithms solving this problem will be discussed in Sec. 4.2.3. However appropriate filters must be designed first, which is discussed in the following section.

Design of weighting filters

Determining appropriate weighting filters that define the optimal controller demands a reliable model and a-priori knowledge of the closed-loop requirements. During the measurements it turned out that the application of a second-order filter gives the possibility to test especially influences of corner frequency and gains within the filters. Keeping the weights simple reduces the number of tunable parameters to a small number, which is practical for implementation. Nevertheless for future projects and with the more advanced system model this filters will probably become more complex, especially in the frequency range where resonant modes are assumed. Currently these modes are effectively suppressed by the roll-off at higher frequencies of -40 dB/dec. The transfer function of the weighting filters are given as:

$$w_S(s) = \frac{1}{M_S} \frac{(s + \omega_{S1})(s + \omega_{S2})}{(s + \omega_{S3})(s + \omega_{S4})} \quad , \quad (4.12)$$

and

$$w_T(s) = \frac{1}{M_T} \frac{(s + \omega_{T1})(s + \omega_{T2})}{(s + \omega_{T3})(s + \omega_{T4})} \quad , \quad (4.13)$$

where usually the poles and zeros are chosen as $\omega_{S1} = \omega_{S2}$, etc. to have a steeper roll-off. An example plot is shown in Fig. 4.6, where also the corresponding $S(s)$ and $T(s)$ are computed for the closed-loop system.

For comparison with the proportional controller, the closed-loop sensitivity and complementary sensitivity are plotted (grey). Having this comparison it is possible to estimate the improvement due to the MIMO controller by inspecting the defined weighting filters. The shaping filter W_T influences the rejection of noise and step response overshoots, by limiting the roll-off frequency and maximum singular value of $T(s)$. Further the shaping filter W_S is used to determine the closed-loop bandwidth and to achieve steady-state accuracy. It is obvious that due to the dependencies of both transfer functions, arbitrary shapes cannot be achieved. There are certain limitations due to the fixed-order of the MIMO controller.

4.2.3 Fixed-order controller

The structure of the controller has already been discussed in Sec. 4.1.2. Due to hardware limitations in the FPGA, the controller terms are restricted to order two, which also limits the number

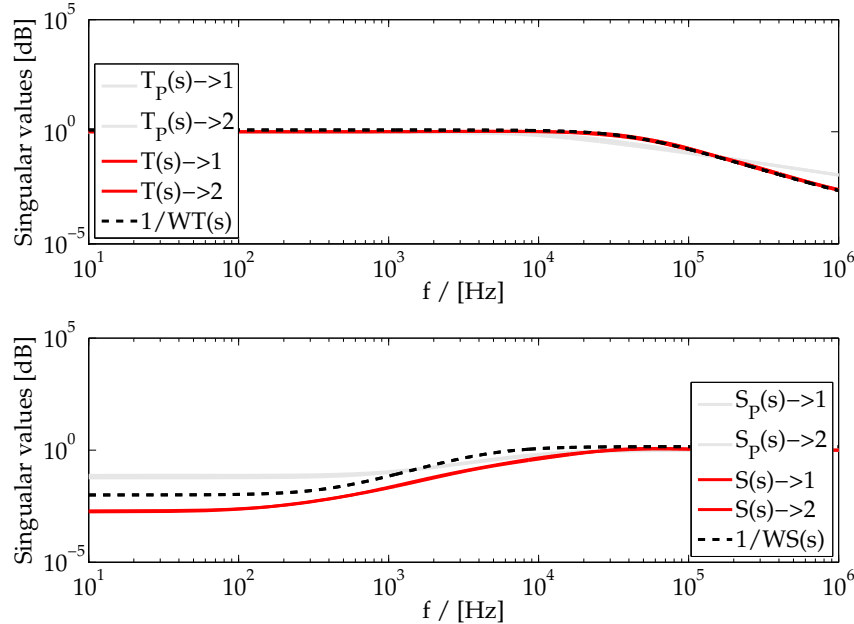


Figure 4.6: Singular value plots of the shaping filters and $S(s)$ and $T(s)$ of an example designed controller in comparison with the P controller.

of parameters to be determined. However there are no restrictions on the order of the plant model that is required for the mixed sensitivity design, which is typically chosen to be higher than that of the controller. This requires application of an algorithm that solves the problem of Eqn.4.11.

Usually in H_∞ controller design methods it is necessary to have the same order for the model and the controller. However the so-called HIFOO algorithm can solve fixed-order stabilization and local optimization problems based on techniques like quasi Newton updating and gradient sampling methods, [40]. In practical application this algorithm demands as input values the above-described generalized plant along with the defined weighting filters. The algorithm starts the searching method with 3 arbitrary sets of parameters, using a gradient-based search method to find the optimal set within the given constraints. Further details about the search procedure can be found in [41], [42]. Rather than using arbitrary starting values, the computation time can be decreased by starting with parameters from a previous design system model. The weighting factors in the controller design are chosen such that the H_∞ norm is fulfilled and the desired closed-loop performance is achieved.

It is practical to begin the design process with "weak" weighting filters such that a set of useful controller parameters can be easily found. Design constraints are subsequently tightened in order to achieve a higher closed-loop performance. For the permanent implementation of this design method for the real plant, a standard procedure should be defined in order to automate this. For example if the model has been changed over time or because of different machine settings, it might be necessary to update the controller parameters. In addition it is necessary to convert the computed continuous-time controllers to a set of discrete-time values before uploading them to the plant. For the realization of this design method, Matlab has been used, but for

permanent implementation it might be necessary to convert this to plant specific programming language. In the following the measurements are presented for the controller implementation on an example set of controllers.

4.3 Measurement Results

A large variety of the designed controllers have been tested on the real plant, but because of limited access to the plant, many tests had to be performed offline using data from previous runs. Furthermore interfaces and procedures have to be worked out in order to apply the design parameters to the real plant. It was necessary to gain experience for estimation of the applicability of the controllers, e.g. judging by simulations the performance or the correct settings of the weighting filters. A major improvement was the implementation of a copy of the control system (the so-called development system), installed in parallel to the real one. This system was used for controller development and for preparing future studies. A second benefit of the development system is that it can be used as an external independent observer to measure the controller performance. In addition, electron beam diagnostics provided another independent measurement of controller performance.

Before showing the actual measurements, difficulties associated with limited testing time and susceptibility to incorrect controller settings will be discussed and methods of evaluating controller performance will be introduced.

4.3.1 Controller application test

For a complex machine such as considered here, the conditions are limited by the physical bounds of the plant and the need to protect the plant from potentially serious damage or equipment down times. For example, an unstable controller might lead to high gradients in the cavities, yielding to quenches in the machine. In this case superconductivity tends to break down and the cryogenic system, raises an interlock for the whole machine until this subsystem recovers, which might take hours. To prevent these scenarios, it is necessary to find an appropriate way of testing the designed controllers. Closing of the feedback loop is done by smoothly increasing a proportional gain factor in order to detect possible instability. In the measurement results presented in Sec. 4.3.3, this gain sweep is further used for controller comparison.

Furthermore it was tested if the simulations can be used to optimize the weighting filters concerning the performance tests on the real plant, which has been discussed in detail in [37] and [44]. Concerning the idea of having a frequent controller update by changes in the system or large setpoint variations, it is necessary to develop a reliable procedure of the controller parameter estimation, based on the new model of the plant (see Sec. 6.2).

4.3.2 Performance definition

To characterize the controller performance, measurement criteria must be defined that distinguish between the two controller design objectives. The requirements defining the deviation of the measured RF field from the reference trajectory during the flat top. This is also described as the field stability as it was introduced in chapter 1. It is known that the measured vector sum

signal is corrupted by measurement noise contributions. So if only the rms value of the field error is taken, it is not fully representing the field error inside the cavity. Nevertheless large imperfections are penalized during the analysis by the rms error caused by instabilities or large field excursions. The relative rms amplitude variation $(\Delta A/A)_{rms}$ can be measured as:

$$\left\langle \frac{\Delta A}{A} \right\rangle_{rms} = \frac{1}{r_A} \sqrt{\frac{1}{N} \sum_{n=1}^N (y_A(n) - r_A(n))^2} , \quad (4.14)$$

and for the rms phase variation $(\Delta P)_{rms}$ as:

$$\langle \Delta P \rangle_{rms} = \sqrt{\frac{1}{N} \sum_{n=1}^N (y_P(n) - r_P(n))^2} . \quad (4.15)$$

Here $y_A(n)$ and $y_P(n)$ denotes the measured vector sum for the sampling instant n in amplitude and phase respectively. If only extracting the flat top region, the summation is given from 1 to the flat top length N . This has to be shifted about the filling time if the whole pulse length is considered. The reference trajectory is similarly defined, although it is assumed that the reference is constant during the flat top, with $r_a(n) = r_a$ as given in Eqn. 4.14. For normal operation it is often the case that the amplitude and phase measurement show slopes over the long flat top due to detuning effects. When the entire flat top is taken into account in the computations, the data must be detrended before computing the rms error. Usually it is possible with an optimal feedforward signal to keep the field almost flat during the pulse, as it will be discussed in chapter 5.

The second criterion is related to the long-term invariance of the vector sum. Often the machine is running in a single bunch mode, meaning that during a pulse only one bunch is accelerated. In these cases, the flatness of the RF field within a pulse is not relevant, but variations from pulse-to-pulse still must be minimized. Therefore, a method is needed to quantify the pulse-to-pulse variation. Equivalent to using rms as a measurement of stability during a pulse, the relative pulse-to-pulse amplitude variation $(\Delta A/A)_{p2p}$ can be measured as:

$$\left\langle \frac{\Delta A}{A} \right\rangle_{p2p} = \frac{1}{r_A} \sqrt{\frac{1}{M} \sum_{k=1}^M \left(\frac{1}{N} \sum_{n=1}^N (y_A(n,k) - r_A(n,k)) \right)^2} , \quad (4.16)$$

and for the pulse-to-pulse phase variation $(\Delta P)_{p2p}$ as:

$$\langle \Delta P \rangle_{p2p} = \sqrt{\frac{1}{M} \sum_{k=1}^M \left(\frac{1}{n} \sum_{t=1}^n (y_P(n,k) - r_P(n,k)) \right)^2} , \quad (4.17)$$

where $y_A(n,k)$ denotes the measured amplitude vector sum for the sampling instant n and the pulse k . The phase notation is defined similarly. In contrast to the rms variation defined previously, pulse-to-pulse variations are measured using only the mean value of the vector-sum in order to reduce the high-frequency contributions to the field error during the flat top.

In the following, three example controllers are presented to give an overview of the performance improvement using a MIMO controller instead of the proportional feedback controller.

4.3.3 Controller comparison example

Rather than presenting results from the large variety of controllers tested, three examples have been chosen to demonstrate the performance improvements achieved using the complex higher-order controller. To allow a comparison, the model used for estimation of the controller parameters has been retained. The variance of the controllers is given by the weighting filters used in the design process. As an example four different controllers are compared, which are the usual proportional feedback plus three designed controllers differing due to different bandwidth used in the shaping filters of Eqn. 4.12, where $2\pi f_s = w_{s1} = w_{s2}$. Typically, a gain sweep was performed in order to determine the optimal controller setting, meaning that the proportional gain is incrementally increased and the field error measured. For comparison with the estimated MIMO controllers presented now, the gain factors were initially scaled down and subsequently increased to the designed proportional gain factor. Furthermore it has to be mentioned that although I and Q are the controlled field components, for the determination of the field regulation quality, the amplitude and phase are taken and therefore also presented in Fig. 4.7.

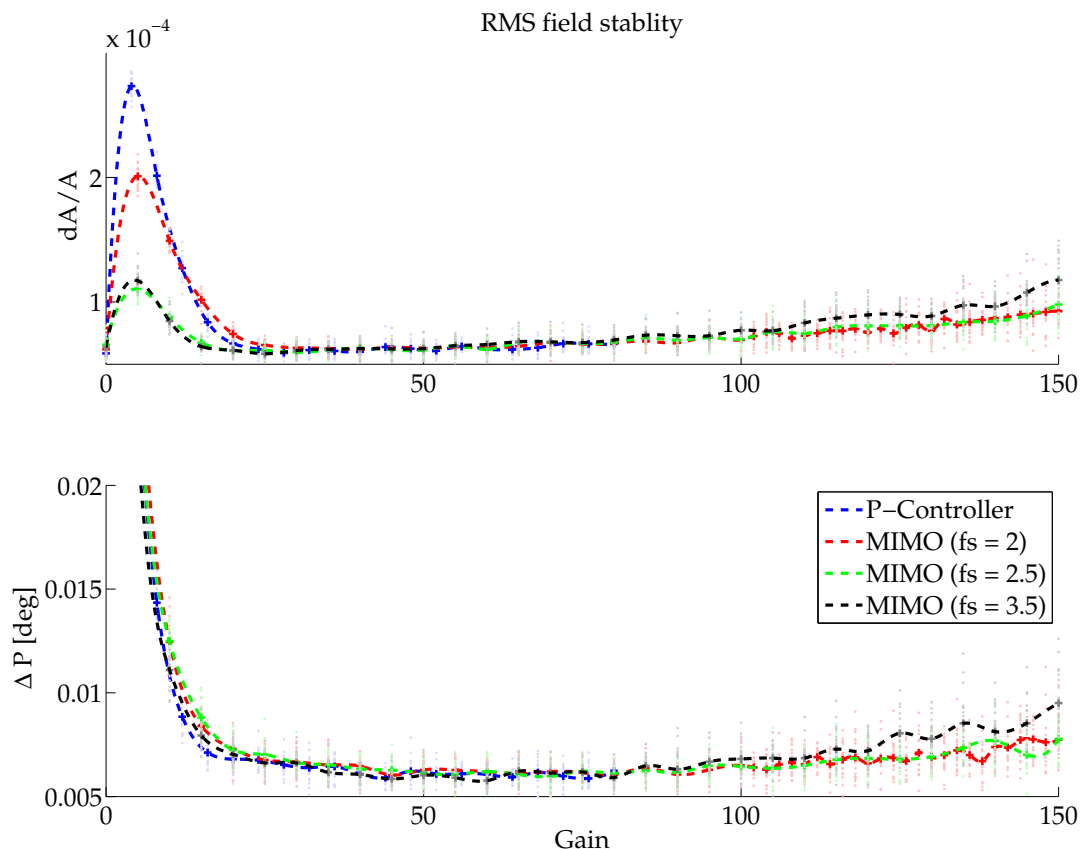


Figure 4.7: Comparison of the rms stability during the flat top for three different MIMO controllers and the proportional feedback as function of the feedback gain.

It can be clearly seen that the rms field stability for amplitude and phase does not significantly differ for all controllers. The minimum achievable value is determined by the residual influences

from the measurement noise. The single dots denote individual measurements, while the lines represent the mean over 20 pulses.

When the proportional gain is increased, the closed-loop bandwidth also increases, leading to growing field excursions as can be seen from Fig. 4.7. These field excursions are caused by the feedback of measurement noise in the system. Further, the $\frac{8}{9}\pi$ -mode leads to growing oscillations (see Fig. 3.15), until the closed-loop system gets unstable. To this point, the designed MIMO controllers do not show significant improvements in the rms error since high-frequency measurement noise dominates the field error signal.

The second controller task was to reduce the pulse-to-pulse fluctuations of the measured RF field. Measurement results of the pulse-to-pulse fluctuations are shown in Fig. 4.8 for the same controllers as in Fig. 4.7.

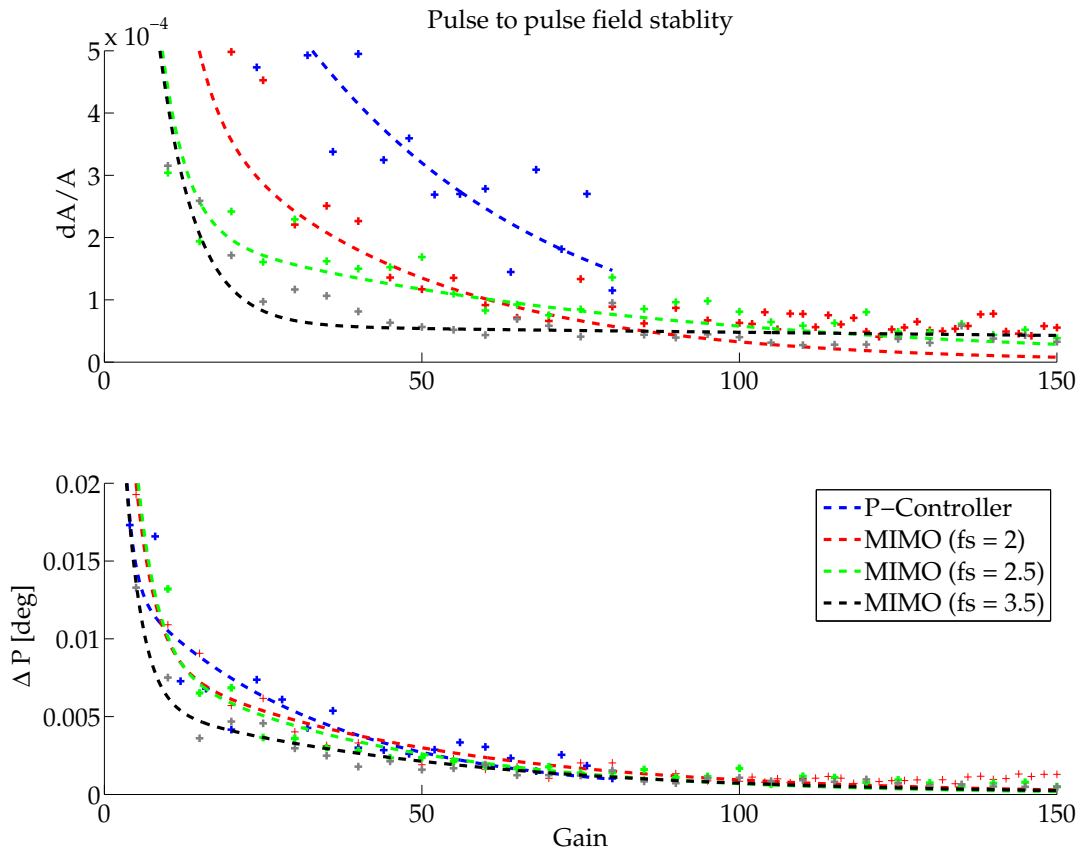


Figure 4.8: Comparison of the pulse-to-pulse stability of the mean flat-top for three different MIMO controllers and the proportional feedback as function of the feedback gain.

By contrast with the rms field stability, the pulse-to-pulse stability shows significant differences for the compared controllers. The gain sweeping range for the proportional controller is smaller than for the MIMO controllers. During the measurements, higher gains have not been tested because the vector sum started to build up oscillations and tended to get unstable. It is easy to observe that the MIMO controller with the shaping filter corner frequency $f_s = 3.5$ kHz gives

the smallest relative amplitude error for small gains, whereas the proportional controller has the worst amplitude stability. For the phase, the errors are less significant but show the same behavior. In this case the improvements due to the higher-order controllers compared to the proportional feedback controller are easily visible. Further it can be seen that increasing f_s also enhances the performance especially for lower gains. As a consequence of the measured rms stability given in Fig. 4.7 the last (black) estimated controller is used with a proportional gain factor at about 40 – 50 (half the gain as estimated by the design procedure).

Other measurements have been performed in addition to the measurements shown for these three example controllers. A digest of measurements can be found in [37], [43] and [44]. The conclusion is that the best improvements in pulse-to-pulse fluctuations come from the higher-order controllers with higher low-frequency gain. Theoretically it would be possible to achieve these reductions with the proportional controller as well, but the growing rms field error is not acceptable. The steep roll off at the closed-loop bandwidth allows to achieve the noise suppression in combination with the high low-frequency gain.

Verification with electron beam

The performance of the RF field regulation is measurable by studying the electron beam deflection in the bunch compression section (corresponding to beam energy), and hence it provides an independent measure of RF field regulation in the up-stream accelerator module that was being controlled by the MIMO controllers. For more details about the equipment and technique, the reader is referred to [45], [46]. In Fig. 4.9 the results are shown as relative beam energy stability vs relative pulse-to-pulse amplitude stability of the measured vector sum. In a similar way to the field measurements presented in Sec. 4.3.3 a comparison between three designed controllers and the proportional feedback controller is shown.

It can be seen that the controller with the lowest amplitude error does not have the best beam stability measurement. This might be due to the discrepancy between the measured vector sum and the beam energy and the limited accuracy in the measurements. To investigate this assumption, additional measurements would be required, but these have unfortunately not been possible so far. Nevertheless, Fig. 4.9 shows that the designed controllers improve the beam energy stability as well as the field amplitude stability. The controller *C3* has a mean $\Delta E/E \approx 1.3 \cdot 10^{-4}$ at $\Delta A/A \approx 4.4 \cdot 10^{-5}$, which is below the requirements defined in chapter 1.

Nevertheless the improvements to the beam stability are not immense compared to the proportional controller as it might be expected. But with the model improvements introduced in Sec. 3.4 it might be possible to enhance the controller as well. It turned out that the high-frequency noise contributions are the main disturbance source to be suppressed by the controller. This conclusion raises the question if a conservative lowpass filter in the feedback loop would also fulfill the same requirements as the complex designed controllers. Tests have been made, showing that with filtering only the achieved performance is not comparable with the designed controllers. So far the presented data are derived from the the *ACCI* system as the main examined plant. In the next section, a brief account of the design applied to a different system will be discussed.

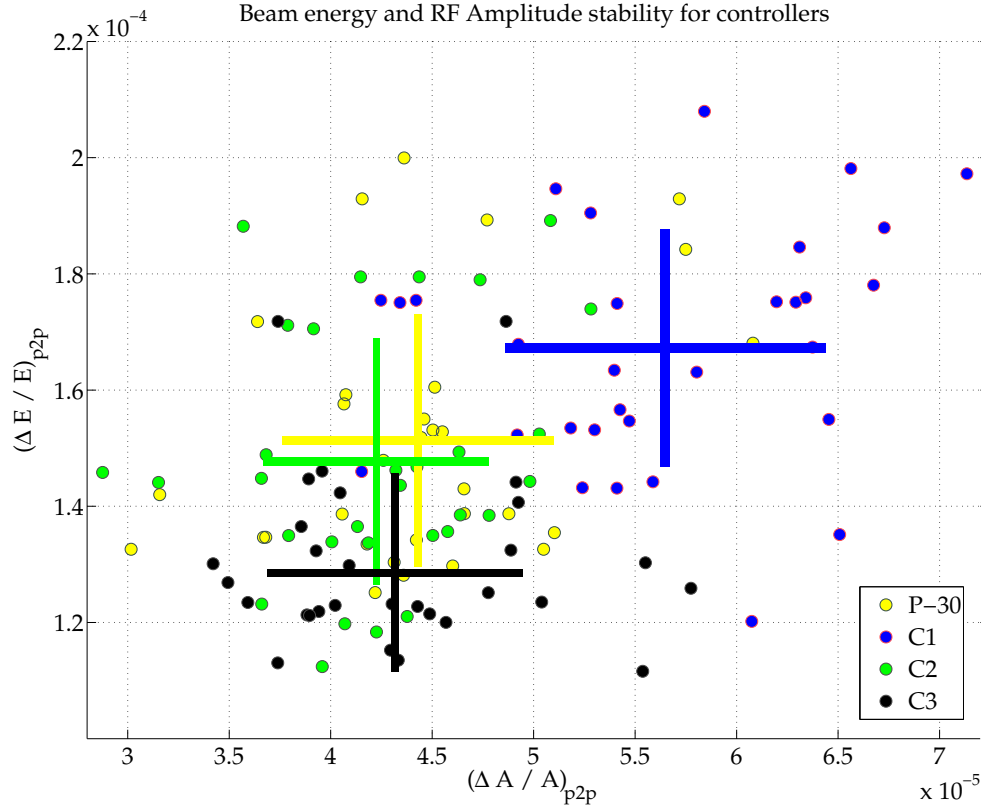


Figure 4.9: Relative beam stability as function of the measured relative vector sum amplitude error. The points give the actual measurement whereas the crosses give the standard deviation of the points for beam and amplitude stability

4.3.4 Measurements from the 3.9 GHz module

At the time of writing, a new “third harmonic” 3.9 GHz accelerating cavity is being installed at FLASH immediately downstream of the ACC1 accelerating cavities in order to linearize the longitudinal phase space of the electron beam. With the appropriate relative phase and amplitude settings the performance of the FEL is improved. For details the reader is referred to [47] and [48]. From the perspective of controller design, there are some differences in the third-harmonic system compared with the other modules, for example, some changes are necessary to the cavity field probe signal chain because of the higher RF frequency. The main difference, however, is the system dynamics because the cavities have a higher bandwidth due to the lower $Q_L \approx 1.3 \cdot 10^6$. Nevertheless, the same process is used to design the model based controller, albeit with different input parameters, meaning that the system model was estimated according to the steps presented in Sec. 3.2 and the controller design according to Sec. 4.2. Analogous to the estimated controllers in the previous section the measurements were done as a comparison to the designated proportional controller. Unlike previous measurements, however, tests on the third-harmonic cavities were performed in a high power RF test stand without beam (still sufficient to measure RF regulation quality). The conditions for measuring the field stability were kept unchanged, i.e. measurements of RF flat top and pulse-to-pulse stability used the same

formulae given in Fig. 4.10 and Fig. 4.11.

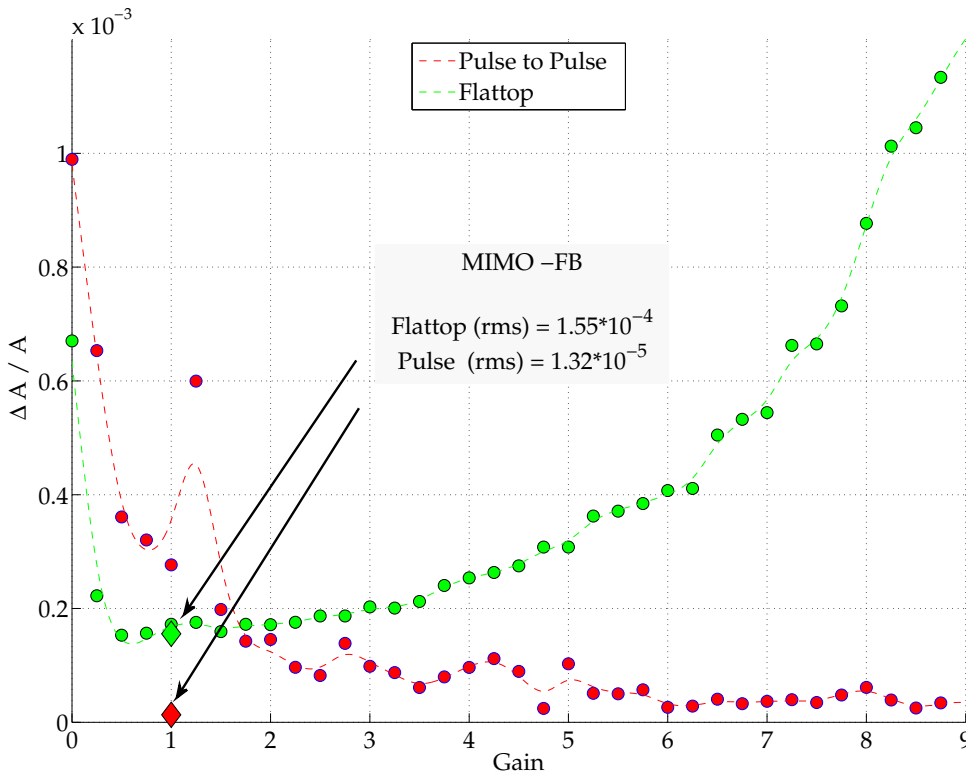


Figure 4.10: Comparison of the relative amplitude errors between the MIMO Controller and a gain sweep with the proportional feedback controller. It can be observed that the proportional feedback gains a better pulse-to-pulse stability with increasing the gain (marked as dots). This unfortunately also increases the measured RMS error during flat top. The MIMO controller (marked as triangles) which has only one optimal gain, fulfills the pulse-to-pulse requirements without increasing the rms error during flat top.

Sweeping the feedback gain of the proportional controller showed that the gain is limited by the predicted $\frac{8}{9}\pi$ -mode and the system is more sensitive at higher gains due to the wider cavity bandwidth. The influence can be clearly seen by the flat top stability in the amplitude of Fig. 4.10, where for high gains the rms error grows to unacceptable levels and beyond the levels measured during open-loop operation. By way of comparison, the best performance achieved using the MIMO-Controller is given as the points at gain 1. The actual values are given within the figures for direct comparison. Here the improvement due to the MIMO controller is more significant than in the case of the 1.3 GHz system. The smallest flat top error with the proportional controller is achieved using a feedback gain between 0.5 – 2, but for this setting the pulse-to-pulse stability is worse than with higher gains. In contrast, the MIMO controller combines the two objectives in the best condition regarding to the field stability in amplitude and phase. The improvements using the complex MIMO controller are mainly the result of higher

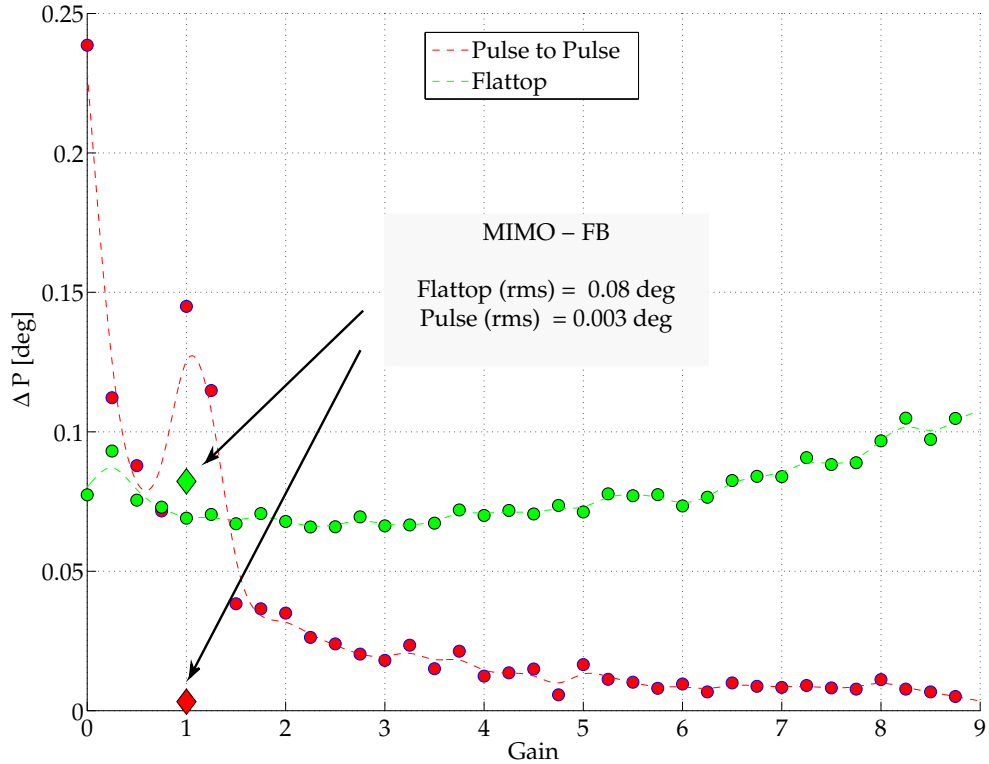


Figure 4.11: Comparison of the phase errors between the MIMO Controller and a gain sweep with the proportional feedback controller. It can be observed that the proportional feedback gains a better pulse-to-pulse stability with increasing the gain. This unfortunately also increases the measured rms error during flat top. The MIMO controller (marked as triangles) which has only one optimal gain, fulfills the pulse-to-pulse requirements without increasing the RMS error during flat top

gain in the low-frequency range and the lowpass characteristic of the controller, which filters high-frequency noise and especially the frequency contributions from exciting other modes of the system. Frequency spectra of the controller I and Q outputs are shown in Fig. 4.12, which confirm that high-frequency noise is amplified by the controller for higher gains. The bode diagram of the presented controller is given in the appendix Fig. A.7 and detrimental effects from aliasing are discussed in detail in Sec. 3.3.5.

It is evident from the figure that the main differences between the two controllers are in the frequency range above 40 kHz where the higher-order MIMO controller suppresses the signal but the proportional controller adds peaks at about 50 kHz. This effect was also visible for the 1.3 GHz system, but the disturbance suppression is more distinctive in the 3.9 GHz case because of the higher bandwidth.

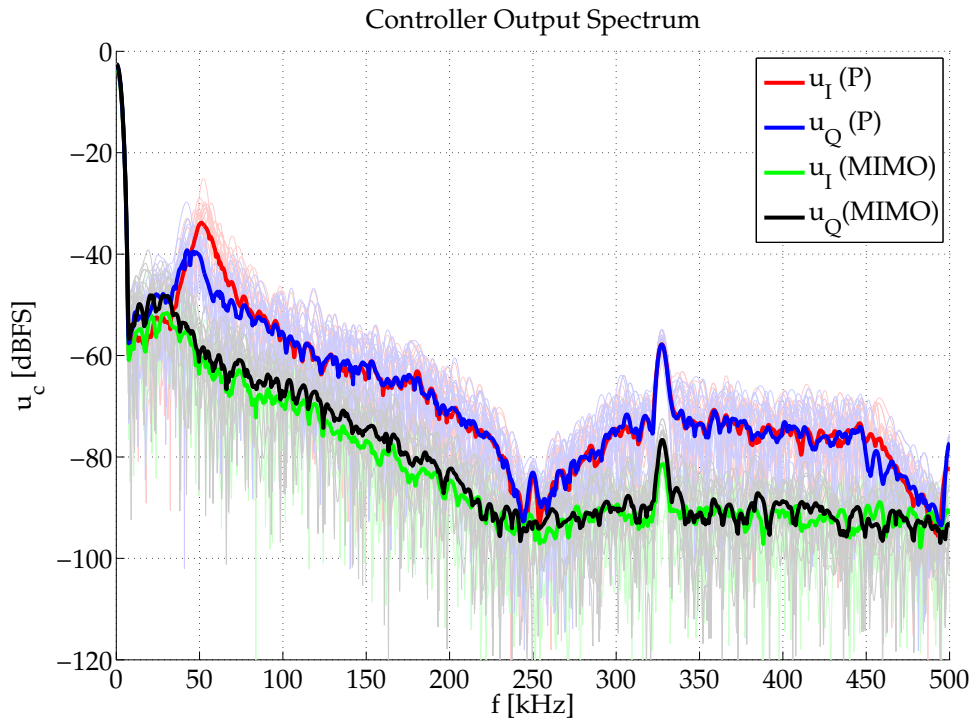


Figure 4.12: Comparison of the spectral components of the controller output between the MIMO and P-Controller at the gain with highest pulse-to-pulse stability (compare with Fig. 4.10). Due to the bandwidth limitation in the MIMO, is the output at frequencies above 40 kHz suppressed compared to the output of the P-Controller

4.4 Conclusion and suggestions

Experience from the feedback controller design can be summarized through the following statements.

1. A model based feedback controller design was tested successfully for two different kinds of RF feedback systems on a real plant.
2. The second-order MIMO controller improves the field regulation of the ACCI system to an amplitude stability of $\approx 5 \cdot 10^{-5}$ and a phase stability of $\approx 0.003^\circ$ for pulse-to-pulse fluctuations. The flat top rms stability does not show significant improvements.
3. The best achieved pulse-to-pulse beam energy stability with the designed controller was measured at $\approx 1.3 \cdot 10^{-4}$
4. For the 3.9 GHz system, the improvement in RF field regulation is in the order of 10 over the proportional feedback controller!

Such results could be achieved even with the simple lowpass system model and a corresponding simple weighting filters, and it is anticipated that further improvements in regulation would be achieved by using a more complex plant model and a higher-order controller.

The main conclusions to be drawn from the designed controllers is that the primary source of instability is excitation of system modes other than the fundamental from high-frequency noise injected into the system by the controller, which means that increasing the proportional controller gain to achieve stable pulse-to-pulse conditions has a negative impact on the flat top rms error by inducing oscillations. In addition, the digitalization process and corresponding aliasing effects lead to oscillations of the $\frac{8}{9}\pi$ -mode whose influence on the driving signal cannot be neglected. Discrepancies between the measured vector sum and the vector sum seen by the beam and their influence on the RF feedback system are not yet fully understood since measurements of the electron beam energy show that perfect RF field regulation does not necessary lead to a perfect beam energy stability. Rather it could be observed that, for long-term measurements, the detected and regulated vector sum can be kept stable, but the observer system detects drifts which are correlated with the beam energy measurements and with changes in humidity and temperature. Clearly reference tracking cannot be guaranteed even with a good controller when feedback signals are measured inaccurately. Drift compensation applications are currently under development. To overcome this drawback it is essential to incorporate beam energy measurements into the feedback controller. Currently this is achieved using an energy control loop on top of the RF field control. In this implementation it cannot be guaranteed that both control applications do not influence each other which might cause instabilities, but a combined controller concept has to be developed such that the MIMO controller is extended in order to incorporate beam information as well as the RF feedback. Further considerations on this can be found in chapter 6.

In the next chapter, we will discuss suppression of predictable pulse-to-pulse disturbances using a sophisticated pre-compensation on the feed-forward drive. Also discussed is the combination of this feedforward compensation with the feedback controller concept, which efficiently achieves the required regulation performance.

Chapter 5

Iterative learning control

The low bandwidth of the feedback loop and limitations on the gain of the feedback controller lead to residual field errors that are not suppressible in closed-loop operation. Open-loop control, also known as feedforward, is used to bring the system closer to the reference trajectory, thereby reducing the error for the feedback controller. In the present implementation, the feedforward drive remains unchanged from pulse-to-pulse unless the machine operators apply changes to the configuration. This lack of automation raises the question of whether or not the feedforward can be better optimized with automated control to further decrease the remaining control error. Since repetitive disturbances are predictable, they can be suppressed by automatic tuning of the feedforward drive.

Iterative learning control algorithms provide the necessary control theories to realize automatic feedforward tuning. The principles of learning control algorithms were originally developed to control processes akin to robots fulfilling circular pick and place tasks. Applications can be found in [49], [50] and [51]. The routines are derived from repetitive operational procedures where an unchanged reference trajectory is cycled for long time. Predictable disturbance sources arise from the physical properties like inertia which lead to control errors or slowing down the operation speed. These influences can be suppressed by learning from previous errors and using that information to optimize the control signals, [52].

The task for RF field regulation is analogous to the example of the robots. In the case of RF control, the predefined setpoint trajectory has to be followed without deviation. Repetitive disturbances as well as non-optimal initial feedforward settings cause deviations from the setpoint trajectory and need to be minimized. Therefore, the ideas of this learning algorithm is transferred to this system and implemented to improve the RF field regulation.

This chapter is organized as follows. First, general properties of the iterative learning control algorithms are introduced in Sec. 5.1. Disturbances which are expected to be suppressed are summarized and some considerations about the implementation on the systems are mentioned. Subsequently, the measurement results are presented in Sec. 5.2. This encompasses both open-loop and closed-loop measurements with the proportional feedback controller. Afterwards, the combination of the MIMO feedback controller and the ILC is given in Sec. 5.3. Regulation performance for the RF field and the electron beam energy, as well as the long-term convergence is discussed. Finally, the main results are summarized and considerations regarding the implementation for regular machine operation are presented in Sec. 5.4.

5.1 General properties

Iterative learning controllers (ILC) are used to control repetitive processes consisting of a number of trials, each representing the same procedure. Since the cavities to be controlled are operated in pulsed mode, meaning that every specific time instance the same RF pulse is generated, the accelerating process is considered to be repetitive. Moreover, some of the disturbances appearing during this operation are repetitive as well, and can be predicted for upcoming pulses as long as the operation conditions remain unchanged. Therefore, the application of the ILC technique is considered to be feasible for the RF field control. In the following the general idea of an ILC is presented.

5.1.1 Repetitive disturbance

An overview of the disturbance sources, including the main contributions of repetitive disturbances have been introduced in Sec. 2.2. These unavoidable disturbances are caused by the properties of the plant, or due to the relation to the acceleration process like beam-loading effects. Additionally, there exists further contributions to the resulting field error. Several are not fully compensated, or they are actually introduced by the feedback controller, e.g. transition overshoots due to closed-loop operation of the system. To summarize, the main sources of repetitive field errors to be compensated by the iterative learning controller are as follows:

- Beam-loading effects during the flat top, including the beam turn-on transient, that can not be compensated by the feedback controller due to the low bandwidth even in closed-loop operation
- Lorentz force detuning, introducing slope on field phase and amplitude if not compensated by active mechanical suppression (main open-loop control error contribution)
- Overshoot in phase during the transition from filling to flat top phase caused by the feedback controller and klystron phase jumps, due to switching the power to 1/4 from filling to flat top
- Non-optimal feedforward configuration, especially in the flat top phase to keep the control error small to the feedback controller

The first two items have been discussed in detail in previous sections, while the latter disturbances are described here. The typical feedforward signal has a significant step transition from the filling to the flat top phase. This feedforward trajectory was derived from the desired cavity fill time and beam-loading compensation assumptions made when designing this machine, [9]. From control point of view, step transitions have strong impact on the system due to their broadband excitation. Furthermore, additional drawbacks arise in this application largely because of the klystron. The power ratio between filling and flat top in open-loop operation is $P_{filling} \approx 4 \cdot P_{flatop}$, and this step change in power causes changes in phase at the klystron output. Both control channels are affected by this phase change due to the IQ control scheme. The ILC should also compensate for deviations from the reference field trajectory during cavity filling. For example applying a pre-detuning to the cavity, in order to keep effects of LFD small

during the flat top has an impact on the cavity fill time, and hence change the trajectory during the fill time. The impact of LFD on field errors are particularly evident at the end of the flat top where detuning effects are strongest, which is easy to observe in Sec. 5.2.1.

Beam-loading effects contribute largest to field errors and are the most important disturbance effect to be compensated. When the machine operates with several bunches in a single pulse, it is generally the requirement that all bunches have the same acceleration voltage, leading to the same energy gain for all bunches in the train. By extracting energy while passing through the cavity, bunches introduce field errors that would cause subsequent bunches to have a smaller acceleration gradient. This effect continues over the entire bunch train, which results in strong differences of the accelerating voltage from the first to the last bunch within this train, as illustrated in Fig. 2.13. The induced field error depends on the bunch repetition frequency and the charge of the electrons. Especially for high charges and high repetition frequency, compensation of this beam-loading effects is necessary for machine operation. In Sec. 5.2.2 and Sec. 5.3 compensation of this effect using the ILC is presented.

5.1.2 Overview of iterative learning techniques

Various concepts for iterative learning control algorithms concerning the application to be used can be found in the literature, e.g. a nice overview can be found in [53]. The idea is to take information from previous trials to optimize the control inputs on the next trial. Clearly, only repetitive disturbances can be suppressed through this learning process. In the general form, a P-type iterative learning control algorithm can be written as, [54]:

$$u_{k+1}(t) = Q(u_k(t) + L e_k(t)) \quad , \quad (5.1)$$

where Q and L are filter matrices of accordant dimensions. The trial number is given by k , whereas the sampling instant within a pulse is denoted by t . In this work only a P-type algorithm is considered, although extension to a so-called D-type algorithms would be possible. Higher-order algorithms consider additional previous trials as well as the most recent, [55]. Analog to the feedback controller, the ILC can be seen as a pulse-to-pulse feedback, calculating and updating the feedforward signal before the next pulse starts. To address more complex system dynamics, model based algorithms can be found, which in simple cases generate an inverse of the system model $L = G^{-1}$, where G denotes the plant, [56]. This requires exact knowledge of system dynamics, something that is not generally the case for real applications. Ideally the errors will become progressively smaller from pulse-to-pulse so the feedforward changes will approach zero, which means that the algorithm converges towards the optimal input signal. A convergence criterion based on the norm of the control error is given as:

$$\|e_k\| \rightarrow 0 \text{ as } k \rightarrow \infty, k \in \mathbb{N} \quad , \quad (5.2)$$

with $\|e_k\|$ the l_2 -norm of the control error e for the k -th trial. The procedure to determine the filter coefficients Q and L is the task for the algorithms. Several approaches can be found in the literature, for example, [57] and [58]. Further a large variety of studies to application of different kinds of algorithms can be found [59], [61] and [60]. In the following section, an algorithm is proposed that is based on minimizing a quadratic cost function, see [64].

5.1.3 Norm optimal iterative learning control

In this section, the basic derivative steps are outlined for the proposed iterative learning controller. Further details can be found in [64]. This model-based algorithm has been chosen because it can achieve fast convergence with small computation effort between two subsequent trials. Furthermore there is already a proposal for a fast version of the algorithm in [62], which minimizes the computation effort between two trials by computing the necessary matrices before the iteration starts. The algorithm provides current trial feedback mechanisms combined with feedforward of previous trial data by splitting the two dimensional dynamics into two separate one dimensional dynamics, [64]. It is possible to realize this approach by separating disturbance suppression between the feedback and feedforward controllers in the frequency domain. The allocation of controller actions is discussed later when introducing the update law. Furthermore, since this algorithm is based on the system model, it is consistent with the model-based design approach that has already been applied to the feedback design. The identified state space model of the plant was introduced in Sec. 3.1.1, and is given by three discrete time state space matrices A, B, C . The control signals remain as they were described in the previous chapter, and the basic ILC requirement is defined as:

$$\lim_{k \rightarrow \infty} y_k(t) = r(t), \quad \lim_{k \rightarrow \infty} u_k(t) = u_\infty(t) \quad , \quad (5.3)$$

where y_k and r is the measured system output at the trial k and the desired reference trajectory respectively, u_k is defined as the system input and u_∞ is the learned control input. All discrete time signals are given as a function of the sampling interval t with $t \in [0, N]$ (here $N = 2048$) sampling steps within a pulse. In order to be able to compute an optimal input signal, a criterion has to be determined which defines the goal of the control task and allocates the quality of the input. This is done by minimizing the following minimum-norm optimization problem:

$$u_{k+1} = \arg \min_{u_{k+1}} \{J_{k+1}(u_{k+1}) : e_{k+1} = r - y_{k+1}\} \quad , \quad (5.4)$$

with the performance index

$$J_{k+1}(u_{k+1}) = \frac{1}{2} \sum_{t=0}^M e_{k+1}^T(t) W_1(t) e_{k+1}(t) + [u_{k+1}(t) - u_k(t)]^T W_2(t) [u_{k+1}(t) - u_k(t)] \quad , \quad (5.5)$$

where $e_k = (e_I \ e_Q)^T$ denotes the tracking error vector signal of the desired trajectory of the k th trial, for the I and Q channel.

The quantities $W_1(t)$ and $W_2(t)$ define weighting matrices of appropriate dimensions with $W_1(t) \geq 0$ and $W_2(t) > 0$ for all t . By selecting the matrices $W_1(t)$ and $W_2(t)$, the $(k+1)$ th trial control input is determined which reduces the tracking error e in an optimal way, while keeping the deviation from the control input used in k th trial small. The full derivation of the update equations given in Tab.5.1 can be found in [64]. The basic idea is to convert a non-causal representation by transforming the costate system used for the update equation into a causal system that can be solved as introduced in [64]. In order to derive the update matrices given in Tab.5.1 the well known discrete time Riccati equation has to be solved.

First level (before operation):

$$K(t) = A^T K(t+1)A + C^T W_1(t+1)C \\ - [A^T K(t+1)B \cdot \{B^T K(t+1)B + W_2(t+1)\}^{-1} \\ \cdot B^T K(t+1)A] \quad ; \quad K(N) = 0$$

$$\alpha(t) = \{I + K(t)BW_2^{-1}(t)B^T\}^{-1}$$

$$\beta(t) = \alpha(t)A^T$$

$$\gamma(t) = \alpha(t)C^T W_1(t+1)$$

$$\omega(t) = W_2^{-1}(t)B^T$$

$$\lambda(t) = (B^T K(t)B + W_2(t))^{-1} B^T K(t)A$$

Second level (between trials):

$$\xi_{k+1}(t) = \beta(t)\xi_{k+1}(t+1) + \gamma(t)e_k(t+1) \quad ; \quad \xi_{k+1}(N) = 0$$

Third level (between each sample interval):

$$u_{k+1}(t) = u_k(t) - \lambda(t)\{x_{k+1}(t) - x_k(t)\} + \omega(t)\xi_{k+1}(t)$$

Table 5.1: Summary of the control law used for the ILC, [66]

Both The Riccati gain $K(t)$ and the the predictive update component $\xi_{k+1}(t)$ are computed by the backward computation, having instead of an initial, a final value as $K(N) = 0$ and $\xi_{k+1}(t) = 0$, with N giving the final sampling instant. The solution has a major drawback for practical implementation due to the large amount of computational effort which has to be performed between two trials. Therefore in [62] the so-called *Fast-Norm-Optimal Iterative Learning Controller* (F-NOILC) was introduced which minimizes the computation effort between two trials by offline calculations before the iterations have started. The update equations are given in Tab. 5.1, where they are grouped in Levels according to where in the cycle the computations must be performed. Figure 5.1 shows a sketch of the level definitions, as applied to the pulsed operation in this application.

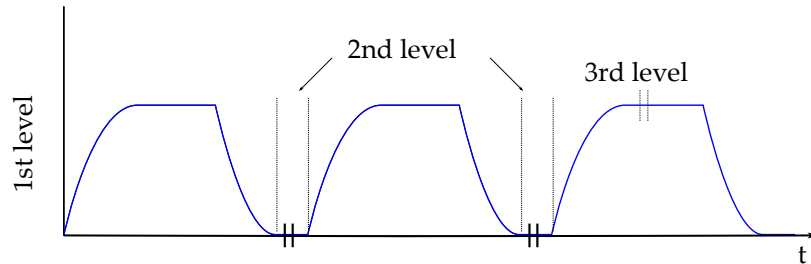


Figure 5.1: Sketch of the level notation given in Tab. 5.1

The algorithm is divided into three levels, where the first level consists of computations that

can be done before the adaptation starts, such as calculation of various matrices that remain unchanged. In the second level are those components that are computed between two trials, such as the calculation of the predictive component. The input signals with a state feedback component are computed during the third level, which corresponds to the time available for computations between each sample of a trial. The algorithm as it is presented in Tab. 5.1 can not be implemented on this plant, since the full state knowledge as it is presumed here cannot be provided. This and other practical limitations are discussed in the following.

5.1.4 Limitations for the real plant application

The algorithm introduced could not be realized without changing the existing fixed controller structure that is implemented in an FPGA. This algorithm also assumes full state knowledge, but it is claimed that this state feedback scheme can be replaced by an output feedback scheme, specifically the MIMO feedback controller that was introduced in the previous chapter [64]. Observer-based methods might be suitable for future applications, but they are not considered here.

For the first simulations and tests, the states were estimated offline using model based simulations which turned out to be impractical for this application, [28]. It has been studied that the measurements made on the plant showed best results when the state difference remained small and therefore have been neglectful for the algorithm. It was decided to implement the ILC on the plant without state feedback, meaning that the matrix $\lambda = 0$. This is rather a heuristic fix, which turned out to be practical in the real application. Optimality proofs for the original algorithm do not apply in this case. Nevertheless the application has been successfully tested and for later examination either state estimation by observer-based methods or other ILC techniques have to be tested, [29].

Substituting the state feedback for output feedback means that the third level computations of Tab. 5.1 can be moved to the second level, and the computation can be performed from pulse-to-pulse, while intra-pulse feedback is done by the MIMO feedback controller. Consequently, the update equation reduces to:

$$u_{k+1}(t) = u_k(t) + \omega(t) \xi_{k+1}(t+1) \quad , \quad (5.6)$$

with the predictive component ξ_{k+1} and $\omega(t)$ computed as defined in Tab. 5.1. Therefore, ξ has to be evaluated first due to the fact that this is a non-causal computation with a terminal condition $\xi(N) = 0$. The update law requires only matrix multiplications, which is feasible for real time applications and implementation, [63]. In order to combine the ILC algorithm with feedback controller, the update equations must be computed from the closed-loop system model rather than the open-loop plant model. The time scale is different for the two controllers, because one is active when the other controller remains unchanged: the ILC acts on the feedforward input to the system between pulses and the feedback controller acts intra-pulse. The end-boundary condition for the ILC forces the last sample of the feedforward control to remain unchanged. From the overall system perspective, the field need only be controlled during the flat top phase, and since the decay phase need not be controlled, the feedforward input and the feedback are both turned off. As a result, it is sufficient to compute the update corrections for just the flat top and filling time $N = t_{filling} + t_{flattop} - t_{start}$, where t_{start} is taken as starting offset at the beginning of the filling phase. This starting offset is needed for practical reasons,

because the control error is large at the begin of the filling phase and it must not be compensated either by the feedforward or feedback controllers. A typical starting time for the ILC has been chosen to be $t_{start} = 250 \mu s$ after the pulse starts, which is half of the filling time. The required computation steps are listed below.

1. Computation of the matrices β , γ , ω depending on the state space system matrices, weighting matrices W_1 and W_2 and the time span defined for the update.
(\Rightarrow this procedure has to be done once when initializing or restarting the update)
2. The control error $e_k(t)$ saved in the FPGA after the pulse, has to be readout by the control system. The previous feedforward input $u_k(t)$ is stored inside the memory.
3. Once the data is available, the predictive component $\xi_{k+1}(t)$ is computed using the control error e_k .
4. The new control input $u_{k+1}(t)$ is computed from the old feedforward input $u_k(t)$ and $\xi_{k+1}(t)$.
5. The new controller input has to be uploaded to the FPGA before the next pulse starts. The system will be operated with the new feedforward signal and items 2 – 5 are repeated.

Normally, one would expect that the feedforward tables are updated on consecutive pulses. However, the present controller structure inside the FPGA is not able to do the calculations. They have to be computed on a server that provides all tables to be processed inside the FPGA. These tables are written in registers and transferred through the communication interfaces. There is a fixed and limited time available for communication and processing since the controller must operate at a fixed pulse repetition frequency (5Hz presently). If the update is not computed fast enough, old tables will be written and the update process will get out of step. The choice of algorithm, processor performance, and speed of communication are all important considerations if pulse-to-pulse adaption is required. To determine the convergence speed of the algorithm, the iteration steps instead of pulses have been taken. This allows to be independent of transmission time variations from one step to the next. Additional considerations for the future permanent implementation are given in Sec. 5.3.4. First the measurement results are presented in the following section.

5.2 Experimental results

The measurements are taken from the same plant as it was introduced in the previous chapters. Usually the ILC would update the original feedforward tables every adaptation step. However, by directly overwriting this tables, the influences to machine operation are significant, e.g. in case of malfunctions the original tables are incompletely overwritten. Furthermore, by phase or amplitude changes the original tables are set back leading to wrong adaptations. Introducing additional correction tables that will be added to the original feedforward tables overcomes this drawback. Therefore the algorithm is started always with initial zero vector $u_0(t) = 0$, whereas the usual feedforward is left. In the following, the correction input is denoted as u_{corr} . The error data are readable after the pulse through the control system. All processing steps are done

in Matlab. Due to the fact that the tests have been made not necessarily from pulse-to-pulse, also several data sets could be taken to average the control error, keeping the high-frequency noise small. The convergence speed is thereby described in the following by the number of iteration steps. Next the ILC algorithm is presented as an open-loop adaptation and in addition in closed-loop, which is more feasible for the usual operation, [43]. Closed-loop in this case means the combination of the ILC with the proportional feedback. The combination with the MIMO controller is presented afterwards in Sec. 5.3. The weighting matrices W_1 and W_2 have been chosen in a way that the adaptation is fast enough without getting unstable. The possible time dependency of W_1 and W_2 as given by Tab. 5.1 has been tested, but for the following presented results they are chosen as:

$$W_1 = q \times I, \quad W_2 = I, \quad (5.7)$$

with q giving a scalar weighting factor. This scalar factor is intended to provide machine operators a "tuning knob", as it is discussed in Sec. 5.3.4. For the results presented in the following a practicable setting has been found with $q = 100$.

5.2.1 Open-loop adaptation

For the first tests on the plant, adaptations in open-loop were done to check that the algorithm is valid and that it gives results comparable to simulations, which have been shown to converge even with adaptation of the beam-loading effects, [28]. Compensation of beam-loading was not tested in open-loop operation due to operational limitations of the plant. Without the feedback controller the risk of so-called beam losses is high and therefore the electron beam with less charge and number of bunches can be turned on for short time only.

The main source of repetitive disturbance is the field imperfection due to LFD, which introduces significant field errors, particularly at the end of the flat top where detuning effects are largest. Whereas the field error must be as small as possible during the beam transmission time only, the feedback controller is compensating during the whole RF pulse. Large control errors demanding strong feedback controller action for compensation. The goal for the ILC is to minimize the control error, reducing the actuator gain given by the feedback controller. This allows to keep the closed-loop bandwidth small in order to prevent oscillations. The open-loop measurements presented here are the first measurements made with the ILC on this plant. In this case, state feedback was implemented in offline simulations, which was introduced to omit when combining the ILC with a feedback controller, [28]. The correction of the lorentz-force-induced field decay during the flat top is compensated, as can be seen in Fig. 5.2.

The adaptation is done during a part time of the flat top for both channels only. One can easily observe that the field error at the end of the flat top is already halved within one iteration step for the I channel. Within only 10 iteration steps the updates almost converged and the measured output has reached the reference trajectory during the flat top. The corresponding feedforward tables to be adapted are given in Fig. 5.3. It can be seen that the final value at the end of the flat top remains unchanged, which is related to the specifics of this algorithm.

Adaption during the flat top only turned out to be insufficient, because the residual overshoot at the begin of the flat top is not compensated fast enough, so in the next measurements, the adap-

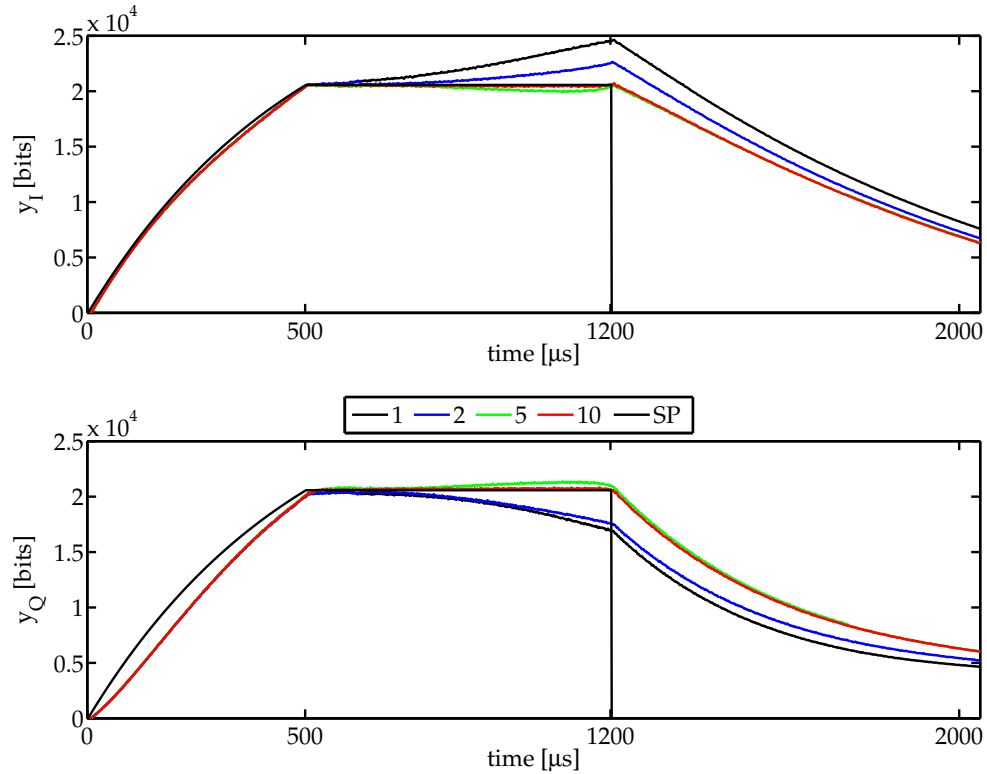


Figure 5.2: Adaptation of the open-loop system response during flat top. Effect of LFD is compensated within 10 iteration steps, [28].

tation was started during the filling time in order to keep the transition excursions acceptable. Additionally, it became evident that a better starting trajectory was achieved by replacing the standard (not adapted) feedforward tables with the adapted tables once the algorithm had converged. This is of course only possible for consistent amplitude and phase settings. For machine operation this method would allow to be faster and closer to the operation point without having a permanent adaptation. Furthermore, studies were performed using the optimized feedforward tables as the nominal feedforward and superimposing the excitation signals used for the system identification. Thus it is possible to overcome the drawback of complex detrending routines. As an addition, further open-loop control experiments have been done on a different acceleration facility to test the benefit of a model based approach. This system is rather complex to discuss in detail, but the basic results are given in the appendix A.1. Comparable to the studies on a different system for the feedback controller, this application shows the advantages concerning the model based design approach.

5.2.2 Closed-loop adaptation

The first closed-loop measurements were made with the proportional feedback controller which is permanently installed at the plant. Depending on the closed-loop conditions, the model has to be updated if the feedback controller is changed. The parallel development of both control

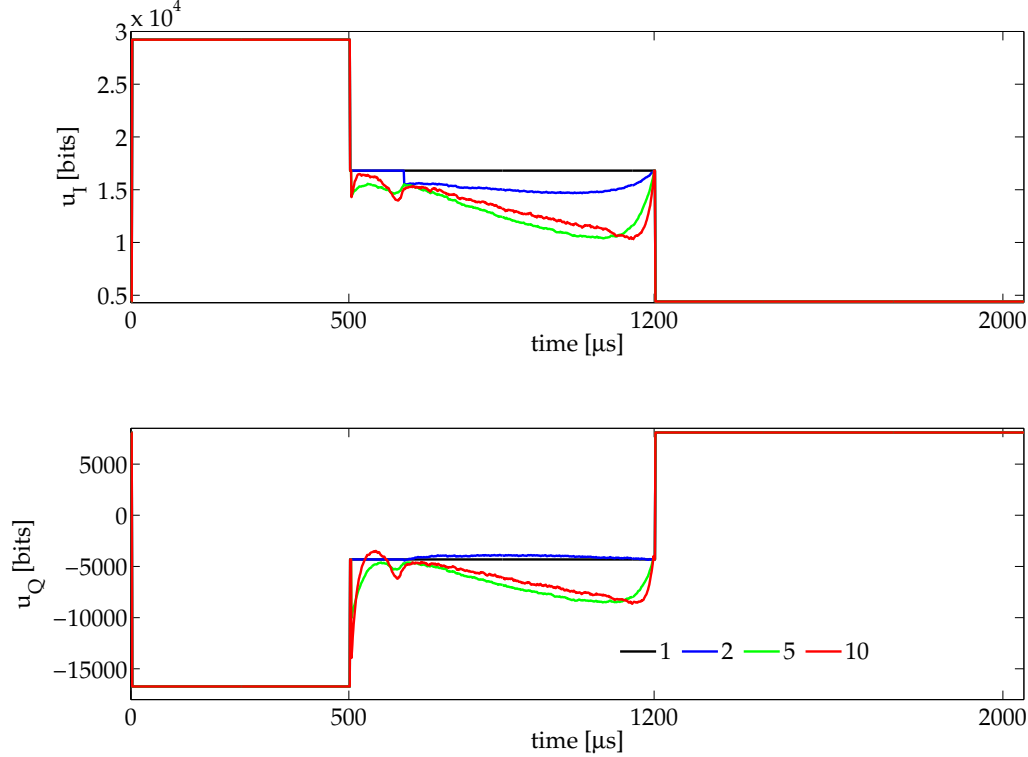


Figure 5.3: Corresponding input signals to Fig. 5.2, where the feedforward signals are adapted during flat top, [28].

techniques demands some compromises regarding the measurement conditions. For ideal setting of the feedback loop the proportional controller was typically operated with a feedback gain of about 40, which turned out to be a good choice. After the parallel system was introduced as described in Chp. 4 the implementation of the MIMO feedback was easier to realize and therefore measurements with this controller in combination are presented as well, in the following section. The essential benefit of operating the ILC on a closed-loop system is to test real operating conditions. This disturbance source causes different contributions than the LFD which has adapted in the open-loop measurements. Whereas the detuning process results in a low-frequency drift during the flat top, the beam is a high-frequency disturbance which has a large amplitude. The machine is operated in a way that the first bunch of an electron beam always occurs at the same sampling instant during the flat top, and measurement devices are synchronized to this time, to facilitate analysis of bunch resolved measurements. The train is distributed over the flat top according to the bunch-to-bunch repetition frequency and number of bunches selected. The large disturbance impact is not compensated by the feedback controller due to the limitation on the closed-loop bandwidth discussed in Sec. 2.2.3. Due to compensation by the ILC it is claimed to have higher frequency control signals which might be sufficient to suppress these effects. The adaption steps and the impact on the field error is shown in Fig. 5.4. Here the amplitude deviation introduced by the bunch is in maximum $\Delta A/A > 3.5 \cdot 10^{-3}$ in

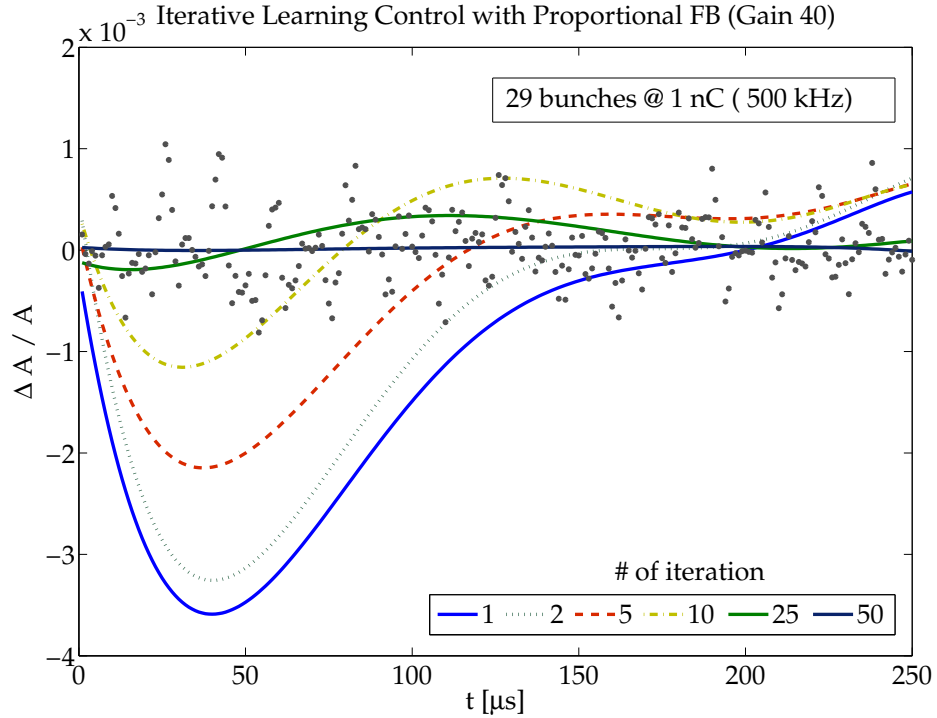


Figure 5.4: Fitted curves of RF field amplitude changes due to feedforward adaptation, compensating effects of beam-loading. Dots represent the measurement points after 50 iterations showing that only non repetitive fluctuations are left over

closed-loop operation with a feedback gain of 40. One can observe that the beam-loading effects can be minimized within 10 pulses to an acceptable level and fully compensated within 50 iteration steps. It is important, from a machine operations perspective, to quickly compensate large deviations over the train, so as to minimize transmission problems in the accelerator by optical settings. The fine removal of residual field errors takes additional steps. In Fig. 5.4 the measurement points are given as the dots after having 50 iterations performed. The lines represent the fitted curves of the measurement point for the earlier iteration steps. In this case the first measurement point is given by the first bunch and only the important 250 sampling instants during and after beam transmission are plotted. The minimum of the blue curve represents the last bunch position in the train of 29 bunches at a charge of 1 nC, which is typical for current operation. On crest acceleration leads to strong amplitude beam-loading effects as it can be seen from the figure. Therefore the phase information is left here. In Fig. 5.5 the relative amplitude and phase error are given as function of the iteration steps, with the same beam conditions as shown in the previous figure.

It can be seen that within 10 iterations, the main contributions to the field error are compensated for both phase and amplitude. For the phase error, the minimum is almost reached after 25 iteration steps whereas the relative amplitude error keeps getting smaller for the whole 50 iteration steps. This is due to the fact that the main contributions to the amplitude field error comes from beam-loading, while for phase, it is LFD. It can be seen that this application ultimately reaches a relative amplitude stability of $\Delta A/A < 0.01(\text{rms})$ and phase stability of $\Delta P < 0.025^\circ(\text{rms})$,

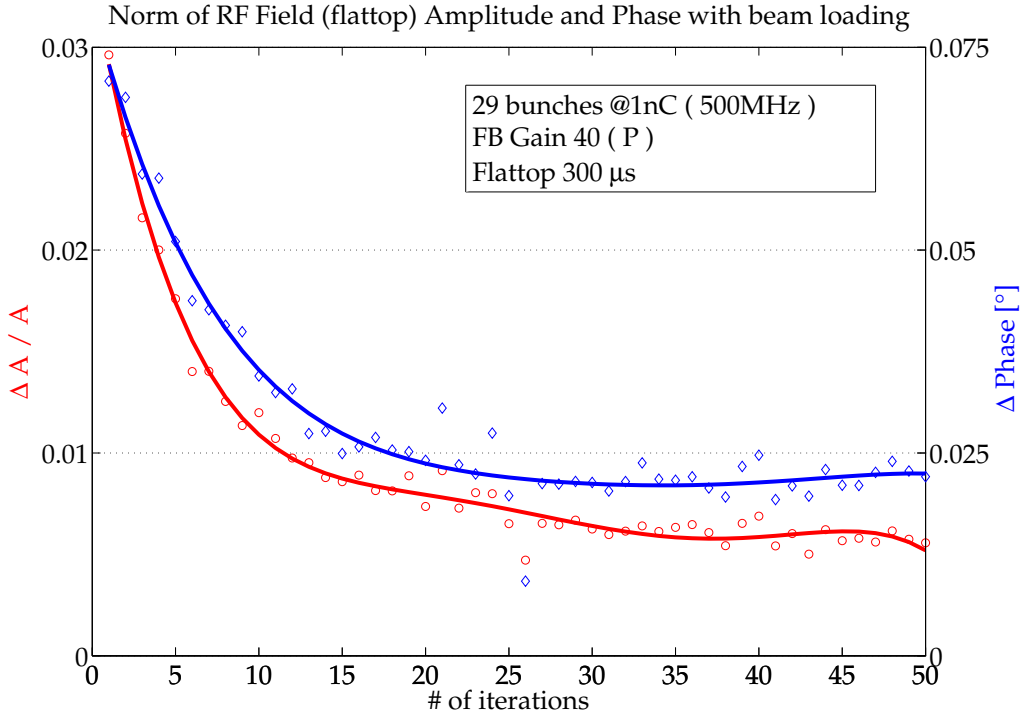


Figure 5.5: Norm of amplitude and phase error as function of the iteration steps. Main field error contributions are caused by electron beam for amplitude and LFD for phase

both of which are close to the requirements defined in the introduction. This raises the question, what would be the impact regarding the beam energy stability? Measurements of the beam are discussed in the next section.

Beam energy measurements

The main objective for RF field regulation is to deliver stable energy gain to the electron beam as needed for acceleration. Therefore it is necessary to clarify whether the compensation of beam induced disturbances on the RF field is also observed on the electron beam. A study can be made of whether or not perfect field regulation over the flat top is achieved after adaption, also results in a flat energy profile over a bunch train. Consequently, an assessment can be made of whether beam-based measurements must be taken into account for beam energy regulation, e.g. by applying further corrections for the setpoint tables.

In Fig. 5.6 the beam energy profile is shown for a bunch train of 30 bunches at a charge of 1 nC. The different measurements are given as bunch resolved function with mean values and rms spread given by the bars. To guide the eye the discrete bunches are connected by lines. The iteration steps are identified by the arrow.

Before starting the ILC a broad energy spread over the bunch train can be observed. The energy is normalized to the first bunch, leading to an energy difference between the first and last bunch in the train of $dE/E > 4 \cdot 10^{-3}$ before starting the adaptation. This is reduced to $dE/E < 5 \cdot 10^{-4}$, after feedforward adaptation. However, a small energy deviation is visible over the bunch

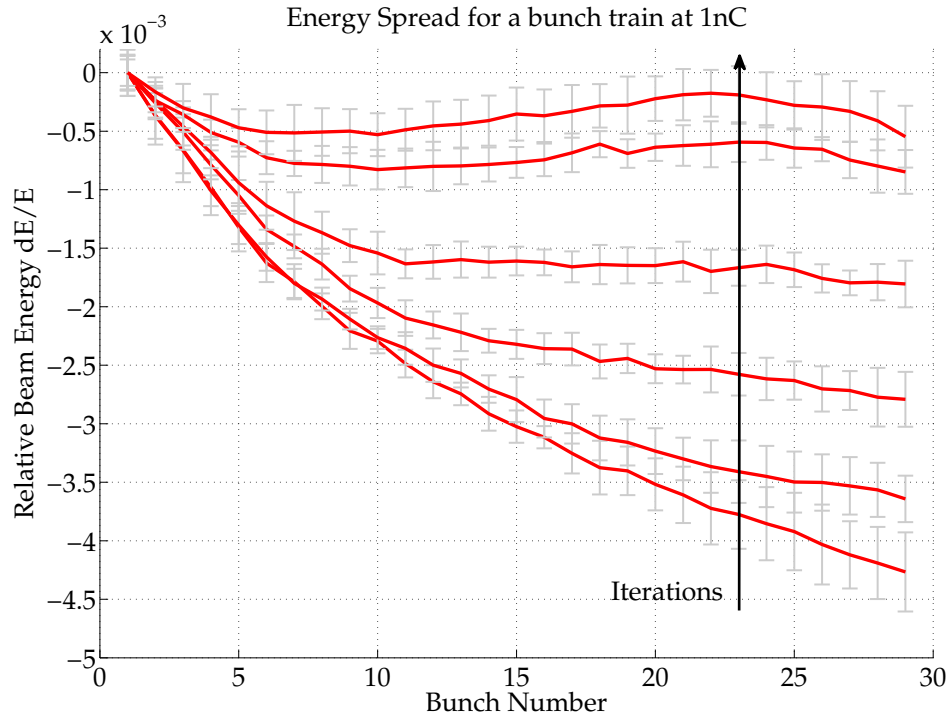


Figure 5.6: Removing transient energy slope on a bunch train caused by beam-loading effects on the field amplitude. Iteration steps are marked by arrow direction

train that resembles a sinusoidal waveform, although this was observed to be less significant in the field measurements. This residual error may be a result of the limited accuracy of the measurement equipment, but it also might be introduced by the ILC as a result of incorrect field detection. Especially measurements with the parallel system have shown that accurate field regulation does not necessarily result a perfect field flatness. Therefore it turns out to be necessary to include the beam information to the controller. Ideally by redefining the setpoint tables based on the measured flatness of the energy profile over the bunch train. The ILC in combination with the feedback controller is taking care to track this beam optimized reference trajectory.

Fig. 5.7 shows the beam energy distribution over the bunch train versus iteration steps. The plot illustrates the rapid adaptation that can be achieved, which is important for machine operations. The energy spread over the bunch train is given as the rms deviation. It can be observed that within 10 – 20 iteration steps the energy deviation is significantly reduced, while some additional steps are needed to further improve the energy deviation.

Pulse-to-pulse fluctuations still occur that are not compensated by this algorithm, which are mainly associated with microphonics and measurement noise. These fluctuations are non-repetitive and therefore compensated by the feedback controller. Integration of the MIMO feedback controller and ILC are discussed in the following section.

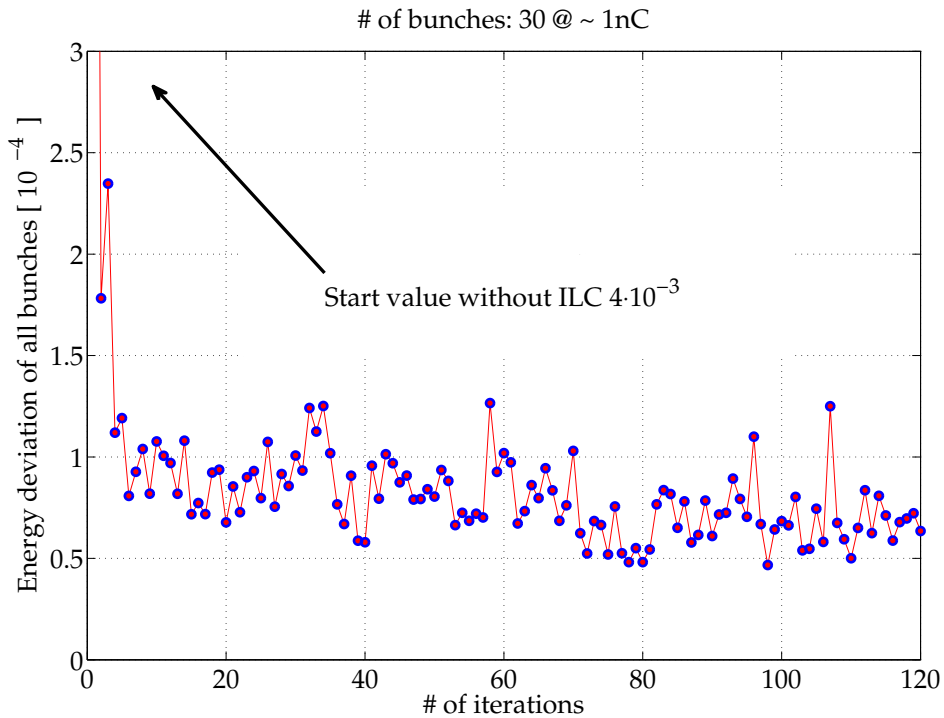


Figure 5.7: Convergence of energy spread over the bunch train after 40 iteration steps using proportional feedback with the iterative leaning controller.

5.3 Combined controllers

It has been shown that the ILC adequately suppresses the repetitive disturbances in both, open-loop and closed-loop operation. The previous chapter described improvements in pulse-to-pulse fluctuations that were achieved using the MIMO feedback controller.

Now the combination of both controller types will be introduced to study the cooperation regarding the field control of the plant. Allocating disturbances to the two controller types based on the frequency range, helps to overcome the drawbacks of each individual controllers. The final implementation is shown in Fig. 5.8, which extends the present system shown in Fig. 2.2 by adding the ILC and MIMO feedback controller. The figure also indicates broadly which components of the controllers are implemented in the FPGA, and which are implemented on other platforms, such as using Matlab code or in DOOCS servers. For the measurement examples presented here, the correction tables are not directly written into the FPGA but are computed beforehand and added to the original feedforward tables. For the permanent implementation the correction tables will have to be implemented inside the FPGA in order to allow fast interruption if exceptions occur. Additional notes to this statement can be found in Sec. 5.3.4. Several steps must be followed in order to determine the combined controller parameters, which are:

1. System setup and estimation of the open-loop model. Validation of the model using measurement data and previously estimated models.
2. Estimation of the MIMO controller parameters with a mixed sensitivity design solved

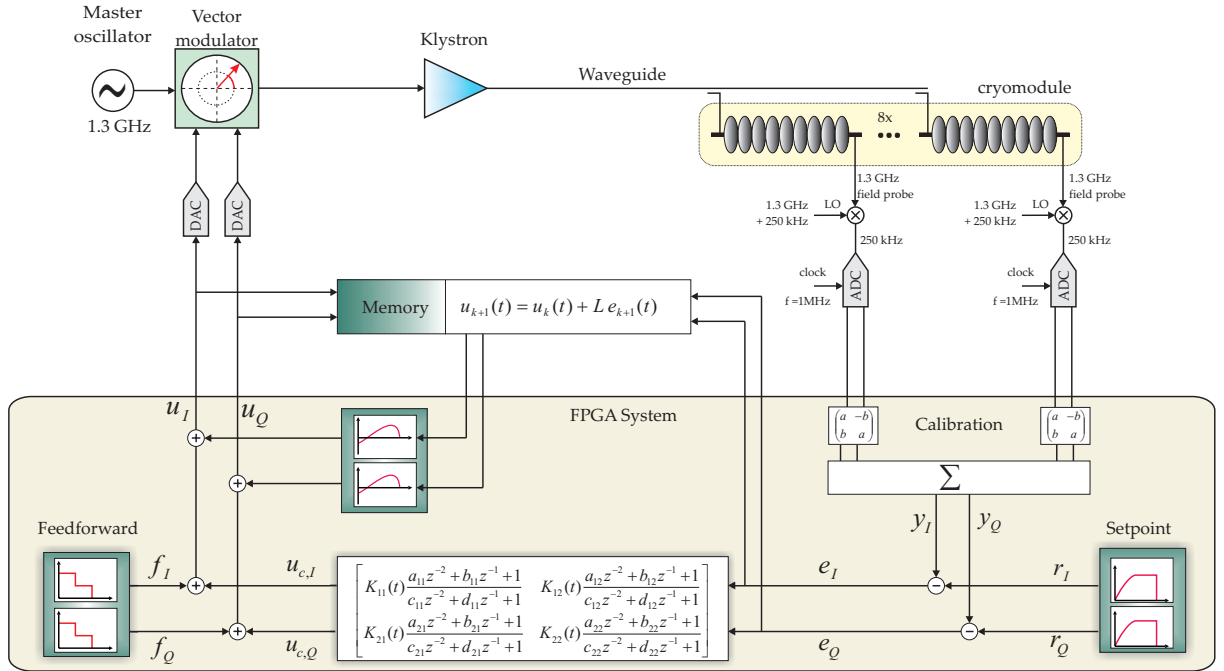


Figure 5.8: Schematic view of the new LLRF control system. The ILC is updating correction tables in the FPGA but calculated offline in a server. Inside the FPGA the MIMO feedback is used for intra-pulse feedbacks

by HIFOO, and testing the controller applicability by offline simulations. Loading the controller parameters to the system and closing the feedback loop. Check the performance of the feedback controller and if necessary tune proportional gain factors.

3. Excitation of the the system to generate closed-loop system response data and estimation of the closed-loop model. Validation of the model as done for the open-loop model.
4. Using the closed-loop model for computation of the adaptation matrices depending on system conditions (flat top time) and settings of the weighting matrices. Application of the ILC and start of the iteration process to compensate remaining repetitive field errors.
5. Verify there is effective compensation of beam-loading effects and further repetitive disturbances such as LFD and overshoots. Monitor the convergence speed and measure field stability from pulse-to-pulse and during the flat top phase.

The above list describes the procedure as it was applied during the test presented here. For future applications, it could be feasible to compute the closed-loop model from the open-loop model and the estimated feedback controller parameters. This would allow to take the open-loop model wide before measurements and do the feedforward adaption without having to estimate a closed-loop model during operation. Excitation of the plant cannot be done during regular FEL operation. Validation of the closed-loop model can be done with the online data taken during operation. This is also discussed when considering the permanent implementation.

5.3.1 Measurements with combined ILC and MIMO feedback controller

The presented measurements have been performed with one specific MIMO feedback controller. It has been seen that the pulse-to-pulse fluctuations are minimized by the MIMO FB, and the ILC is able to remove the major impact of beam-loading plus additional repetitive errors on the acceleration field. To visualize the improvements, in Fig. 5.9 the field error during the flat top is compared with open-loop measurements, closed-loop with the MIMO feedback controller, and the combination of MIMO feedback and iterative learning control. All measurements have been done at the same plant, but without the electron beam.

The residual control error is mainly determined by LFD and overshoots in the closed-loop mode.

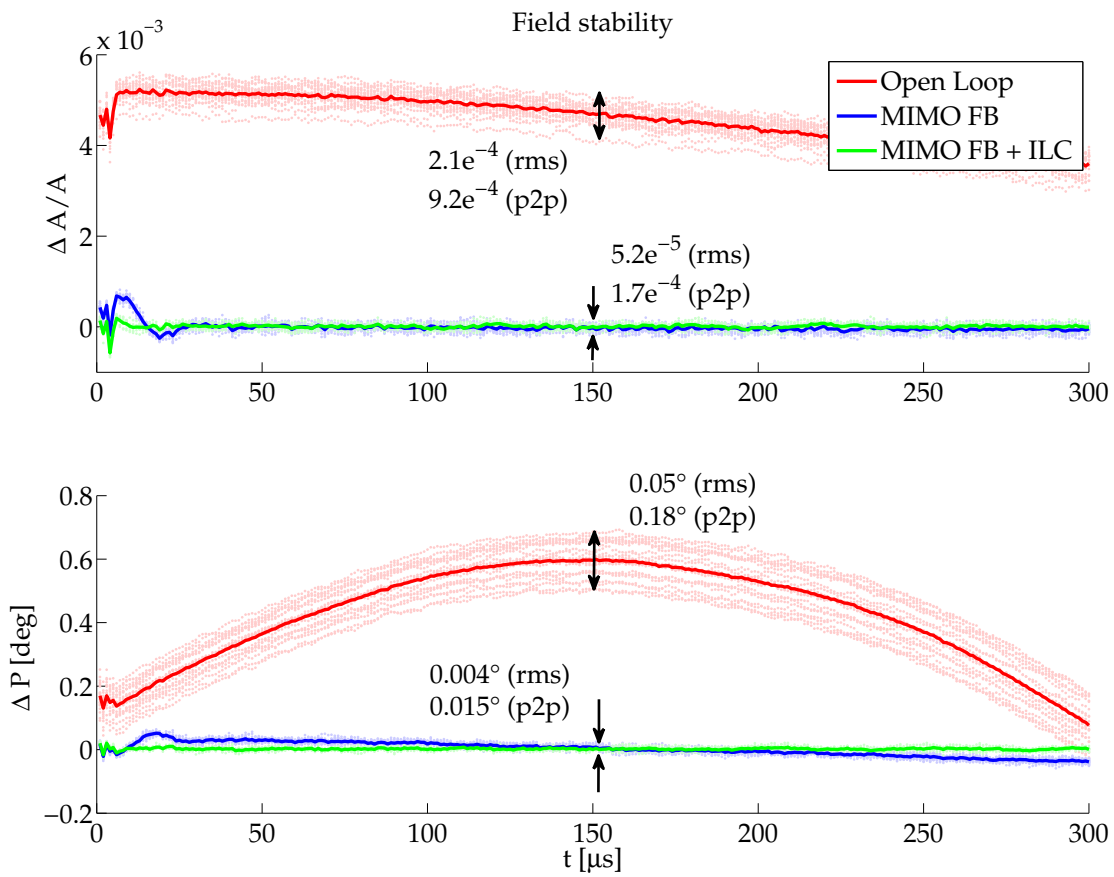


Figure 5.9: Comparison between open-loop measurements, the MIMO feedback and the MIMO feedback controller + iterative learning control after 10 iteration steps. Measurement points are given as dots, whereas the average is given in the solid lines marked by colors

For open-loop operation, large deviations of the field errors can be observed during the flat top, which is here at about $t = 300\mu s$. Single measurement points are given as dots in the corresponding colors of the mean values labeled in the legend. Pulse-to-pulse fluctuations are observable by the spread around the mean value. The calculated rms and peak to peak (p2p)

errors are given as values inside the plot. This spread significantly reduces from open-loop to closed-loop operation. Beside this, any fluctuations in the offset can be reduced while applying the feedback controller, as it is expected. Nevertheless, there remains a small slope in the amplitude and phase field errors, even in closed-loop operation with the MIMO feedback controller. Enabling the ILC removes this residual field error after several iteration steps. For illustration only the last iteration step is drawn. Furthermore the overshoot at the beginning of the flat top is also significantly reduced. Residual fluctuation are not fully suppressed, which is easier to observe in the more detailed Fig. 5.10.

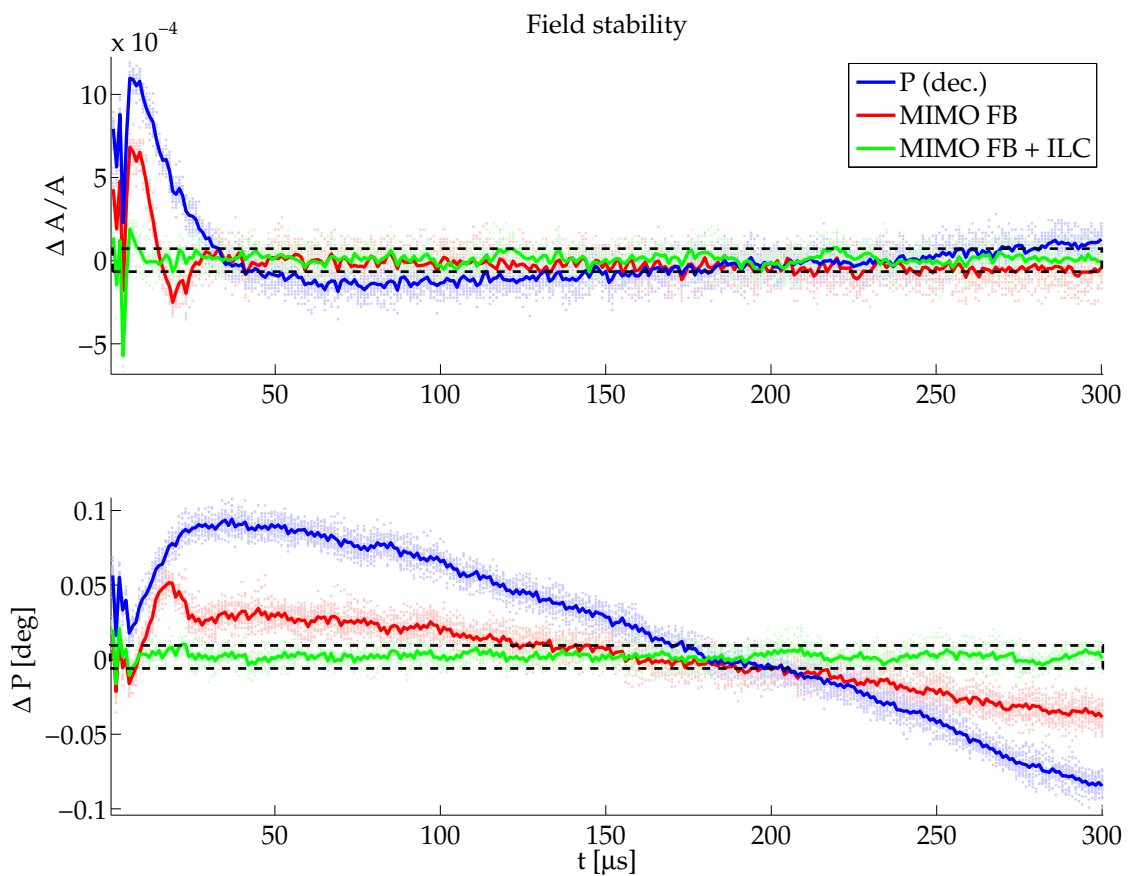


Figure 5.10: Comparison between closed-loop measurements with the proportional FB controller (gain 40), the MIMO feedback and the MIMO feedback controller + iterative learning control after 10 iteration steps. Measurement points are given as dots, whereas the average is given in the solid lines marked by legend given colors

Here, closed-loop measurements with MIMO feedback (in red) and the MIMO + ILC (in green) are compared with the closed-loop response of the original proportional feedback controller (shown in blue). Combining the MIMO feedback with the ILC results in almost perfect field regulation, except for the transient at the beginning of the flat top. It is the step step transition between filling and flat top that leads to the jumps in the control errors. This transition ideally

should be smoothed so as to reduce the oscillation at the begin of the flat top. Clearly, the settling time after the transition seen in Fig. 5.10 is much faster for the MIMO controller than for the proportional feedback. Furthermore, in the case of the proportional controller, the measured plant output is deviating from the setpoint, as seen by the residual slope in the amplitude error and a larger residual error on the phase. The slopes are smaller for the MIMO feedback but are still not fully compensated. The overshoots at the beginning of the flat top as well as the slope are then removed by the iterative learning controller. It can be seen that the performance requirements listed in the introduction are fulfilled with this combined controller concept. The pulse-to-pulse fluctuation (rms) are minimized to about $\Delta A/A = 2 \cdot 10^{-5}$ and $\Delta P = 0.004^\circ$ by the feedback controller, whereas the field errors measured for the flat top are approximately $\Delta A/A < 1 \cdot 10^{-4}$ and $\Delta P < 0.001^\circ$, when ignoring the overshoot in the beginning. To visualize the distribution of the relative amplitude error during flat top, all measurement points are plotted as a histogram in Fig. 5.11. The relative sample distribution is given as function of $\Delta A/A$ for different iteration steps.

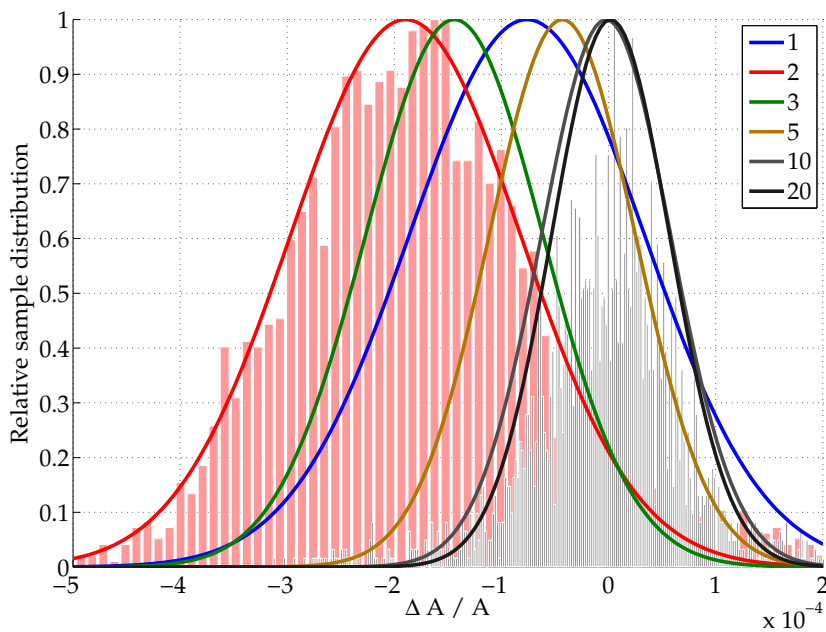


Figure 5.11: Distribution of the relative amplitude error $\Delta A/A$ for all measurement point during the flat top. The envelope of the histogram bars are given for the iteration steps.

The detailed distribution for iteration step 1 is shown by the bars and for better visualization, the normal curve of distribution is fitted. For clarity, the bars have been omitted from all subsequent steps. It is easy to observe that the mean value for the first iteration step is offset by approximately $\Delta A/A = 2 \cdot 10^{-4}$. The standard deviation (FWHM¹) of the first iteration step is about $2\sigma = 2 \cdot 10^{-4}$. With increasing iteration steps the mean value of this curve approaches 0 which denotes the suppression of steady state errors or effects like LFD. The standard deviation is also decreasing. Already after 10 iteration steps the adaptation has almost converged and

¹full width half max

after additional 10 steps only minor changes can be observed. The standard deviation has been decreased to $\Delta A/A < 1 \cdot 10^{-4}$, which is demanded by the requirements stated in the beginning. The requirements defined as control objective are achieved while using the combined controller concept.

For a permanent implementation additional considerations have to be made, and these are discussed in Sec. 5.3.4. However, before discussing implementation, one further aspect must be studied, namely whether the algorithm is stable over a long time once it has converged - something that is a common issue for iterative algorithms.

5.3.2 Long-term adaptation after convergence

For iterative algorithms, both the convergence speed and the long-term stability are important. Latter is very important for operation of the accelerator, because the machine users do experiments over large time periods. As a test, 1000 iteration steps have been made where in Fig. 5.12 some iteration steps have been sorted out. Machine conditions have not been changed during this adaptation, e.g., no phase or gradient changes as well as the same beam conditions. The figure gives the measured relative field error $\Delta I/I$ and $\Delta Q/Q$ instead of amplitude and phase presented so far. The yellow dots mark the measurement points during the flat top for 5 pulses, whereas the red dots give the mean values for every sampling instant of the flat top averaged from these 5 pulses. The mean is given to emphasize the repetitive component which is overlaid by additional measurement noise error, varying from pulse-to-pulse. The yellow ellipsoid marks the region of the computed rms error of the measurement points and the red ellipsoid the rms region of the mean values respectively. To give the control trajectory the required area of convergence determined by the required amplitude and phase stability is also drawn. Due to the phase settings in the machine the relative requirements in I are higher than for Q. In the following the individual plots of Fig. 5.12 are discussed in detail.

In plot (a) the first iteration step is given. It is evident, that there is an offset control error for all measurement points in the plot. This is mainly determined by the residual field error of the closed-loop system. As has been previously mentioned, the feedback controller is not able to compensate completely for these residual errors. This measurement was taken with beam that was being accelerated on crest, and beam-loading effects can be seen as the horizontal branch on the lower edge of the measurement points. The error is largely in the I channel because when operating on crest, the electron beam couples to the real (in-phase) component of the acceleration field, as introduced in Sec. 2.1.3. The two outliers to the right of the plot are residual overshoot sampling instants from the beginning of the flat top, and the steep diagonal tail is caused by the lorentz force detuning effects for the latter flat top region. It can be seen that as the detuning increases, there is a corresponding increase in the error contribution to Q. The width and location of the ellipsoids demonstrate the control error without applying the ILC to adapt the feedforward signal, even when the feedback controller is acting. In plot (b) the situation after 10 iteration steps is shown. The scalings on the axes are equal to plot (a) to emphasize the improvements already after 10 iterations. For a pulse-to-pulse repetition frequency of 5 Hz this would be within 2 seconds. It can be seen that the LFD effects are not fully compensated and that there are still two outliers to the right of the plot. However, the offset of the center of the ellipsoid has been moved towards the required location, and the

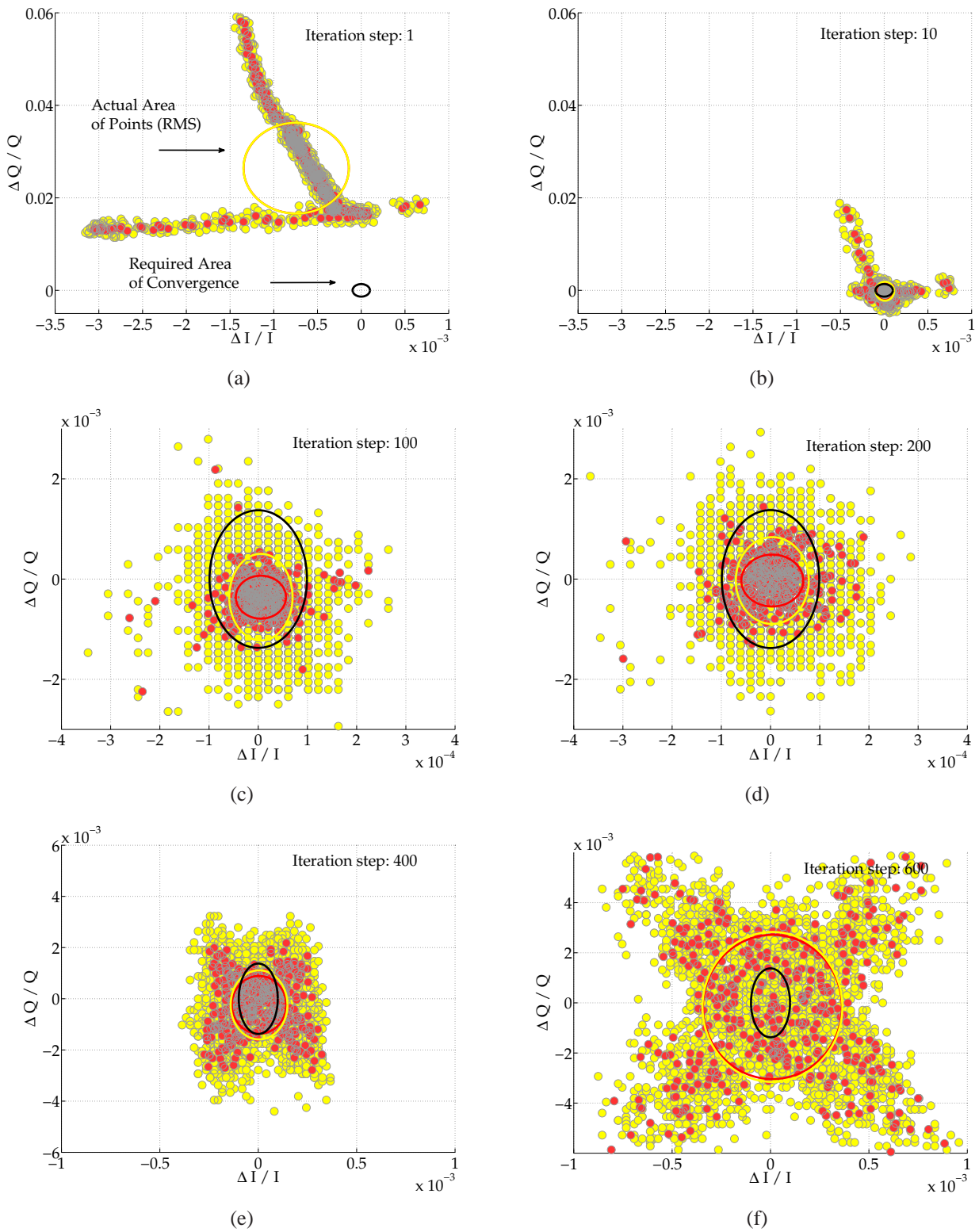


Figure 5.12: Deviation of measured field errors in IQ during flat top with MIMO FB and ILC for long-term iterations. Structural development of "cross" errors, caused by oscillation during flat top

spread of data-points has been reduced to an appropriate level. After 100 iteration steps the requirement for the rms field error is achieved, as can be easily observed in plot (c). Some measurement point are still outside the black area, but the main number of points is located inside. In plot (d) the algorithm has converged and the residual errors are distributed equally in the region. One can see that the centers of all ellipsoids are located approximately at origin, where $\Delta I/I = \Delta Q/Q = 0$. Additionally it can be seen that the measurement points (yellow) are fixed to a mesh structure meaning that the points are around the discrete limit given by the fixed points in the FPGA. Based on the data in plot (d), further improvements in the regulation would be hard to realize. Unfortunately, it can be seen from plot (e) that after 400 iterations the data points are moving away from the convergence area. It has to be remarked that the measurement points are not equally distributed, rather a "cross" seems to be drawn by the measurement points. This assumption can be verified when studying the last plot in this series (f), giving iteration step 600. These two crossed diagonals raising the question what measurement point distribution causes this final distribution? Obviously the measurement points cannot be derived from noise contributions, therefore one would assume an equal distribution in the IQ plane. The cross is likely caused by an oscillation distributed over the flat top. To prove this assumption in Fig. 5.13 the spectral distribution of the vector sum amplitude is given.

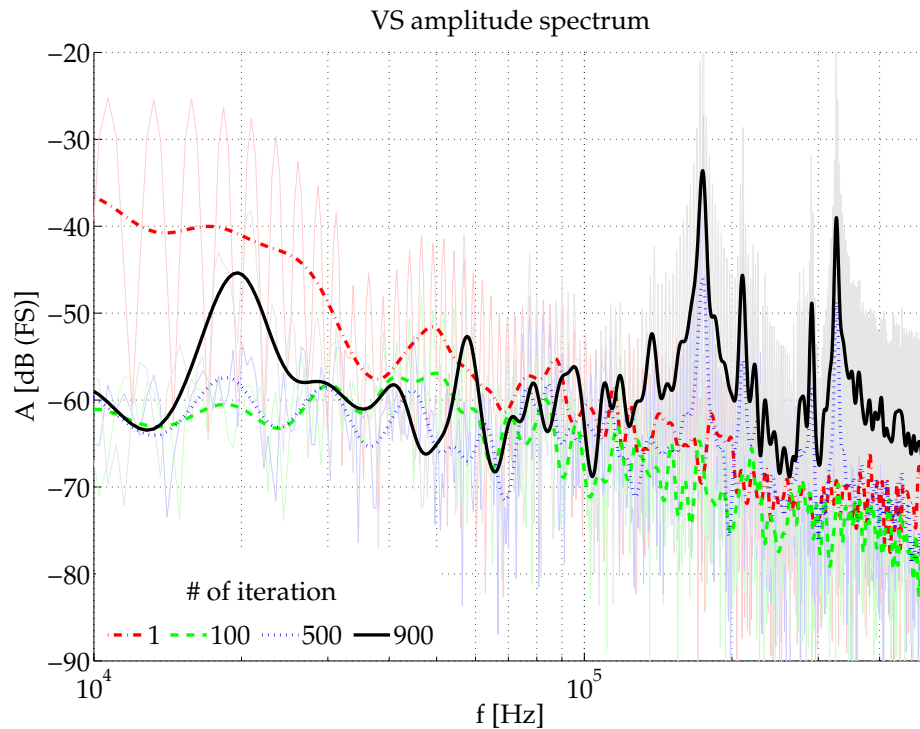


Figure 5.13: Frequency spectrum of the measured vector sum amplitude. In the low-frequency range are the magnitudes smaller after several iterations whereas after 900 iterations two resonance peaks are observable

The amplitude spectrum is derived from the measurement points during flat top and normalized to the maximum range of bits given in (decibel full scale $dB(FS)$). The frequency spectrum is generated by a fast fourier transformation (FFT). The actual spectrum is given as the dashed

opaque background, whereas the lines are drawn to guide the eye. The iteration steps are color labeled. One can see that in the low-frequency range, the amplitude will be suppressed with increasing number of iteration steps as it can be expected from Fig. 5.12. The green curve represents the smallest achieved control error, since it has the lowest integrated spectral contribution. In the higher frequency range > 1 kHz are no significant changes observable except for iteration number 500 and 900, which are representing the divergence cross section of the previous figure. The assumed oscillations can be easily detected in this plot. There are two resonance peaks, which seem to be mirrored at about 250 kHz. Comparing this with Fig. 3.16 shows the same resonance peaks. Therefore, it can be stated that the ILC seems to excite the $\frac{8}{9}\pi$ -mode, which could also be detected with the sinusoidal excitations have been made. The first resonance peak here is also located at ≈ 174 kHz. This effect is unwanted and has to be overcome when implementing this to the plant. Unfortunately all measurements have been made with the simple model of the system presented in Sec. 3.3.3. The resonance peak in the measurements has not been included in the system model, as it was presented in Sec. 3.4. It is expected that with this improved system model, the excitation of these resonances can be avoided. Tests are currently under investigation which can be found in [29]. The significance for the implementation and possible solutions are outlined in Sec. 5.3.4.

5.3.3 Beam energy spread for a bunch train

As has been discussed already, removing beam induced transients on the RF field must subsequently improve the beam energy distribution over a bunch train. It has been observed from measurements that the correlation between the field flatness and the beam energy distribution over a bunch train is given only to a certain limitation. In Fig 5.14 the relative amplitude stability and the beam energy relative to the first bunch are given as a bunch resolved measurement.

The residual wave which was visible in Fig. 5.6 is mostly removed in this plot. This has two main reasons. First the bunch repetition frequency was only 500 kHz during this measurement, which lead to a longer disturbance impact with half of the amplitude, meaning the disturbance was smaller. Additionally, the feedforward adaptation was corrected by time shifting steps. It was introduced in Sec. 3.3.4 that the measured system response can be detected with a time delay of $t_d \approx 2 - 4 \mu\text{s}$. Therefore, the control error is computed with a time delay of the same value. While using the delay corrected system model, it is further necessary to compensate later in the allied correction terms by $u_{corr}(t) = u_{corr}(t - \tau)$. The same experiences have been made while applying the feedforward correction term at the PSI machine, as discussed in the Appendix A.1. The outcome is a much improved flatness of the electron beam energy distribution as well improvements in the measured field amplitude. In this case, the large transition over the first two bunches is not being compensated, and this is visible on the amplitude. Ideas exist to simply remove first bunches in a train, but this demands fast kicker magnets which are currently not applied. Even so, the achieved relative amplitude error is in a range of $\Delta A/A < 1 \cdot 10^{-4}$ and also $\Delta E/E < 1 \cdot 10^{-4}$ over the bunch train for typical beam-loading conditions. Whereas the large drop at the beginning of the bunch train is visible for both measurements, the small fluctuations visible on the amplitude are not fully correlated with the electron beam energy.

Having collected all this expertise described herein, some consideration must be given to applying this combined controller method for permanent usage in the plant.

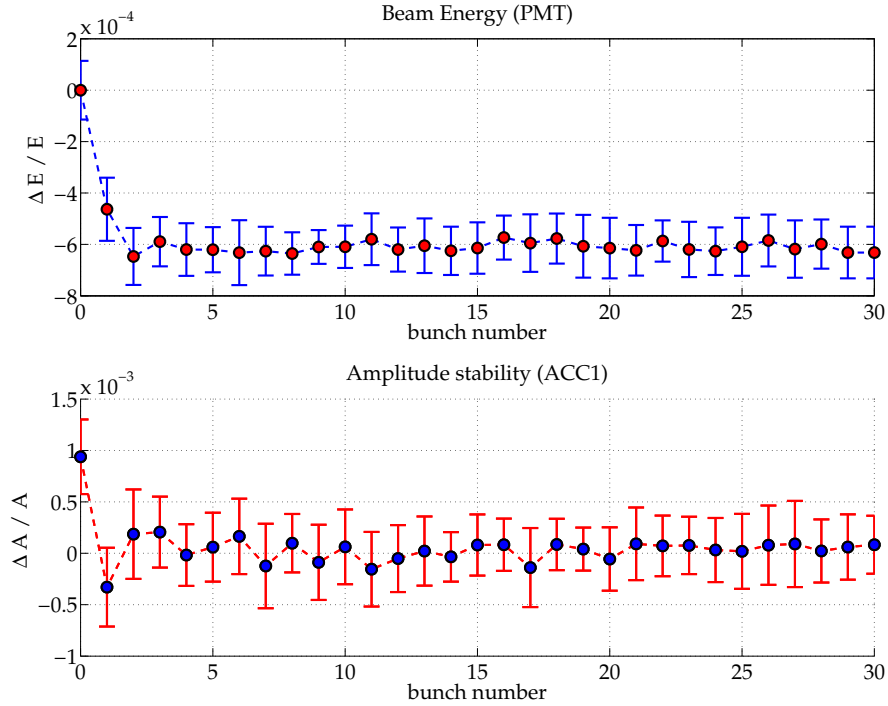


Figure 5.14: Amplitude and beam energy stability for a bunch train of 30 bunches after feed-forward adaptation with the ILC

5.3.4 Implementation considerations

For a user facility considered here a reliable system with high performance requirements is required. Therefore, all new applications have to be tested carefully before implementation, and further must be embedded in a functional system without having negative influences regarding existing applications. This demands a smart exception handling for all applications. As an example, the algorithm must be stopped if there is a malfunction in the underlying system. Defining a list of exceptions and developing tasks to be performed demands experience with the operating system and knowledge of typical operation routines used in the machine. In case of learning algorithms the framework for exception handling could be applied to different algorithms that might be tested in the future. Another point of consideration is the communication interface to the machine operators. Interaction points have to be predefined and those identified that might remain unchanged, such as the setting of the weighting matrices W_1 and W_2 . For the tests presented, the matrices have been chosen in a way that the convergence speed was sufficient without having overshoots in the correction tables from pulse-to-pulse. It might be possible to provide the users a tuning knob which allows to change the weighting factor q . This would have a comparable effect to a learning gain, which ideally can be tuned between convergence speed and reliability depending on the conditions for current operation. Therefore additional test must be made which show the practicability of this proposal. It is further to be thought if the weighting functions are defined as time depending matrices, to emphasize special regions of strong suppression like the filling, flat top transition. Simulations have been made

and can be found in [28].

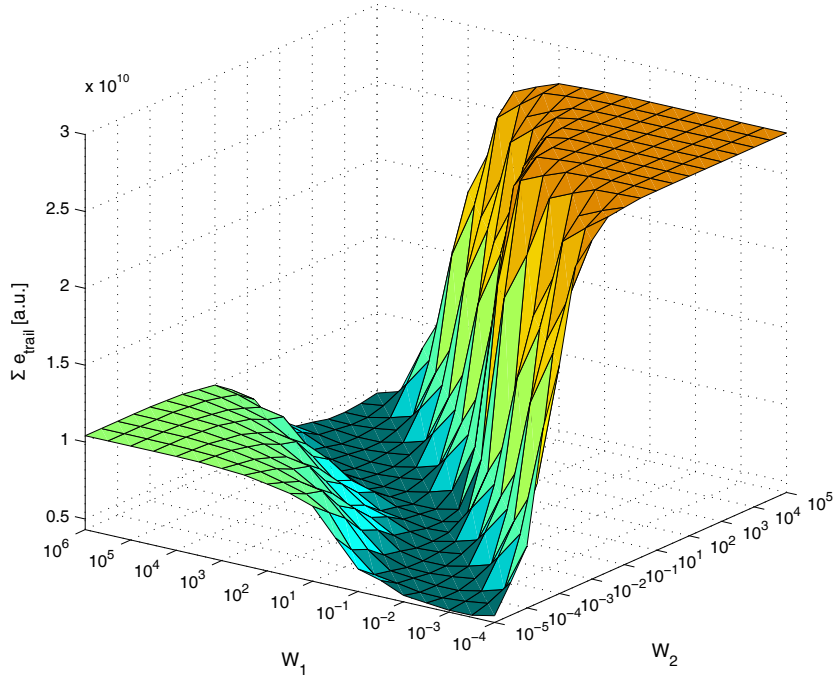


Figure 5.15: Simulation of the influence of the weighting matrices for the sum of residual control errors for a trail Σe_{trial} , [28]

For tuning processes in the machine, it might be necessary to change phase and amplitude frequently by small variations. It could be verified that setpoints changes do not lead to effect the ILC. Additionally, it might be possible to take the optimized feedforward signal as a starting point for normal operation. Furthermore, it has turned out that in the case of long-term adaptations, the algorithm is critical to avoid resonance peaks building up. It is assumed that this is caused by the special mode of the system which has not been considered in the model used for the measurements. In Sec. 3.4 an advanced model was introduced, which was recently developed but could not be tested with the ILC. It is assumed that when having modeled this resonance peak, the learning controller will not excite the system in this frequency range. To prove these assumptions tests on the plant must be performed. As an optional solution for the implementation, it would be possible to define thresholds to detect when the algorithm has converged, and the adaptation would then be stopped until the control error grew above this threshold. Meanwhile, the correction term would be filtered in order to generate a new starting correction signal. This is only a heuristic solution. Another issue which has not been discussed so far, but has been turned out to be most critical for this learning algorithms is a sudden disappearance of the electron beam driven by the so-called machine protection system (MPS). This is a machine safety system that cuts the beam if there are complications in other machine sub-systems, e.g. focussing issues or radiation alarms. The compensation of the beam-loading leads in this case to increases of the field amplitude, which might further result in unacceptable field gradients that could harm the machine. Consideration and possible solutions to this problem are discussed in Sec. 6.2. Finally the pulse-to-pulse adaptation in combination with the com-

munication interface has to be considered. The results that have been presented were made with Matlab based routines. For permanent application this communication interface has to be transported to a server-based functionality that is supported by the operation systems. The computations that have to be made between two pulses are limited to matrix multiplications, which are easy to realize. With the additional exception routines it has to be tested if the computations can be performed fast enough to allow a pulse-to-pulse adaptation or if it is necessary to reduce the update rate.

5.4 Summary

In this chapter an iterative learning controller approach to optimize the feedforward input to the system was introduced. The variety of disturbances was outlined which are not compensated by the feedback controller. It could be seen that the limited closed-loop bandwidth of the system does not allow to compensate high-frequency effects like beam-loading from the electron beam. The repetitive appearance of this disturbance source can be suppressed by changing the feedforward control signals. Following a short overview of possible iterative learning techniques, the F-NOILC algorithm used for this application has been introduced. Limitations of the system to be controlled demand a modified version of this algorithm, taking into account the intra-pulse feedbacks that have been realized with the previously introduced MIMO feedback controller. Measurements are presented that were made in open-loop and in closed-loop operation using the proportional feedback controller. Compensation of beam-loading effects significantly improve the RF field flatness. This has been shown by measuring the beam energy spread over a bunch train, which has been decreased by a factor of 10. To achieve remarkable results only 10 iteration steps are needed. As the major point in this thesis the combined controller concept of ILC and MIMO feedback was tested in real application. It can be seen that improvements to the current controller implementation are significant. The requirements for the residual control error can be achieved using this combined controller implementation for pulse-to-pulse as well as for the flat top field error. This marks a major improvement to the presently used controller algorithm. Studies have been made on the long-term stability, showing that after a large number of iteration steps oscillations tend to build up, which can be traced back to general system characteristics. Finally, some considerations have been made concerning the permanent usage of this controller concept for the real plant to be controlled. Currently, there are other iterative learning controller concepts under investigation, which will be tested and compared with the presented results [29]. With the enhanced system model, it is assumed to optimize the learning algorithm in order to minimize residual control errors. Further, incorporating beam measurements will improve the achievable beam regulation performance by gaining additional information about the real control value. The number of sensors in the system would be increased but the control signals remain as the real and imaginary part of the field vector.

Chapter 6

Conclusion and Outlook

In this thesis, a procedure was introduced for the design of a model-based controller for pulsed radio frequency fields in superconducting accelerating modules, where high performance is an essential requirement for free electron lasers and related accelerator system. A suitable black-box system model of the plant dynamics has been identified using subspace identification methods that generate an LTI state-space model from system response data only. Special excitation methods were used to characterize higher-frequency resonance peaks that come from physical properties of the system. The validated models are then used for designing the controllers required to stabilize the system against disturbances that are an inherent characteristic of system operation.

A combined controller concept has been developed that takes into account both disturbance characteristics and system limitations, with a significant improvement in field regulation from that of the original controller. There are two components to the combined controller: a MIMO feedback controller that suppresses non-repetitive and low-frequency field errors; and an iterative learning controller applied feedforward drive that pre-compensates predictable and repetitive disturbances, most notably caused by beam-loading. The very narrow bandwidth of the system permits the MIMO controller to suppress high-frequency disturbances occurring within the pulse with reasonable control effort.

This concept of splitting the compensation across controller types is essential for meeting requirements, and the resulting performance is significantly better than previously achieved with a single controller. A mixed sensitivity approach with the fixed-order controller design method HIFOO can be used to determine the feedback controller parameters. It has been shown that the feedforward controller is able to minimize repetitive field errors with minor adaptation steps, and it is particularly effective for compensation of beam-loading effects.

The outcome of this work is a model-based controller approach to RF field control that meets the required level of performance.

6.1 Achieved goals

Objectives of this work were outlined in the introduction. In subsequent chapters, additional perspectives were covered that addressed the machine operators. Listed below are the main achievements and experiences with respect to the itemization given in chapter 1.

1. It was shown that a model of the plant was identified by applying standard subspace identification methods for LTI systems. The input/output data generation and preprocessing steps were classified and tested in dedicated routines. Advanced detrending routines for pre-processing the measurement data turned out to have large influences on the model. It was shown that essential system dynamics can be modeled using a simple *3rd* order model. It was subsequently shown that the model quality could be improved by taking into account resonance peaks that were most likely caused by aliased from higher frequencies. Recent modeling results give hints how to improve this procedure in order to further improve the model-based designs.
2. Feedback controller parameters have been estimated using a semi automated procedure and the resulting controller designs have improved the field regulation relative to the original decentralized feedback controller. The mixed-sensitivity design allowed control parameters to be determined that improve the pulse-to-pulse field regulation by about a factor five. This model-based approach has been further tested on a new module that has been installed in the facility.
3. Iterative learning controllers were shown to successfully suppress repetitive disturbances to a remarkable level in amplitude and phase. Requirements on the flat top have been achieved both with and without presence of the electron beam, which provides the most significant source of disturbance. Furthermore the iterative learning controller has been tested on an additional application with comparable successful results.
4. Finally it has been shown that it is possible to realize the combination of both controllers on the plant, and that the combination meets requirements for field stability pulse-to-pulse and intra-pulse. The different time scale makes it possible for the two controllers to be active without influencing each other. It is expected that the performance will be further improved once the newest system models have been estimated.

While the performance requirements have been achieved and fundamental questions answered, experience from this work has raised additional questions that should be the subject of future studies, allowing this work to be built on for future application and tests. Additionally, the machine operators perspective is essential. Finally, all components of this work should be realized for the permanent machine operation that is so important for the goals of this work. These components are as follows.

1. All data transfer, evaluation and processing tasks are done with Matlab, while the feedback controller is implemented in the FPGA in order to achieve the real-time performance necessary for intra-pulse field control. It is intended to convert the Matlab routines as far as possible to programming languages used for the current operation system allowing a structured implementation. For the ILC it is intended to have a real time pulse-to-pulse adaption which demands a platform transfer for the data processing. The whole approach must be embedded in the present system used for operation.
2. Throughout the tests, no significant negative impacts on the reliability of the machine were observed. The setup of the controller parameters as well as the identification method requires additional machine time, which limits how often the updates can be done. Operability must be tested once there is a permanent implementation.

3. The use of an automatic routine for estimating the system model and designing the controller parameters reduces the required machine time to only a few pulses for exciting the system and measuring its response. Most calculations can be performed offline and therefore do not impact machine operation. The higher complexity of the feedback controller is justified by the achievable performance improvements. Controller parameters must be established before operation and only updated if found to be necessary.
4. It has been shown that the achieved improvements in the field regulation also have a positive effect on the beam energy spread and profile. It was also shown that RF field regulation alone is not sufficient to perfectly control the electron beam and consequently, further improvements should be achieved by including the available beam information, e.g. by optimized desired beam trajectories. Some details can be found in Sec.6.3.

In summary it has been shown that many issues associated with machine operations can be addressed. The proposed approach will, however, need to be in routine operation over some period of time in order to confirm reliability. In addition to the results presented here, tests have been performed on other accelerator systems using the model based approach and MIMO feedback and iterative learning controllers, hence demonstrating that the model based controller design methods can be used, provided the model describes the system sufficiently. For example, the MIMO feedback controller delivered very precise field control on the 3rd harmonic system, although these results need to be proven with the electron beam after the system is installed in the accelerator. Expertise gained from the modeling procedure shows the approach offers the highest possibilities for improvements that will still further enhance the quality of RF field control. All considerations made so far can be applied through an implementation framework which is briefly outlined in the following.

6.2 Future applications

The measurements presented in the thesis are only an extract of all the results obtained. It has been always the goal to implement this system for routine operation which demands many other complex considerations to be taken into account. In order to achieve the reliability and operability required by machine operations, the degree of automation and the use of fixed routines becomes a crucial factor, especially because of the greater complexity and from an increasing number of subsystems.

An example application to be automated is the system identification procedure that validates and if necessary updates the system model, which occasionally varies due to changes in the operation point, such as for significant gradient changes where the detuning effects vary. In Fig. 6.1 is sketched how a permanent validation of the model from measurement data could detect changes in the system behavior.

Should the system response vary from the simulated response, a possible malfunction in the plant can be detected. Otherwise, if the system behaves as expected, the model has to be updated. This proposal is just one example of possible routines, that might use the model-based approach.

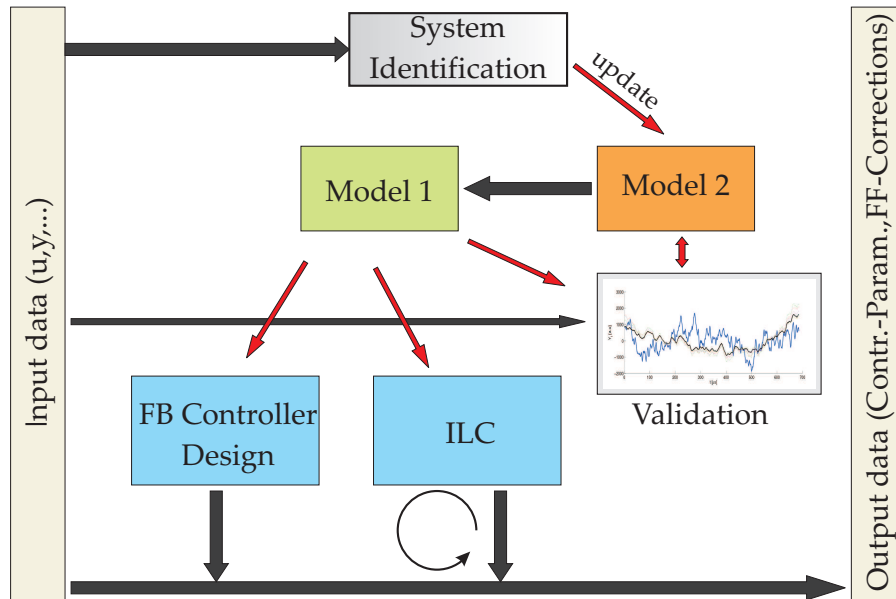


Figure 6.1: Idea of a frequently updated system model depending on current system status and operation point changes

Algorithms such as the ILC tested in this work might be substituted by different approaches which are currently under development. For this purpose it is necessary to keep the framework of the implementation modular. The control of 32 cavities will lead to further considerations which might contain nonlinear modeling approaches. Changes in the controller structure might be explored, for example to use observer-based feedback.

At this point, the combined controller concept still needs to be implemented. Considerations of how the combined controller could be fully integrated in FLASH operations are outlined in the following.

Planned system integration

Ideas for the possible implementation have already been introduced in the individual chapters. Beside integration to permanent operation, additional routines must be developed to deal with unexpected events. The tools used for the measurements are based on a Matlab environment, and these have to be converted to the operation system.

The implementation of the MIMO feedback controller is less of a concern because the FPGA realization already exist. Communication from the operating system to the parameter registers can be tested offline ahead of time. In case of problems, the proportional controller used so far can easily be realized by special setting of the controller parameters. On the other hand, implementation of the ILC is more complex for two major reasons. First of all the algorithm convergence is important. Once the algorithm has been enabled it should ideally converge fast, and once the control error is small enough, the adaptation should be halted so meaning the feed-forward signal remains unchanged. It has been shown that stability problems can occur after many iterations. Triggering the algorithm based on the magnitude of the control error might be a sufficient practical solution. Furthermore, the machine protection system introduces complications not mentioned so far. It has been shown that especially the operation of long bunch

trains demands a very effective exception handling, for example, the ILC should ideally react synchronously with fast beam cuts and if necessary scale back the correction terms to the feed-forward, or simply not apply them. Unfortunately this synchronization cannot be guaranteed due to the spontaneous appearance of bunch train cuts. Furthermore the computed correction term is ideally stored to have a fast adaptation when the train is recurring, preventing the recurrence of this cutting effect. A proposal for the beam-loading compensation in two stages, namely coarse and fine is illustrated along with additional proposals in Fig. 6.2.

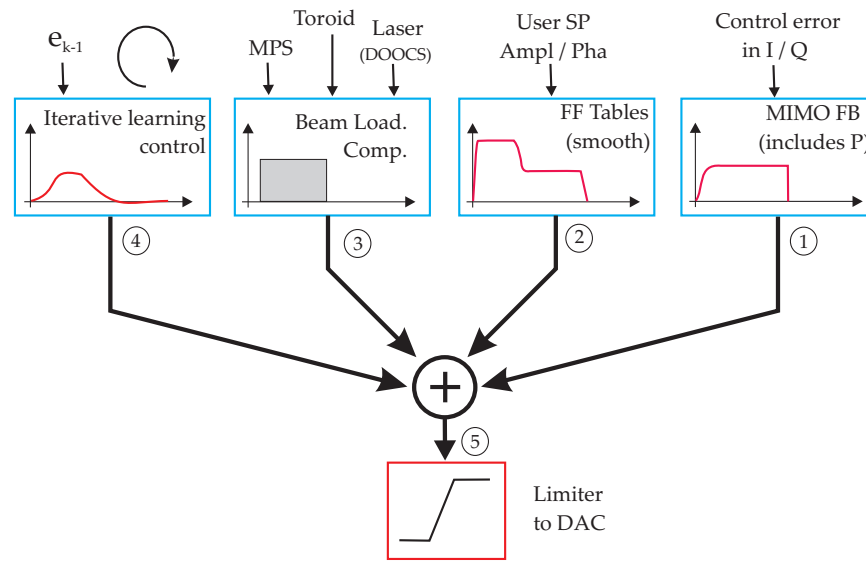


Figure 6.2: Implementation proposal for the RF table generation and control signal computation from sources of driving signal components

The control signals applied to the plant are combined as sketched in Fig. 6.2 are described in the following.

1. Using the MIMO feedback controller for intra-pulse RF feedbacks. Together with a smooth ramping of the proportional gain factor during the filling time, preventing unnecessary large control signals which are occasionally harmful to RF hardware. The controller parameters are estimated previously and updated if necessary.
2. Nominal feedforward tables, used as open-loop control signals will be applied. The transition from filling to flat top phase and the first sampling instants for the filling are smoothed compared the previous tables.
3. For coarse beam-loading compensation, the user settings and current system status are used to generate a simple feedforward correction table, that compensate main contributions from the electron beam induced field deviation. Direct connection to the machine protection system allows application of the compensation synchronized to the current beam settings (fast exception handling).
4. The iterative learning controller is the used for fine adaptation of repetitive control errors such as LFD and the residual beam disturbances, from the the coarse beam-loading compensation.

5. Limitations and threshold values to prevent unusual settings in the tables before applying control signals to the system. Mainly as additional exception to protect against unforeseen events.

Coarse compensation of beam-loading effects can be realized using a rectangular feedforward addition whose shape is depending on beam parameters such as charge and number of bunches. This adaptation must be synchronized to the system responsible for the beam generation. The advantage is that main field deviations generated by the electron beam are synchronously compensated to the beam arrival. If a bunch train is shortened, for example by the machine protection system, then the coarse compensation is synchronously truncated. This prevents exceeding of physical limitations of the cavity, due to bounded maximum gradients. The residual control error from the coarse adaption is compensated by the iterative learning controller, which performs fine compensation of beam-loading effects in order to the relative small energy variations over a bunch train. Additionally, it has turned out that the steep transition from filling to the flat top phase lead to large control errors. A smooth transition is needed to reduce the overshoots introduced by the feedback controller at the beginning of the flat top phase. Further improvement is expected by introducing a time-depending proportional gain for the feedback controller, especially at the begin of the filling phase, where the control error is large but is not necessary to be compensated. This can be realized by ramping the feedback gain as it is sketched in Fig. 6.2. It is also necessary to apply limitations to the controller output, in order to protect the system of controller malfunctions. As an enhancement to this proposal it is intended to integrate beam based information in the RF field control. Some consideration are given in the following.

6.3 Beam based feedbacks

It is planned to integrate beam based information into the field regulation process, and the required sensors are being developed and tested at the plant. Simply adding an additional feedback loop is not feasible without previously studying the influence of cascaded feedback loops that are connected to same actuators, especially since the number of sensor will increase, but the number of actuators remain unchanged.

An additional issue is the different vector components to be considered. Whereas the RF field is controlled in the IQ space, the beam information is provided in terms of amplitude and phase. Both descriptions can be transformed among each other, although this would demand additional processing steps. For first tests of the beam based feedback approach, where the feedback signal from the beam diagnostics was applied to the amplitude in the RF feedback loop, while the phase was controlled by the RF itself. This demanded a special implementation of the controller structure that is not discussed here. For the MIMO feedback loop however both controller channels are coupled by the cross terms in the controller, and this cannot be implemented in a simple division.

Furthermore it is not feasible to control RF fields from beam information only. For example after startup of the system the RF fields must be stabilized first before the beam can be turned on. The solution might be found in the combination of both feedback loops in one controller. The results and experience gained with the MIMO feedback controller established a good basis. It is conceivable to extend the multivariable-input, output controller to a 4×2 system by including the beam information as two additional inputs. This would require enhancements of both the

model and the feedback controller itself. The mixed sensitivity design would be a possible method to estimate the necessary controller parameters as it has been shown in this thesis. Certainly the weighting filters would have to be extended and a good tradeoff between beam and field contribution to the control signals would have to be found. An issue not detached from this idea is the small bandwidth of the cavity, which can easily be observed by the slow transient effect in the beginning of a bunch train. However pulse-to-pulse fluctuations visible on the beam would lead to an improvement for the regulation.

An additional possibility is to measure repetitive imperfections in the energy profile for a bunch train. It has already been shown that an ideally flat measured vector sum does not necessary lead to a correspondingly flat energy profile along the bunch train. Measuring deviations in the energy profile can be used to optimize the setpoint table for the RF field regulation. The feedback controller and the ILC take care of minimizing the control error with respect to the optimized setpoint trajectory. Measurement errors can be minimized by having an additional information about the assumed real vector sum measured by the electron beam. It has to be shown in measurements how this approach could improve the actual field regulation.

Bibliography

- [1] XFEL homepage: <http://www.xfel.eu/de/>
- [2] J. Feldhaus, J. Rossbach, H. Weise: *Freie-Elektronen-Laser*, Spektrum der Wissenschaft Verlagsgesellschaft, Heidelberg-Germany, Februar 1998
- [3] R. Brinkmann, et al.: *TESLA XFEL Technical Design Report*, DESY, Hamburg, 2002
- [4] E. Schneidmiller, E. Saldin, M. Yurkov: *The Physics of Free Electron Lasers*, Springer Verlag, Berlin-Germany, 2000
- [5] FLASH homepage: <http://flash.desy.de/>
- [6] S. Simrock, M. Felber, M. Hoffmann, B. Lorbeer, F. Ludwig, H.C. Weddig, K. Czuba: *Performance of the new Master Oscillator and phase reference system at FLASH*, Proceedings of PAC07, Albuquerque, New Mexico, USA, pp. 188 - 190
- [7] B. Aune et al.: *Superconducting TESLA cavities*, Physical Review special topics - accelerators and beams, vol., 2000
- [8] Vogel E.: *High Gain proportional RF control stability at TESLA cavities*, TESLA Report, DESY, Hamburg, 2007
- [9] T. Schilcher: *Vector sum control of pulsed accelerating fields in lorentz force detuned superconducting cavities*, Phd-Thesis, Hamburg, 1998
- [10] S. Simrock, et al.: *Considerations for the choice of the intermediate frequency and sampling rate for digital RF control*, Proceedings of EPAC06, Edinburgh, 2006
- [11] M. Hofmann: *Development of a Multichannel RF Field Detector for the Low-Level RF Control of the Free-Electron Laser at Hamburg*, Phd-Thesis, Hamburg, 2008
- [12] W. Giergusiewicz, et al.: *Low latency control board for LLRF system: Simcon 3.1*, Proceedings of Spie Volume 5948, 2005
- [13] A. Brandt: *Development of a Finite State Machine for the Automated Operation of the LLRF Control at FLASH*, Phd-Thesis, Hamburg, 2007
- [14] M. Liepe: *Regelung Supraleitender Resonatoren mit Strahlbelastung am TESLA-Test-Linearbeschleuniger*, UHH Diploma thesis, Hamburg, 1998

-
- [15] O. Kugeler, W. Anders, J. Knobloch, A. Neumann: *Characterisation of Microphonics in Hobicat*, Proceedings of FEL 2006, Berlin, 2006
- [16] T.L. Grimm, W. Hartung, T. Kandil, H. Khalil, J. Popielarski, C. Radcliffe, J. Vincent, R.C. York: *Measurement and Control of Microphonics in High Loaded-Q Superconducting RF Cavities*, Proceedings of Linac, Lübeck-Germany,
- [17] M. Huening: *Selbstoptimierende Parametersteuerung der Hochfrequenz des supraleitenden Linearbeschleunigers TESLA Test Facility*, Diploma thesis, Aachen, 1998
- [18] V. Ayvazyan, S. N. Simrock: *Dynamic Lorentz Force Detuning Studies in Tesla Cavities*, Proceedings of EPAC, Lucerne-Switzerland, 2004
- [19] M. Liepe, et al.: *Dynamic Lorentz Force Compensation with a Fast Piezoelectric Tuner*, TESLA Note 2001-3, Hamburg, 2001
- [20] L. Ljung: *System Identification - Theory for the user*, Prentice Hall, New Jersey, 1999
- [21] P. Van Overschee, B. De Moor: *Subspace Identification for Linear Systems*, Kluwer Academic Pub., Boston-USA, 1996
- [22] The Mathworks: *System Identification Toolbox User's Guide*, The Mathworks Inc., Natick-USA, 2004
- [23] T. Katajama *Subspace Methods for System Identification*, Springer-Verlag, London, 2005
- [24] J. Lunze: *Feedback Control of Large-Scale Systems*, Prentice-Hall, New Jersey, 1992
- [25] G. Strang: *Introduction to Linear Algebra*, Wellesly - Cambridge Press, MA USA, 2003
- [26] G. Koch: *Modeling of an accelerator based X-ray free electron laser system for controller design*, TUHH Diploma thesis, Hamburg, 2005
- [27] J. Lunze: *Regelungstechnik 2*, Springer-Verlag, 3. Auflage, Heidelberg-Germany, 2005
- [28] S. Kirchhoff: *Disturbance Modelling and Controller Design for an Accelerator based Free Electron Laser*, TUHH Diploma thesis, Hamburg, 2008
- [29] P. Gdaniec: *Grey-Box Identification and advanced Learning Feedforward Controller Design Methods for Free Electron Lasers*, TUHH Master thesis, Hamburg, 2010
- [30] R.T. Stefani, B. Shahian, C.J. Savant, G.H. Hostetter: *Design of Feedback control systems*, Macmillan Publishing Co., NY USA, 1990
- [31] J. Lunze: *Regelungstechnik 1*, Springer-Verlag, 5. Auflage, Berlin-Germany, 2005
- [32] S. Skogestad, I. Postlethwaite: *Multivariable feedback control, Analysis and design*, John Wiley and Sons, New York, 2001.
- [33] J. Doyle, B. Francis, A. Tannenbaum: *Feedback Control Theory*, Oxford University Press, NY USA, 2002

- [34] G.F. Franklin, J.D. Powell, A. Emami-Naeini: *Feedback Control of Dynamic Systems*, Addison Wesley, Reading, MA, 2002
- [35] F. Ludwig, M. Hoffmann, H. Schlarb, S. Simrock: *Phase stability of the next generation RF field control for VUV- and X-Ray free electron laser*, Proceedings of EPAC06, Edinburgh, 2006
- [36] J.M. Maciejowski: *Multivariable Feedback Design*, Addison Wesley, Cornwall-England, 1996
- [37] H. Langkowski: *Fixed-Order H_∞ Controller Design for the Free Electron Laser FLASH*, Diploma thesis, Hamburg-Germany, 2008
- [38] K. Zhou, J. Doyle: *Essentials of Robust Control*, Prentice Hall, New Jersey-USA, 1998
- [39] K. Zhou, J. Doyle, K. Glover: *Robust and Optimal Control*, Prentice Hall, 1996
- [40] J.V. Burke, D. Henrion, A.S. Lewis, M.L. Overton: *Hifoo - A MATLAB Package for Fixed-Order Controller Design and H_∞ Optimization*, IFAC Symposium on Robust Control Design, Toulouse-France, 2006
- [41] S. Gumussoy, M. Millstone, M.L. Overton: *H_∞ Strong Stabilization via Hifoo a Package for Fixed-Order Controller Design*, Proceedings of CDC, Cancun-Mexico, 2008
- [42] S. Gumussoy, D. Henrion, M. Millstone and M.L. Overton: *Multiobjective Robust Control with HIFOO 2.0*, IFAC Symposium on Robust Control Design, Haifa, 2009
- [43] C. Schmidt, G. Lichtenberg, W. Koprek, W. Jalmuzna, H. Werner, S. Simrock: *Parameter Estimation and Tuning of a Multivariable RF Controller with FPGA technique for the Free Electron Laser FLASH*, Proceedings of ACC, Seattle-USA, 2008
- [44] H. Langkowski, C. Schmidt, G. Lichtenberg, H. Werner: *An iterative learning control approach combined with a multivariable RF controller for the free electron laser FLASH*, Proceedings of ECC 09, Budapest, 2009
- [45] C. Gerth, F. Ludwig, C. Schmidt: *Beam based measurements of the RF amplitude stability at FLASH using a Synchrotron radiation Monitor*, Proceedings of DIPAC 2009, Basel, 2009
- [46] A. Wilhelm, Ch. Gerth: *Synchrotron radiation monitor for bunch-resolved beam energy measurements at FLASH*, Proceedings of DIPAC 2009, Basel, 2009
- [47] E. Vogel, et al.: *Considerations on the third harmonic rf of the European XFEL*, Proceedings of SRF 07, Beijing - China, 2007
- [48] E. Harms, et al.: *Third harmonic system at Fermilab/FLASH*, Proceedings of SRF 09, Berlin, 2009
- [49] S. Arimoto, S. Kawamura, F. Myazaki: *Bettering operation of robots by learning*, Journal of Robotic Systems, vol. 1, pp. 123-140, 1984

- [50] S. Arimoto, S. Kawamura, F. Myazaki: *Bettering operation of dynamic systems by learning*, Proceedings of 23rd IEEE Conference on Decision and Control, pp. 1064-1069 , 1984
- [51] S. Kawamura, F. Myazaki, S. Arimoto: *Applications of learning method for dynamic control of robot manipulators*, Proceedings of 24th IEEE Conference on Decision and Control, pp. 1381-1386 , 1985
- [52] J. Lee, K. Lee: *Iterative learning control applied to batch processes: An overview*, in International Symposium on Advanced Control of Chemical Processes, 2006, pp. 10371046.
- [53] K.L. Moore, C. YangQuan, A. Hyo-Sung: *Iterative Learning Control: A Tutorial and Big Picture View* 45th IEEE Conference on Decision and Control, pp. 2352-2357, 2006
- [54] J.D. Ratcliffe, J.J. Hatonen, P.L. Lewin, E. Rogers, T.J. Harte, D.H. Owens: *P-type iterative learning control for systems that contain resonance*, Int. J. Adapt. Control Signal Process., vol. 19, no. 10, pp. 769796, 2005.
- [55] Z. Bien, K. Huh: *Higher-order iterative learning control algorithm*, IEEE Proceedings, vol. 136, pp. 105112, 1989.
- [56] K.L. Moore: *Iterative Learning Control for Deterministic Systems*, Springer - Verlag, London, 1993
- [57] B.D.O. Anderson, J.B. Moore, C. Wen: *Iterative Learning Control*, Prentice-Hall, N.J., 1989
- [58] Y. Chen, C. Wen: *Iterative Learning Control*, Springer - Verlag, London, 1999
- [59] D.A. Bristow, M. Tharayil, A.G. Alleyne: *A Survey of Iterative Learning Control A learning-based method for high-performance tracking control*, IEEE control systems magazine, Vol. 26, pages 96-114, 2006.
- [60] D.H. Hwang, Z. BIEN, S.R. Oh: *Iterative Learning Control method for discrete time systems*, IEEE Proc. D, 1991
- [61] D.H. Owens: *Iterative learning control: convergence using high gain feedback*, Proceedings on 31st IEEE conference on Decision on control, 1992
- [62] J.D. Ratcliffe, L. van Duinkerken, P. Lewin, E. Rogers, J. Htnen, T. Harte, D. Owens: *Fast Norm-Optimal Iterative Learning Control for Industrial Applications*, 2005 American Control Conference, 2005
- [63] J.D. Ratcliffe, P.L. Lewin, E. Rogers, J.J. Htnen, D.H. Owens: *Norm-Optimal Iterative Learning Control Applied to Gantry Robots for Automation Applications*, IEEE Transactions on Robotics, Vol. 22, No. 6, 2006

-
- [64] N. Amann, D.H. Owens, E. Rogers: *Iterative learning control for discrete-time systems with exponential rate of convergence*, IEE Proc. Control Theory Appl., vol. 143, no. 2, pp. 217224, 1996.
- [65] N. Amann, D. Owens, E. Rogers: *Iterative learning control using optimal feedback and feedforward actions*, International Journal of Control, vol. 65, no. 2, pp. 277293, 1996
- [66] S. Kichhoff, C. Schmidt, G. Lichtenberg, H. Werner: *An Iterative Learning Algorithm for Control of an Accelerator based Free Electron Laser*, Proceedings on 47st IEEE Conference on Decision and Control, 2008

Nomenclature

ACC1	Acceleration Module 1
ADC	Analog to Digital Converters
DAC	Digital to Analog Converters
DESY	Deutsches Elektronen Synchrotron
DOOCS	Distributed Object Oriented Control System
FB	Feedback
FEL	Free Electron Laser
FF	Feedforward
FLASH	Free Electron Laser Hamburg
F-NOILC	Fast Norm Optimal Iterative Learning Controller
FPGA	Field Programmable Gate Array
HIFOO	H_∞ Fixed Order Optimization
IF	Intermediate Frequency
ILC	Iterative Learning Controller
LFD	Lorentz Force Detuning
LLRF	Low Level Radio Frequency
LTI	Linear Time Invariant
MIMO	Multivariable Input Multivariable Output
N4SID	Numerical algorithms for State Space Subspace System Identification
PRBS	Pseudo Random Binary Signal
PSI	Paul Scherer Institut
RF	Radio Frequency
SASE	Self Amplified Spontaneous Emission
SIMCON	Simulator and Controller
SIMO	Single Input Multiple Output
XFEL	X-ray Free Electron Laser

Appendix A

Additional results

A.1 Measurements from PSI

Beside the studies that have been done on the FLASH facility, the Paul Scherer Institut (PSI) offered the possibility to test the model based iterative learning control algorithm on an electron gun control system. These measurements have not been presented before, due to the different system characteristics. The system assembly is comparable to the control system presented for FLASH. A normal conducting cavity has a much lower quality factor which leads to a significant higher bandwidth in the system. Nevertheless the model based ILC approach presented should be able to control this system as it was claimed in this thesis. The application is of further interest, due to the normal conducting electron gun which is installed at DESY too.

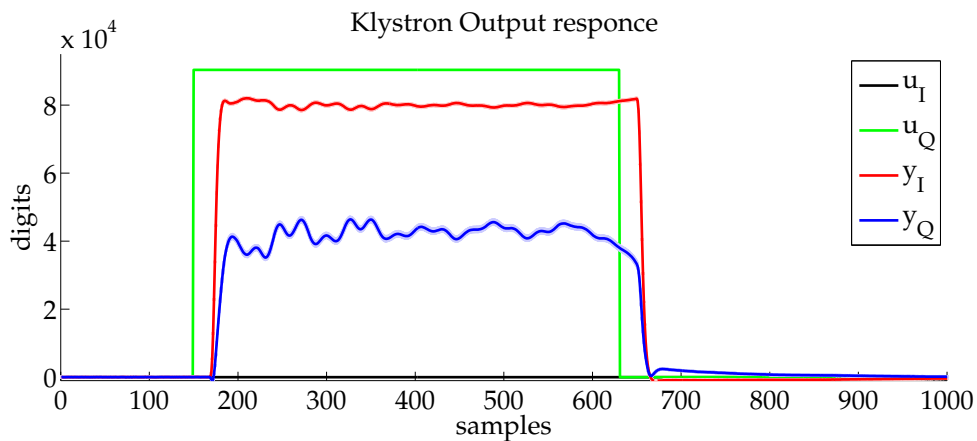


Figure A.1: Measured System response to usual input signals

The system is intended to be operated in open-loop and pulsed mode. This requires to find optimal open-loop control signals, achieving the intended constant output trajectory. By applying a rectangular pulse as starting trajectory, the following system response can be observed as shown in Fig. A.1. This repetitive oscillation visible as the klystron output is applied to the modulator which generates the necessary high voltage drive for the klystron. The control objective is to adapt the modulator driving signals u_I and u_Q such that the klystron output y_I and y_Q are flat

during the pulse. A reference trajectory does not exist and has to be defined as constant during the flat top computed from the mean values of y_I and y_Q . The application of an iterative learning controller is feasible to suppress this strongly repetitive field imbalances. The determination of the controller is done analog to the procedure discussed in this thesis. Therefore an open-loop model of the system has to be estimated from response data generated by excitation of the system. An example for the system response is shown in Fig. A.2, which gives a comparison of the system outputs y_I and y_Q with and without excitation signals.

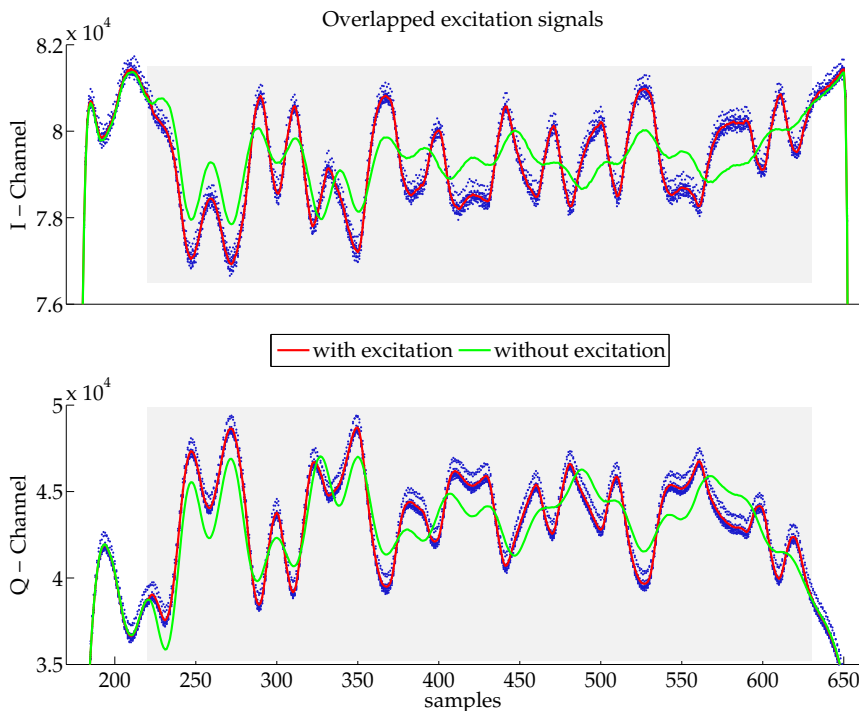


Figure A.2: Comparison of the system response with and without excitation signal.

The measurement points are given as the blue dots and the mean value as the red line. Excitation signals are applied within the shadowed area. It can be seen that the operation point is strong disturbed, which makes it necessary to remove this trends by subtracting the unexcited response from the data, as it has been shown in Sec. 3.2.2. After this subtraction the system response to the excitation signal can be seen in Fig. A.3.

The system response delay has been marked and is removed by shifting the data sets before identification. For the later adaptation done by the ILC this delay has to be taken into account, in order to apply the correction signals shifted to the measured error. Having the model, update matrices of the ILC algorithm can be computed and the controller is applied to the system input. In Fig. A.4 and Fig. A.5 the adapted system input and the corresponding responses are shown. It can be seen that within 10 iteration steps the input signal has almost converged and the measured system output is liberated from the repetitive disturbance effects. Although fluctuations from pulse-to-pulse still remain, they can not be compensated due to the absence of an intra-pulse

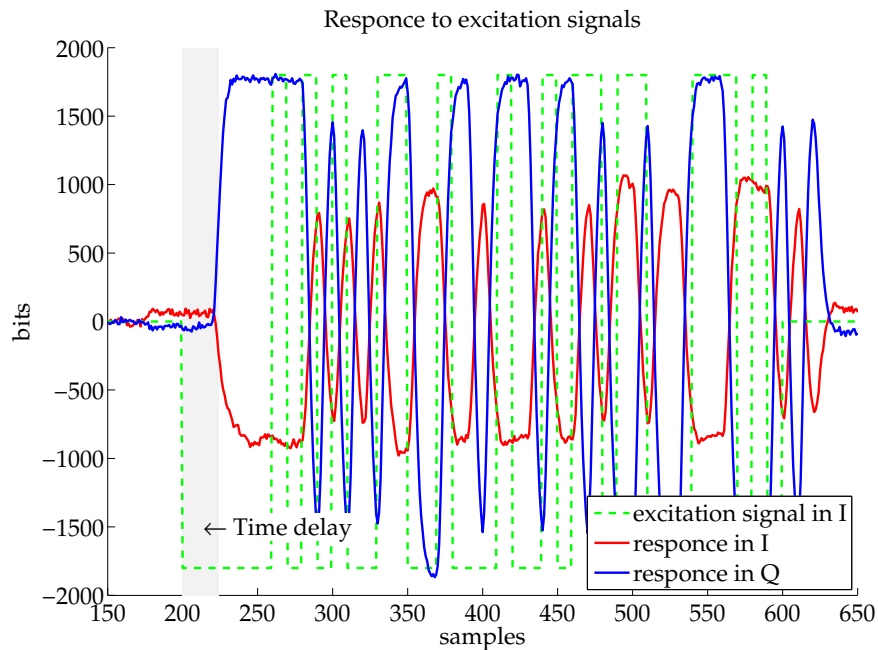


Figure A.3: Response to excitation signal after removing the unexcited system response from the measurement data

feedback controller. Finally in Fig. A.6, the amplitude and phase stability are given as function of the iteration steps. It is easy to observe that the convergence speed is fast and the adaptation remains stable for several iteration steps. Compared to the relative amplitude error $\Delta A/A$ and the phase error ΔP the improvement very significant.

These measurements show, that the model based approach of the ILC is able to compensate for repetitive disturbances also on different accelerator subsystems.

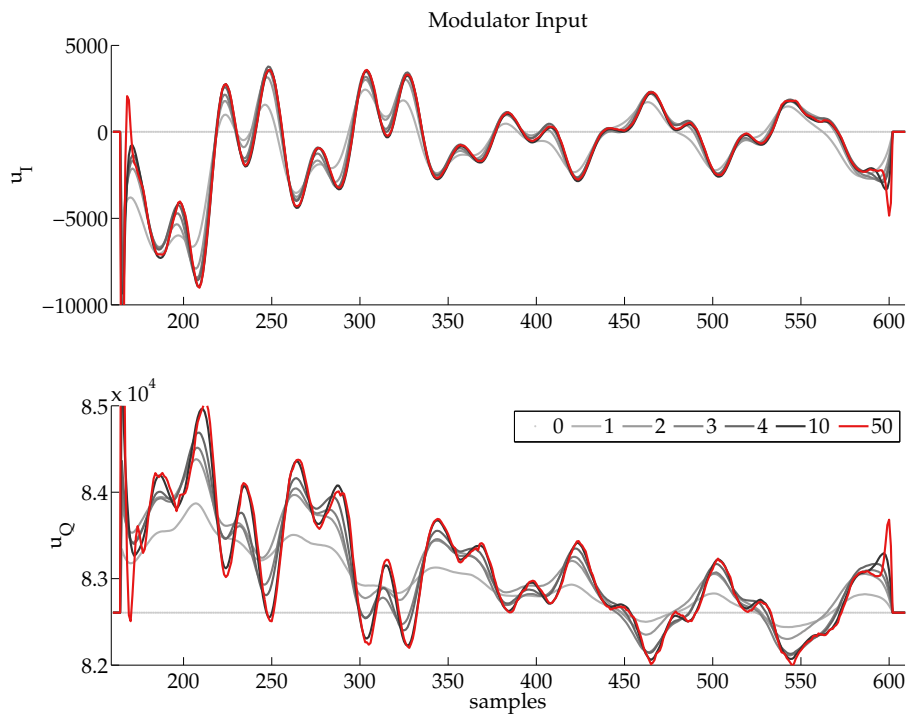


Figure A.4: Adaptation of the input channels I and Q of the system

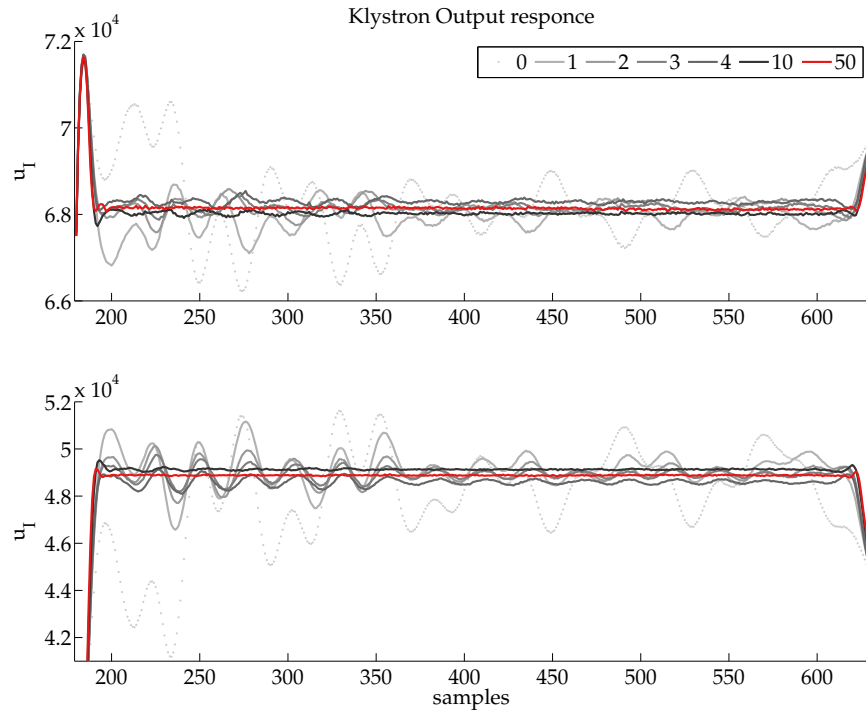


Figure A.5: System output for different iteration steps

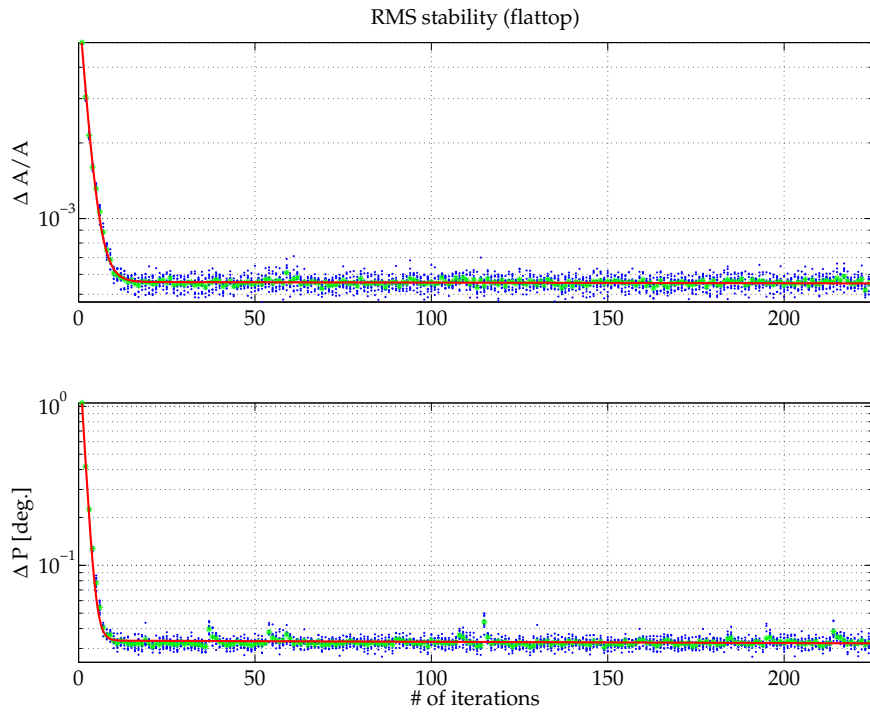


Figure A.6: Amplitude and phase control error during flat top (rms)

A.2 RF feedback controller

In the following an example of the parameter settings in the MIMO feedback controller should be briefly shown. This is done by a Bode plot of the feedback controller parameters used in the measurements done for the 3.9 GHz system. It can be seen that the controller is diagonal dominant for the low-frequency range $f < 1\text{kHz}$. For comparison the dc gains are given. Remembering the pulse duration is $t < 1300\mu\text{s}$, the frequency range of interest is given by $\approx 1\text{ kHz}$. In the high-frequency range some singularities occur which is due to the sampling process and therefore can be neglected here.

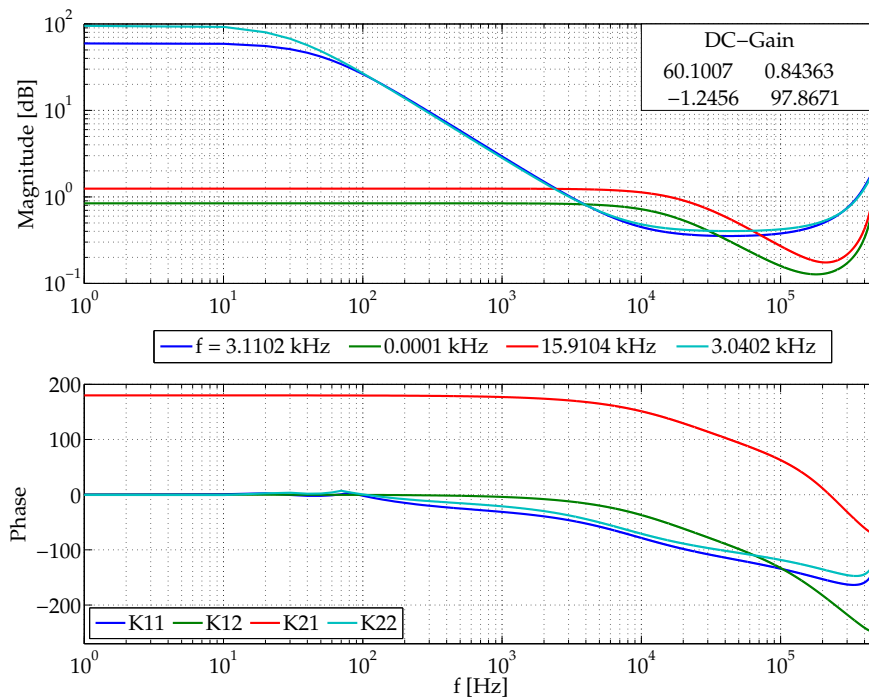


Figure A.7: Bode diagrams for the MIMO controller transfer function of the matrix elements. The frequencies given in the plots are the crossover frequencies of the the controller elements. Furthermore the dc gains of the controller parameters are shown

A.3 Additional plots for ILC

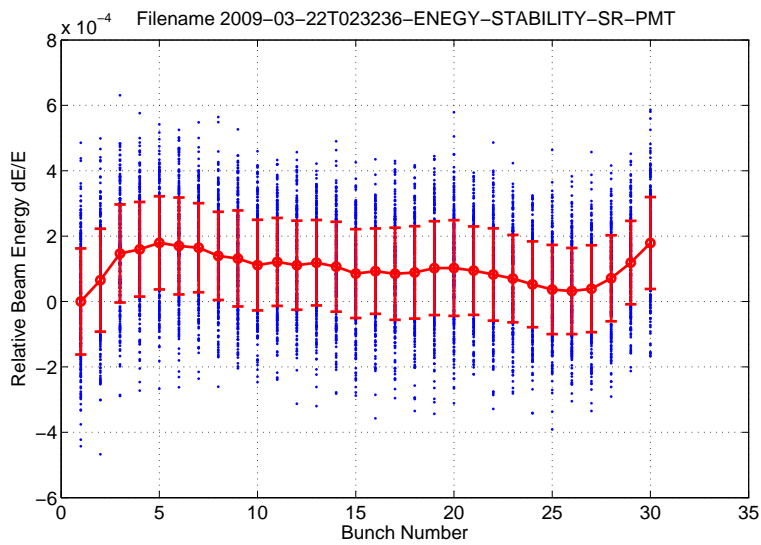


Figure A.8: Energy deviation over a bunch train measured by photomultipliers after adaptation

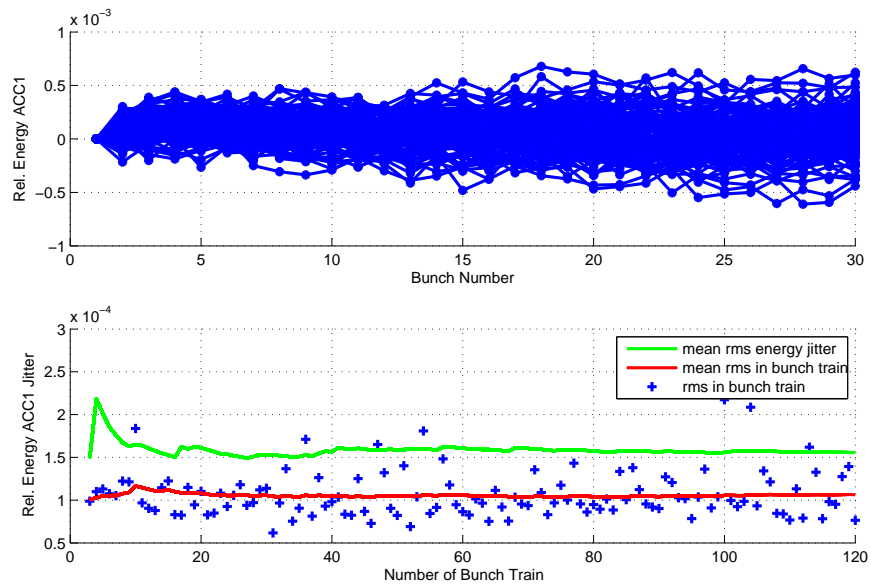


Figure A.9: Measurement of the energy jitter within a bunch train for several pulses after adaptation with the ILC

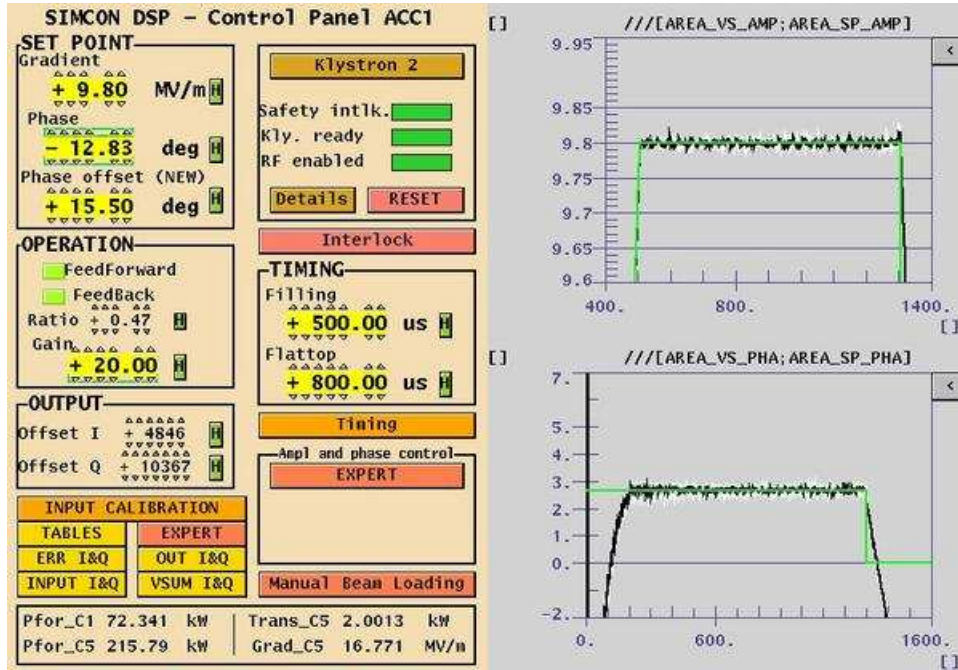


Figure A.10: Snapshot of the control system panels with ILC improvements

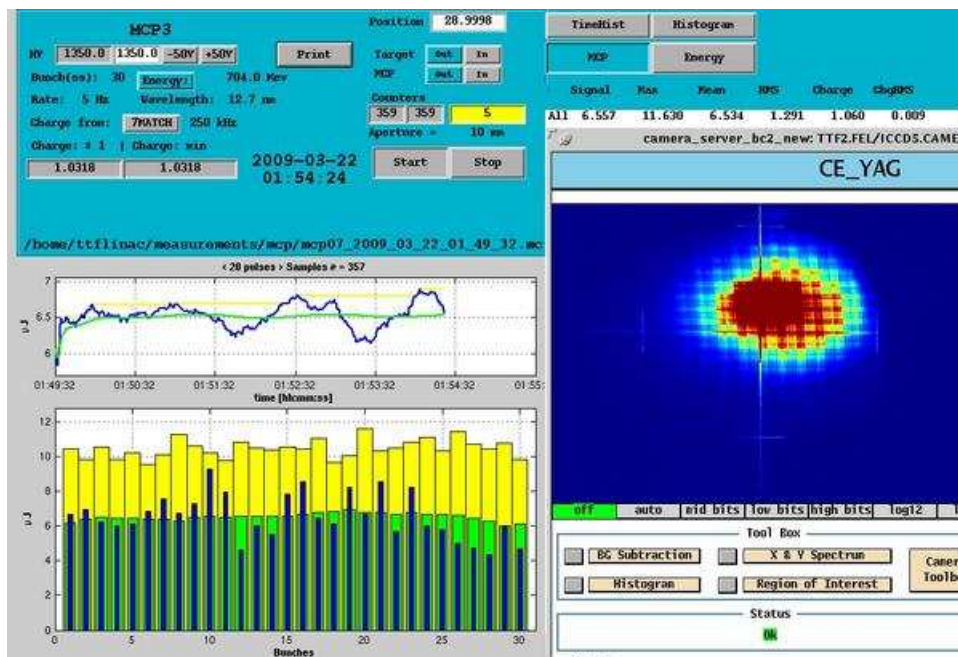


Figure A.11: Snapshot of the SASE energy monitor after removing beam induced transients in ACC1

Lebenslauf

Persönliche Daten:

Familienstand: ledig
Staatsangehörigkeit: deutsch
Geburtsdatum: 26. August 1980
Geburtsort: Parchim

Schulausbildung:

09/87 - 06/93 Schule am Klüschenberg
08/93 - 07/99 Gymnasium Lübz
07/99 Abitur

Hochschulstudium:

10/00 Immatrikulation an der Universität Rostock
10/02 - 06/04 Studentische Hilfskraft am Institut für Allgemeine Elektrotechnik der Universität Rostock
03/03 Vordiplom
03/06 Abschluss Dipl.-Ing. Elektrotechnik
04/06 - 09/06 Promotionsstudent am Institut für Allgemeine Elektrotechnik der Universität Rostock
10/06 - 03/10 Promotionsstudent am Institut für Regelungstechnik der Universität Hamburg-Harburg

Praktika:

08/02 - 10/02 Felika Elektroservice GmbH
10/04 - 02/05 Spallation Neutron Source Project
Oak Ridge National Laboratory, Tennessee USA

Beruflicher Werdegang:

10/06 - 03/10 Deutsches Elektronen-Synchrotron in Hamburg
Wissenschaftliche Hilfskraft mit Hochschulabschluss
zum Zwecke der Vorbereitung auf die Promotion
seit 04/10 Deutsches Elektronen-Synchrotron in Hamburg
Wissenschaftlicher Mitarbeiter